NASA CONTRACTOR REPORT

NASA CR-2042

NASA CR-2042

EVALUATION OF INSULATION MATERIALS AND COMPOSITES FOR USE IN A NUCLEAR RADIATION ENVIRONMENT

Phase II Final Report

by D. E. Westerheide, H. G. Carter,
R. C. Erickson, and E. E. Kerlin

Prepared by
GENERAL DYNAMICS
CONVAIR AEROSPACE DIVISION
Fort Worth, Texas
for George C. Marshall Space Flight Center

NATIONAL AERONAUTICS AND SPACE ADMINISTRATION • WASHINGTON, D. C. • MAY 1972

1. Report No. NASA CR-2042	2. Government Accession No.	3. Recipient's Catalog No.
4. Title and Subtitle EVALUATION OF INSULATION MATERIALS AND COMPOSITES FOR USE IN A NUCLEAR RADIATION ENVIRONMENT , Phase II Final Report		5. Report Date May 1972
		6. Performing Organization Code
7. Author(s) D. E. Westerheide, H. G. Carter, R. C. Erickson, and E. E. Kerlin		8. Performing Organization Report No. FZK-380
		10. Work Unit No.
9. Performing Organization Name and Address General Dynamics Convair Aerospace Division Fort Worth Operations Fort Worth, Texas		11. Contract or Grant No. NAS 8-25848
		13. Type of Report and Period Covered NASA Contractor May 1970 – May 1971
12. Sponsoring Agency Name and Address National Aeronautics and Space Administration Washington, D. C. 20546		14. Sponsoring Agency Code

15. Supplementary Notes

16. Abstract

The results of the studies show that the nuclear heating of the propellant in all of the four baseline RNS configurations studied (1575-MW NERVA) was much lower than that of the nuclear flight module (NFM) configuration with the 5000-MW NERVA analyzed previously. Although the nuclear heating has been reduced, the effect of nuclear heating on the propellant as well as the effect of nuclear heating on internal structure such as anti-vortex baffles, screens, and sump components cannot be neglected. In addition, it was found that the present analytical procedures were not able to predict boundary-layer initiation and breakoff points with the accuracy necessary to predict propellant thermodynamic nonequilibrium (stratification) and/or mixing.

17. Key Words (Suggested by Author(s)) Insulation Materials Radiation Nuclear heating	18. Distribution Statement

19. Security Classif. (of this report) Unclassified	20. Security Classif. (of this page) Unclassified	21. No. of Pages 210	22. Price* $3.00

*For sale by the National Technical Information Service, Springfield, Virginia 22151

This report was prepared by the Fort Worth operation of General Dynamics, Convair Aerospace Division under Contract NAS8-25848, <u>Evaluation of Insulation Materials and Composites for Use in a Nuclear Radiation Environment</u>, for the George C. Marshall Space Flight Center of the National Aeronautics and Space Administration. The work was administered under the technical direction of the Astronautics Laboratory, Engineering Physics Branch of the George C. Marshall Space Flight Center, with Dr. R. L. Gause acting as contracting officer's representative.

FOREWORD

.The Fort Worth operation of the Convair Aerospace Division
of General Dynamics under Contract NAS8-25848 with the George
C. Marshall Space Flight Center is participating in a study
that is part of the overall effort necessary to develop the
technology required for the design of a nuclear rocket vehicle.
This work is based in part on the nuclear flight systems con-
cepts generated under Contracts NAS8-24714 (McDonnell Douglas
Corp.), NAS8-24715 (Lockheed Missile & Space Co.), and NAS8-
24975 (North American Rockwell Corp.). The propulsion system
for the flight vehicle is the 1575-MW, 75,000-lb-thrust NERVA
engine being designed under Contract SNP-1 (Aerojet Nuclear
Systems Company and Westinghouse AstroNuclear Laboratory). The
current study is an extension of nuclear rocket vehicle develop-
ment work previously performed by the Nuclear Aerospace Research
Facility of the Fort Worth operation under Contract NAS8-18024.

This report is one volume of the final progress report to
be issued under Contract NAS8-25848. The report documents and
discusses work performed under Task I - Redesign of Propellant
Heating Experiment - during the period 21 May 1970 through 21
May 1971 and includes the Task I work reported in the first,
second,and third quarterly progress reports.

The work performed under Task II - Radiation Analysis of Saturn V Materials, Systems, and Components - of Contract NAS8-25848 is documented in a separate volume, General Dynamics Convair Aerospace Division Report FZK-378.

S U M M A R Y

The major tasks completed and documented in this report
are: (1) analysis of the fluid dynamic and thermodynamic phenomena
of the liquid hydrogen propellant of five candidate Reusable
Nuclear Shuttle (RNS) configurations for a typical lunar shuttle
mission, (2) development of a liquid hydrogen propellant heating
experiment (PHT) for the Aerospace Systems Test Reactor (ASTR)
facility capable of simulating the fluid dynamic and thermodynamic
phenomena of any one or all of the four baseline RNS configurations,
(3) determination of the effect of operational variables on the
overall fluid dynamic and thermodynamic characteristics of the
RNS and PHT, (4) comparison of the propellant phenomena data gen-
erated for the 5000-MW NERVA under NAS8-18024, Modification 2, to
that developed for the 1575-MW NERVA under the present contract,
(5) revision of the AG4 and RIO propellant heating computer codes
to incorporate procedural and geometric changes in the codes as
required for the current RNS concepts, and (6) investigation of
the effect of heat shorts, antivortex baffles, propellant retention
screens, and the sump on propellant phenomena.

The results of the studies show that the nuclear heating of
the propellant in all of the four baseline RNS configurations
studied (1575-MW NERVA) was much lower than that of the nuclear
flight module (NFM) configuration with the 5000-MW NERVA analyzed
previously. Although the nuclear heating has been reduced, the

M374

effect of nuclear heating on the propellant as well as the effect of nuclear heating on internal structure such as antivortex baffles, screens, and sump components cannot be neglected. In addition, it was found that the present analytical procedures were not able to predict boundary-layer initiation and breakoff points with the accuracy necessary to predict propellant thermodynamic nonequilibrium (stratification) and/or mixing.

Further, the results show that the conditions required to simulate the pertinent fluid dynamic, thermodynamic, and nuclear parameters of the RNS configurations can be met through the use of a suitable test tank in the ASTR facility. A typical PHT arrangement was developed and its fluid dynamic and thermodynamic characteristics were shown to be similar to those predicted for the RNS flight configuration that it represented.

TABLE OF CONTENTS

TABLE OF CONTENTS (Cont'd)

TABLE OF CONTENTS (Cont'd)

TABLE OF CONTENTS (Cont'd)

TABLE OF CONTENTS (Cont'd)

LIST OF FIGURES

LIST OF FIGURES (Cont'd)

LIST OF FIGURES (Cont'd)

LIST OF TABLES

I. INTRODUCTION

Contract NAS8-25848 was undertaken at the Nuclear Aerospace Research Facility (NARF) of the Fort Worth operation at the direction of, and under contract to, the George C. Marshall Space Flight Center, National Aeronautics and Space Administration. The work performed, which was an extension of previous Fort Worth operation efforts in support of the nuclear rocket vehicle development program, was directed toward two primary tasks: (1) redesign of the Propellant Heating Experiment, and (2) a radiation effects analysis of Saturn V materials, systems, and components. This report documents and discusses the work accomplished under Task I. Task II results are documented in General Dynamics Convair Aerospace Division report FZK-378.

The objective of Task I was to revise the analytical data and experiment designs previously generated under Modification 2 of Contract NAS8-18024 (Ref. 1) to conform with the new concepts of the Nuclear Flight Systems being generated under Contracts NAS8-24714 with McDonnell Douglas Astronautics Co. (Ref. 2), NAS8-24715 with Lockheed Missiles and Space Co. (Ref. 3), NAS8-24975 with Space Division, North American Rockwell (Ref. 4), and SNP-1 with Aerojet Nuclear Systems Co. (Ref. 5). This report documents and discusses work performed under Task I during the period 21 May 1970 through 21 May 1971, and includes the

Task I work reported in the first, second and third quarterly progress reports (Refs. 6 through 8).

Completion of Task I has resulted in the design of a ground experiment in which a simulated Reusable Nuclear Shuttle (RNS) propellant tank containing liquid hydrogen is exposed to a nuclear radiation field. The program plan for this study is shown in Figure 1-1. The experiment synthesis and design of this propellant heating test (PHT) was conducted in a manner that will allow one to: (1) establish the amount of nuclear energy deposited in liquid hydrogen for well-defined nuclear environments, (2) identify the associated changes in the fluid dynamic and thermodynamic state of the fluid, and (3) provide experimental data for comparison with the various propellant heating analyses developed to predict nuclear heating effects in liquid-hydrogen-fueled nuclear flight systems.

The nuclear factors studied and evaluated during this program consisted of (1) the method of calculation of nuclear energy deposition in liquid hydrogen, and (2) the nuclear heating that occurs in the various RNS configurations during engine burn and in the NARF test module. The details are presented in Section II.

The drain-temperature profiles and pressurization requirements for four baseline RNS configurations were determined for a typical lunar shuttle mission. Parametric data were obtained by varying the pertinent stage operation parameters over a wide

NERVA-2 NFM DATA AND RESULTS
FROM NAS8-18024

NASA
GUIDELINES

UPDATE COMPUTED
CODES
• AG-4
• RI-0
   • Incorporate
     Required Pro-
     cedural and
     Geometric
     Changes

RNS-LUNAR SHUTTLE
MISSION FLUID AND
THERMODYNAMIC
PHENOMENA
 • Drain
   Temperature
 • Pressurization
   Requirements

PARAMETERIZATION
VARIABLES
 • Drain Rate
 • Bottom-to-Sidewall
   Heating Ratio
 • Liquid Level
 • Pressurization
   Level
 • Acceleration

PHT TANK DESIGN
 • Tank Configurations
 • Axuiliary Tank
   Heater Requirements
 • Facility Require-
   ments

FINAL
REPORT

NUCLEAR FLIGHT SYSTEM STUDIES

FLUID FLOW VISUALI-
ZATION EXPERIMENT
 • Heat Shorts
 • Bulk Mixing-
   Boundary Layer
   Interaction

Figure 1-1   Program Plan for Redesign of the Propellant Heating Test

range of values. The results of this analysis are discussed in Section III.

The scaling and simulation analysis and the resulting experiment synthesis and design are presented in Section IV. A small-scale fluid-flow visualization experiment was conducted. The objective of this test was to determine, in a qualitative manner, the effects of heat leaks and tank-bottom geometry on the propellant fluid dynamics.

Section V contains a summary of the flow visualization experiment results and a description of the experimental equipment.

The conclusions reached in the various studies conducted under Task I and recommendations for future action are given in Section VI.

II. NUCLEAR FACTORS

The most recent data available on the nuclear environment of the 1575-MW NERVA have been used in calculating the nuclear heating in the liquid hydrogen bulk and tank sidewall. The method of calculation and the nuclear heating occurring in the various RNS and test module configurations are discussed in the following subsections.

2.1 Calculation of Nuclear Energy Deposition in Liquid Hydrogen

2.1.1 Method of Calculation

The nuclear heating rates required for the performance of Task I were calculated by methods which provide a degree of accuracy appropriate to the requirements of these particular studies and which allow the generation of rather extensive and detailed data as economically as possible. The gamma ray and neutron source terms were obtained by representing the Aerojet Nuclear reference data (Ref. 5) in terms of a few non-isotropic point sources. Attenuation in liquid hydrogen was calculated by the use of infinite-medium buildup factors derived from moments method data; this method was checked and monitored for accuracy by comparison with calculations based on single scattering with infinite-medium buildup on the second leg.

2.1.2 Unattenuated Full-Flow Gamma Dose Rates and Neutron Fluxes

The Aerojet data on unattenuated gamma dose rates were extended by locating a small set of non-isotropic source points in the vicinity of the reactor core, which, given appropriate directional strengths, reproduced the given isodose curves. The dose rate was assumed to fall off as distance squared along a given direction relative to a source point. A differential analysis shows that for detector positions lying more than 250 in. from the core center, the unattenuated dose rate can be attributed to a single non-isotropic source at the core center, with an accuracy of about 20% or better. The unattenuated gamma dose rate ranges from about 6×10^7 erg/gm(C)h at the tank bottom to about 1×10^6 erg/gm(C)h at the top of a typical configuration.

Neutron isoflux lines from the Aerojet data (Ref. 5) were extended in the same way as for gamma-ray dose rate, i.e., by the use of effective non-isotropic point sources. The empty-tank fast-neutron flux levels range from 1×10^{11} n/cm^{2}sec at 200 in. above core center to about 2×10^9 n/cm^{2}sec at the top of a typical configuration.

2.1.3 Gamma-Ray Attenuation in LH$_2$

Figure 2-1 shows a set of arbitrarily normalized points taken from SHADRAC results on gamma-ray attenuation in liquid
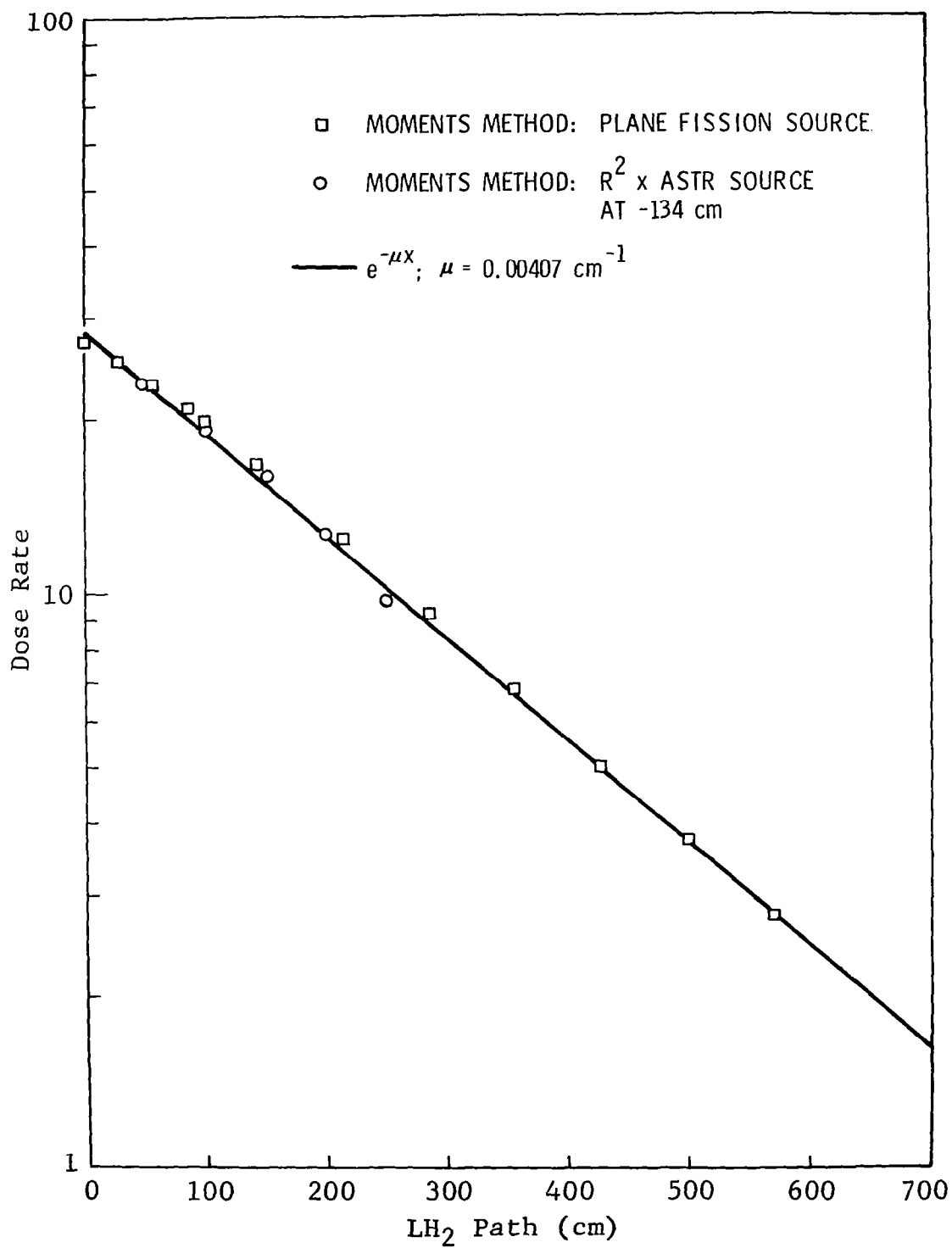
Figure 2-1   Gamma-Ray Attenuation in an Infinite LH$_2$ Medium

hydrogen. The squares correspond to a plane fission source. The circles represent the distance-squared weighted dose rate from the ASTR situated only 134 centimeters below the hydrogen surface. The two sets of data are essentially exponential and have nearly the same effective removal coefficient. This comparison shows that gamma-ray dose rate attenuation in an infinite liquid hydrogen medium is rather insensitive to the detailed shape of the incident spectrum; which result is supported by transport-theory considerations for a case where pair production is absent and where the gamma spectrum decreases with increasing energy but is non-vanishing over a fairly extensive range of energy. On the basis of estimated gamma spectra from NERVA at various emergence intervals, it is concluded that the indicated removal coefficient should give a dose rate accuracy to 30% over two decades of gamma attentuation in an infinite medium of liquid hydrogen.

The limitation on the validity of constant removal cross sections in liquid hydrogen derives less from spectral hardening than from the fact that the infinite-medium assumption is not necessarily applicable to large penetrations through small-angle conical volumes. In the case of hydrogen propellant tanks, unattenuated gamma rays reaching the wall at points well above the tank bottom may be scattered in the direction of an on-axis detector point thereby contributing more dose at that

point than would be inferred on the basis of infinite medium attenuation. However, at detector points not far above the bottom of the tank this "short-circuit" effect is small, since the large scattering angles involved imply low differential cross sections and low scattered gamma-ray energies. Calculations based on single scattering with infinite-medium buildup on the second leg show that the underestimate resulting from the infinite-medium buildup assumption does not exceed 15% in the propellant regions where nuclear heating and cumulative dose are considered to be significant. Hence, the SHADRAC results have been used to describe gamma-ray dose buildup in these studies.

2.1.4 Fast-Neutron Attenuation in LH$_2$

Figure 2-2 shows that, according to moments method results, the dose due to a plane fission source of neutrons falls off in a roughly exponential fashion in liquid hydrogen. The fast neutron attenuation is, of course, much more sensitive to the shape of the incident spectrum than that of gamma rays. However, a rough estimate of the rate of neutron energy relaxation is actually all that is required for these studies.

The neutron heating and cumulative dose at internal points in a hydrogen tank is negligible compared to that of gamma rays. It is only in regard to boundary-layer heating that neutrons are significant, and even in this context the
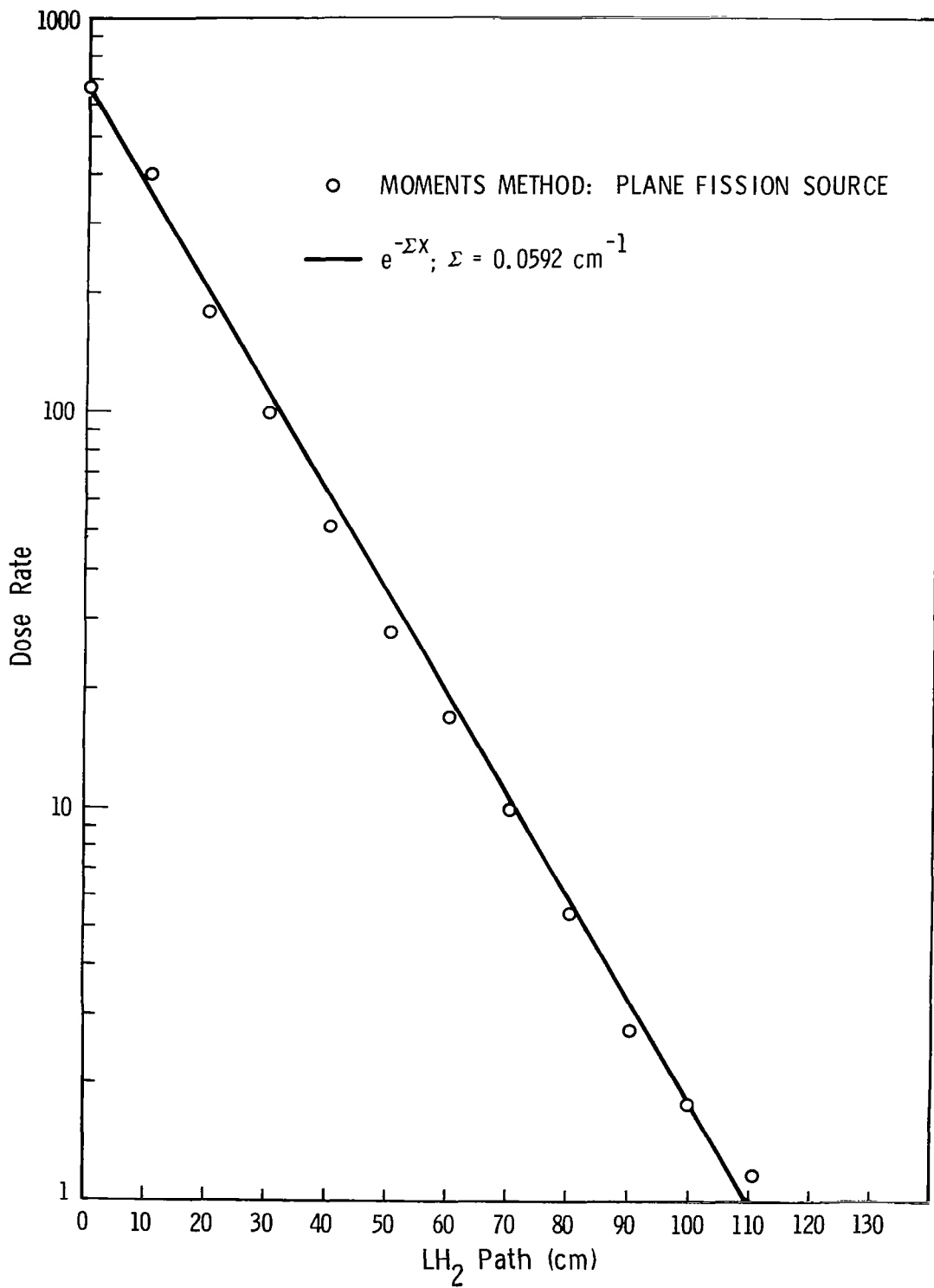
Figure 2-2   Fast-Neutron Attenuation in an Infinite LH$_2$ Medium

propellant heating program uses the dose rate relaxation parameter only to evaluate an integral involved in the boundary-layer energy balance. Since the value of this integral is insensitive to the rate of neutron relaxation (except for very thin boundary layers), a constant removal cross section is considered adequate for the purpose. As far as the program is concerned, the total neutron energy flux at a given wall position is more significant than the details of neutron attenuation.

2.1.5   Bulk Heating of LH_2 by Gamma Rays

The asymmetric propellant heating program assumes a radially homogeneous bulk liquid. Hence, the appropriate input for bulk energy deposition by gamma rays is a radial average given by

$$\dot{Q}_b^\gamma(Z) = 2.39 \times 10^{-9} \left[\int_0^{R_Z} 2\pi r D(r,Z) dr \right] / \pi R^2(Z)$$

where Z is the height above the base of the tank and R is the tank radius at height Z. The coefficient converts the energy deposition from rad(C)/h to Btu/lb(H_2)-sec. The point energy deposition rate is approximated by

$$D(r,z) = D_0(r,z) \exp\left[-\mu s(r,z)\right]$$

where for convenience the point height is referred to the core center. The function $D_0(r,z)$ is the unattenuated dose rate at

2-7

(r,z), s(r,z) is the slant path through hydrogen for gamma rays reaching (r,z), and μ is the effective removal coefficient.

2.1.6 Radial Variation of Gamma-Ray Energy Deposition

The radial distribution of dose rate in a given liquid hydrogen layer is often quite nonuniform. Figure 2-3 shows the radial distribution of dose rate for various layer heights in the 174-in.-diameter modular configuration propulsion module. Each curve represents a layer at a given height Z above the tank bottom and terminates at an r-value equal to the tank radius at that height. In the case of a liquid hydrogen layer 60 in. above the tank bottom, it is seen that the dose rate increases by a factor of about 5 from the axis to the wall. In this configuration the radial increase results mainly from the fact that outer points are not in the shadow of internal shield. In view of this radial variation, it is conceivable that the heating program underestimates the cumulative boundary layer heating by radially homogenizing the energy deposition and thereby overestimating the rate of heat loss to the bulk fluid.

2.1.7 Boundary-Layer Heating by Neutrons

In addition to bulk nuclear heating, the asymmetric propellant heating program accounts for direct heating of the boundary layer, which effect is predominantly due to the rapid attenuation of the neutron flux just inside the tank walls. Actually,
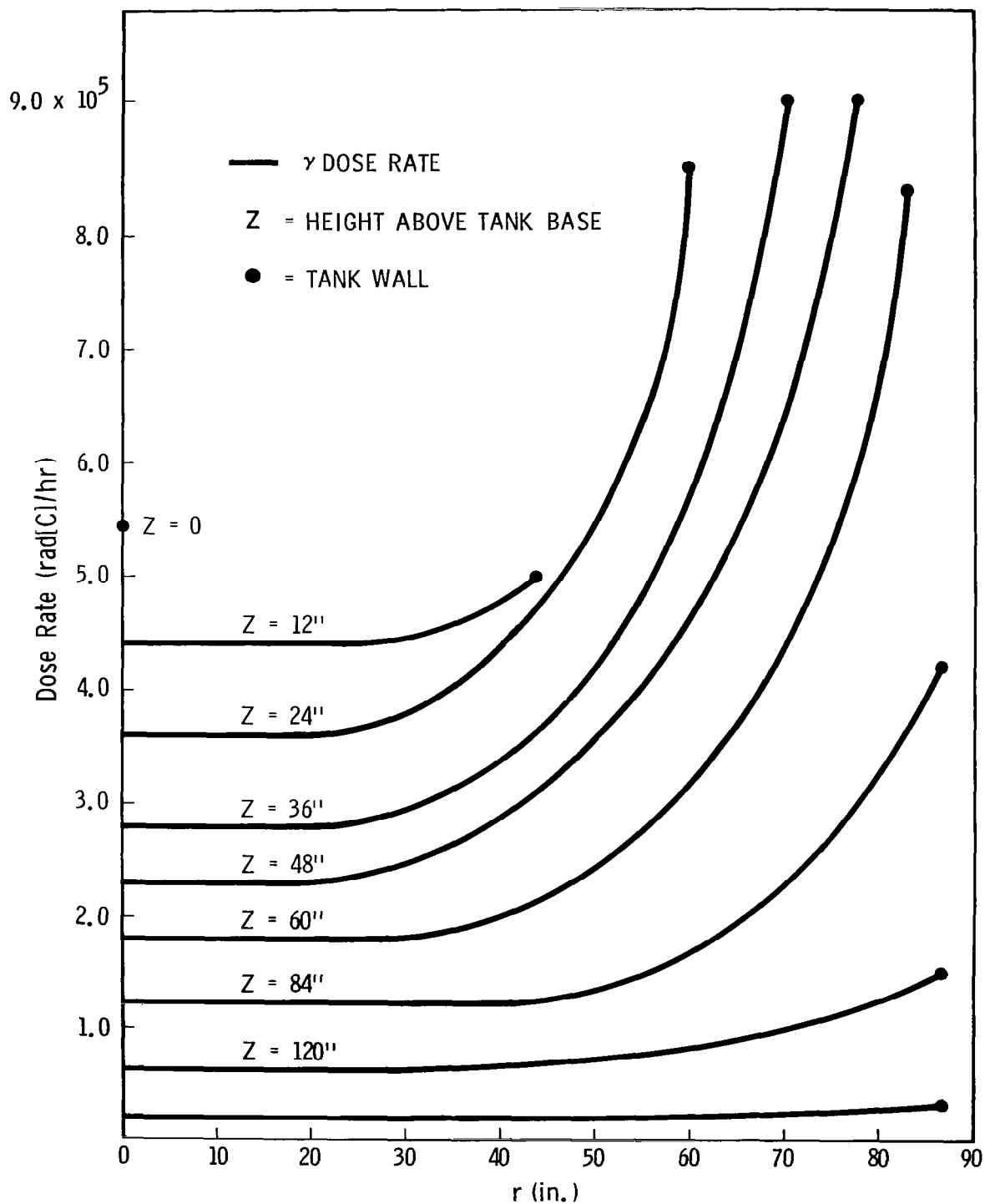
Figure 2-3   Radial Dose Rate Distribution for 174-in.-
Diameter Propulsion Module (Full tank)

two different energy deposition distributions are required.
The distribution used by the program in evaluating the boundary-
layer energy balance is

$$\dot{q}_N(y) = q_Z \exp\left[-q_e y\right]$$

where $\dot{q}_N$ is a point energy deposition rate per unit volume, q_Z
is the value of $\dot{q}_N$ at the wall, y is distance along an inward
normal to the wall, and q_e is an energy relaxation coefficient.
On the other hand, the overall neutron heating, which must be
added to the bulk gamma heating for a given layer, is described
in terms of a dimension normal to the vehicle axis. The latter
distribution is given by

$$\dot{q}_N'(r) = q_Z \exp\left[-(q_e/\sec \beta)r\right]$$

where β is the angle between a vector normal to the wall at a
given point and a vector normal to the vehicle axis.

The wall deposition rate for each distribution is given by

$$q_Z(R,z) = 5.18 \times 10^{-13} \phi$$

where ϕ is the fast-neutron flux in n/cm^2-sec and the coeffi-
cient expresses the corresponding energy deposition rate in
Btu/ft^3-sec. The energy relaxation coefficient in each distri-
bution at a wall point (R,z) is given by

$$q_e(R,z) = \Sigma\left[1-(\hat{r}\cdot\hat{e})^2\right]^{-\frac{1}{2}}$$

$$= \Sigma \sqrt{\left[1+(z/R)^2\right]\left[1+\sigma^2\right]}\Big/\left[(z/R)-\sigma\right]$$

where Σ is a neutron removal cross section, $\hat{r}$ is a unit vector

in the direction of neutron incidence, $\hat{\epsilon}$ is a unit vector
parallel to the wall and in the plane of the vehicle axis, and
$\sigma = dz/dR$ is the wall slope at (R,z).

The calculated parameters q_Z and q_e are included in the
input to the heating program. The neutron contribution to
bulk heating, $\dot{Q}_b^n$, is obtained by integrating over the distribu-
tion $\dot{q}_N'$. An adequate approximation to the result for the
boundary layers of interest is

$$\dot{Q}_b^n(z) = (0.458/R) \left[\sqrt{1+\sigma^2} / \sigma \right] (q_Z/q_e)$$

where the coefficient expresses the bulk heating in Btu/lb(H_2)-
sec with R in inches. The total bulk heating for a layer is
then given by

$$\dot{Q}_b = \dot{Q}_b^\gamma + \dot{Q}_b^n$$

where $\dot{Q}_b^\gamma$ is defined in Section 2.1.5.

2.2 Nuclear Heating

The nuclear heating data required by the propellant heat-
ing codes (Ref. 9 and 10) are described in the following subsec-
tions. The four baseline RNS configurations are shown in Figures
3-1 through 3-4.

2.2.1 Single Tank - 8° Conical Bottom

Figure 2-4 shows calculated heating rates and boundary -
layer parameters for a single tank with an 8° conical aft bulk-
head. The data along the axis indicate the layer positions

$\dot{Q}_b$ (*) and $\dot{Q}_w$ (*) table (left); q_z (**) and q_a (ft^{-1}) table (right):

$\dot{Q}_b$ (*)	$\dot{Q}_w$ (*)	q_z (**)	q_a (ft^{-1})
0.02	0.01	0.009	103.2
0.02	0.01	0.010	98.4
0.03	0.02	0.011	92.4
0.05	0.02	0.013	86.4
0.07	0.02	0.015	81.6
0.10	0.028	0.017	75.6
0.15	0.033	0.019	70.5
0.22	0.040	0.022	66.0
0.35	0.053	0.027	60.2
0.55	0.075	0.032	55.2
0.70	0.09	0.035	51.6
1.26	0.11	0.039	49.2
4.36	0.68	0.044	4.16
		0.047	1.80

* = Btu/lb-sec x 10^{-3} ** = Btu/ft^3-sec

Z (in.)   r (in.)
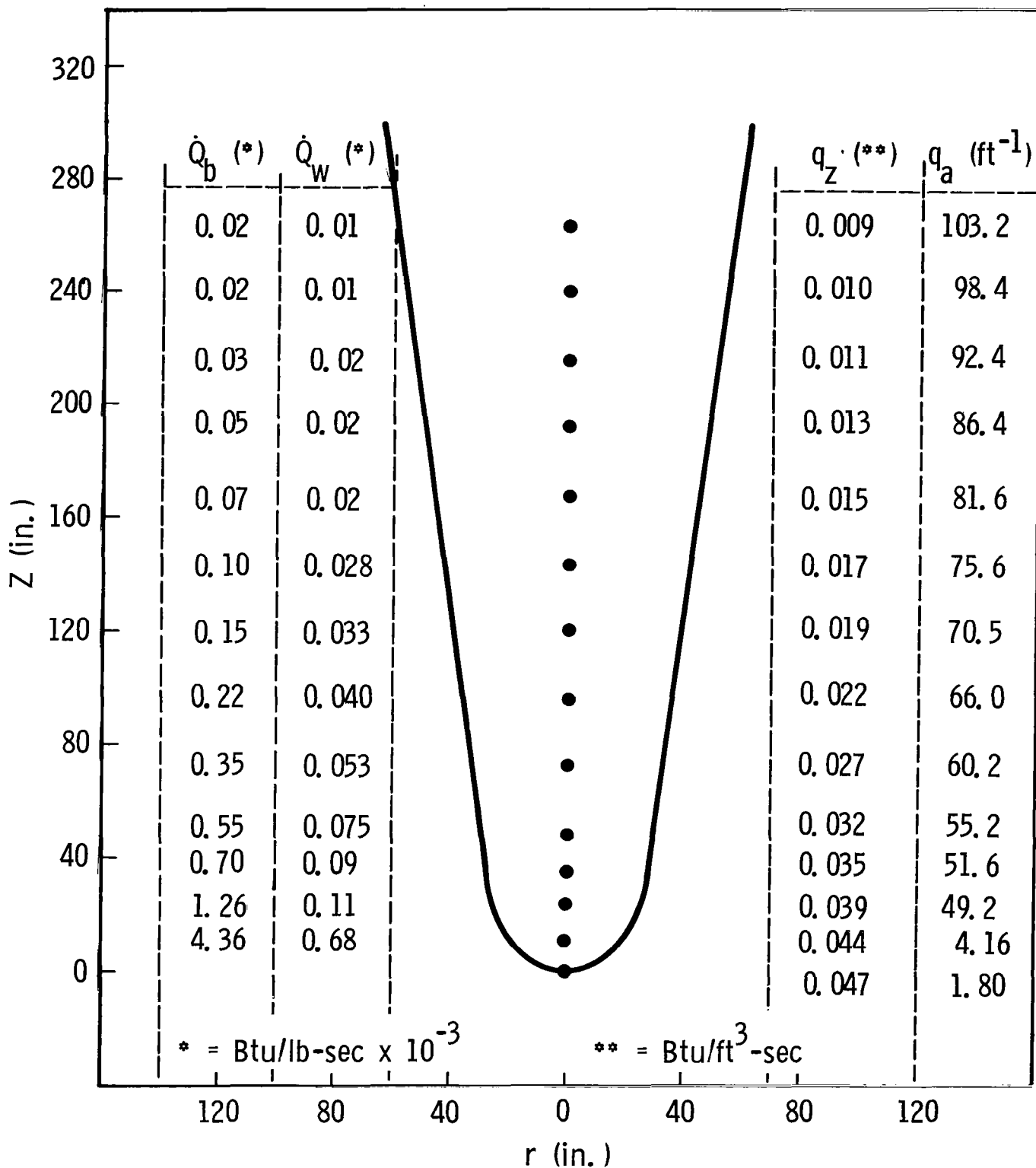
Figure 2-4   Nuclear Heating in Single Tank - 8° Conical Bottom

considered. The tabulated data include $\dot{Q}_b$ (Btu/lb(H$_2$)sec), the radially averaged heating rate in a differential layer at height Z above the tank bottom, $\dot{Q}_w$ (Btu/lb(Al)sec), the wall heating in a corresponding section of tank wall, and the two boundary-layer heating parameters that are entered as direct input to the heating program. In the case of the 8° cone, most of the liquid hydrogen lies within the shadow of the internal shield so that the radial heating distribution is relatively flat. The bulk heating falls from 4.36 x 10^{-3} Btu/lb-sec at a plane 1 ft above the tank bottom to 0.02 Btu/lb-sec at a plane 22 ft above the tank bottom. The bulk and wall heating values entered as input into the program are the cumulative heating rates shown in Figure 2-5.

2.2.2 Single Tank - 15° Conical Bottom

Figures 2-6 and 2-7 show the nuclear part of the heating-code input for a tank with a 15° conical aft bulkhead. The bulk-heating radial distribution is similar to that shown in Figure 2-3. At the lowest point, the bulk heating is relatively large due to the neutron contribution, which represents about 70% of the bulk heating at Z = 10 inches. At 240 in. the average bulk heating is down to 4 x 10^{-5} Btu/lb-sec. The magnitudes of the boundary-layer relaxation parameter, q_e, indicate that neutrons are totally absorbed at distances from the wall on the order of several inches. This value drops to about
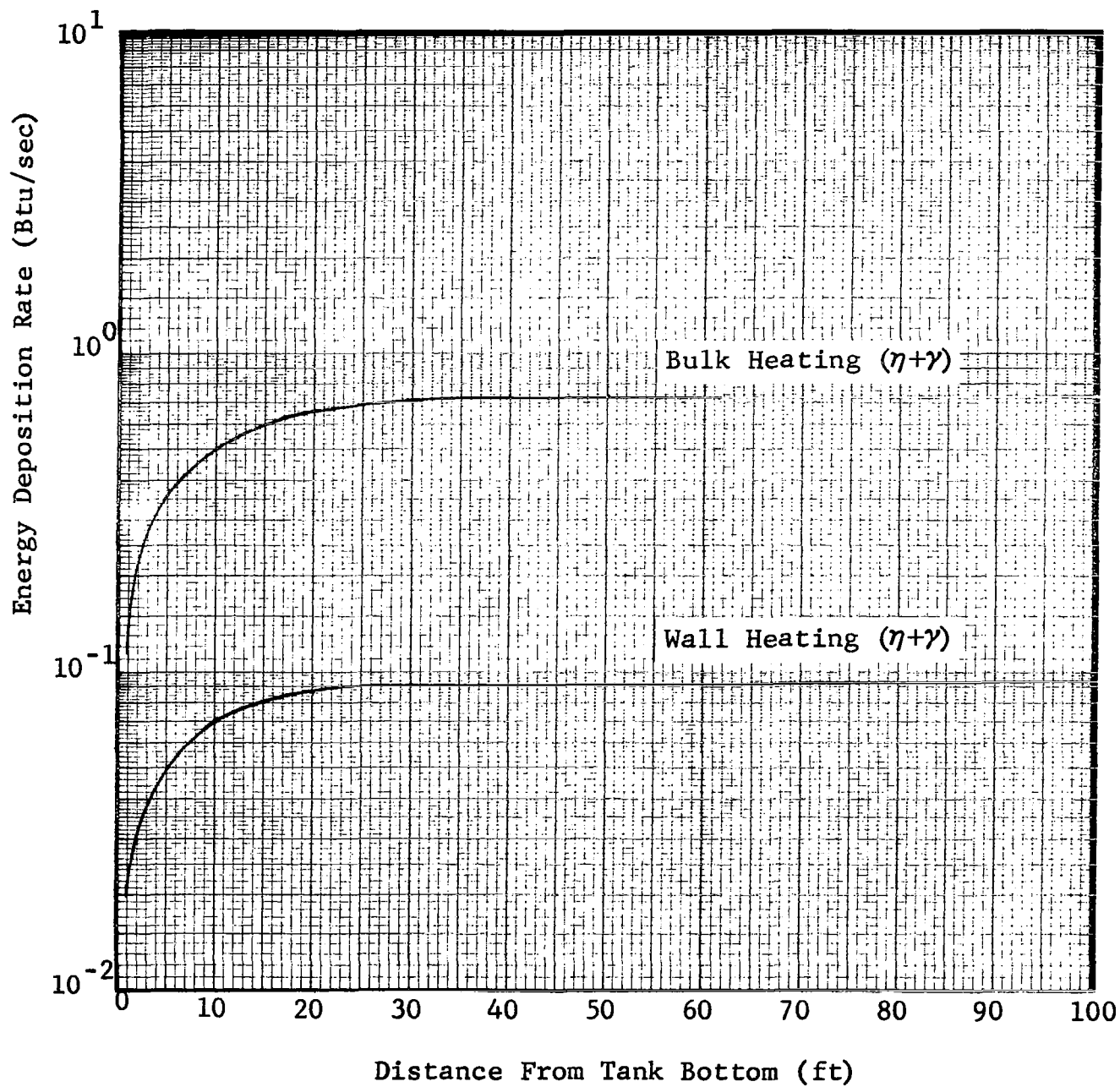
Figure 2-5   Nuclear Energy Deposition Rate - Single Tank 8° Conical Bottom Configuration
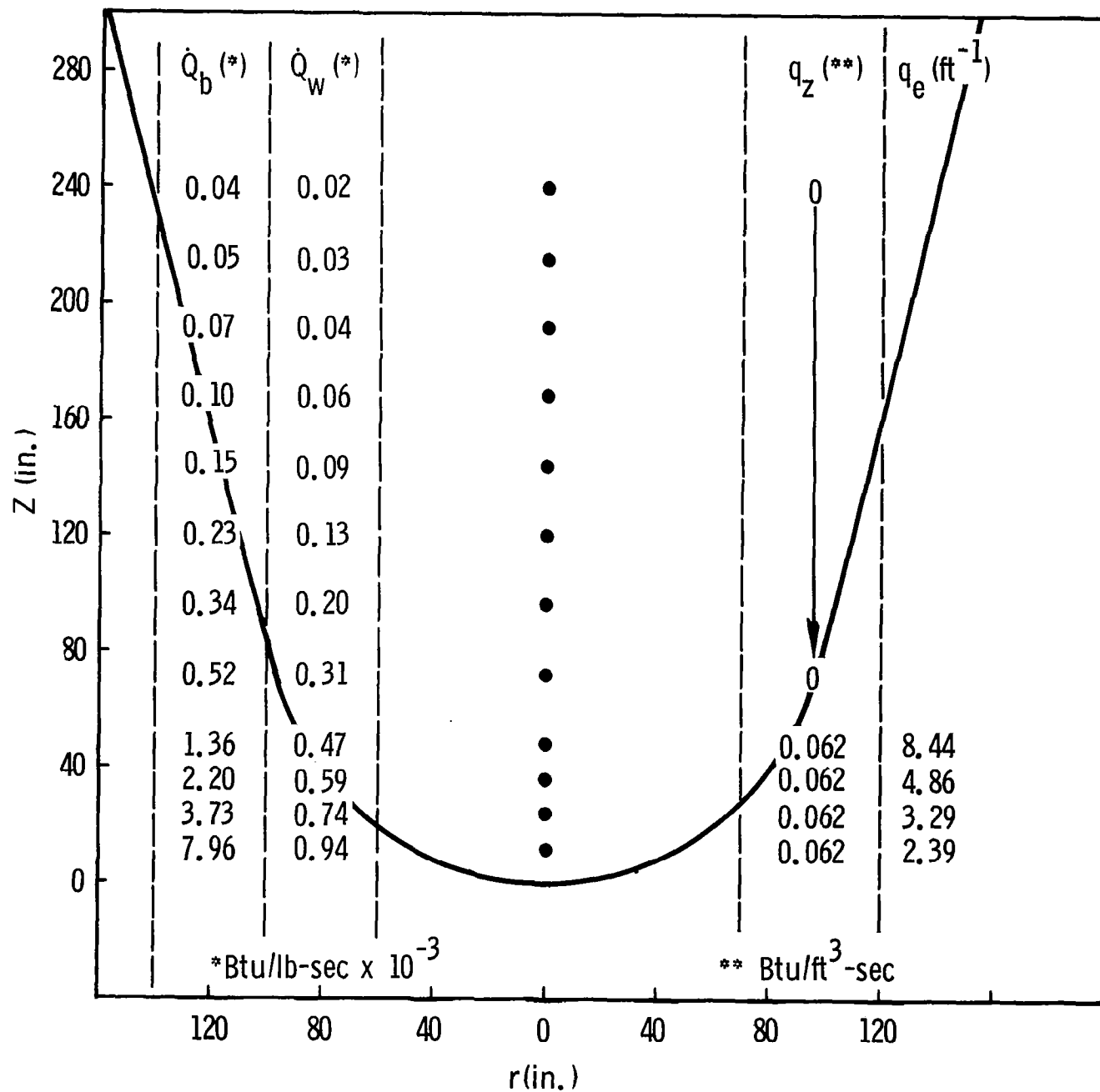
Figure 2-6 Nuclear Heating in Single Tank – 15° Conical Bottom
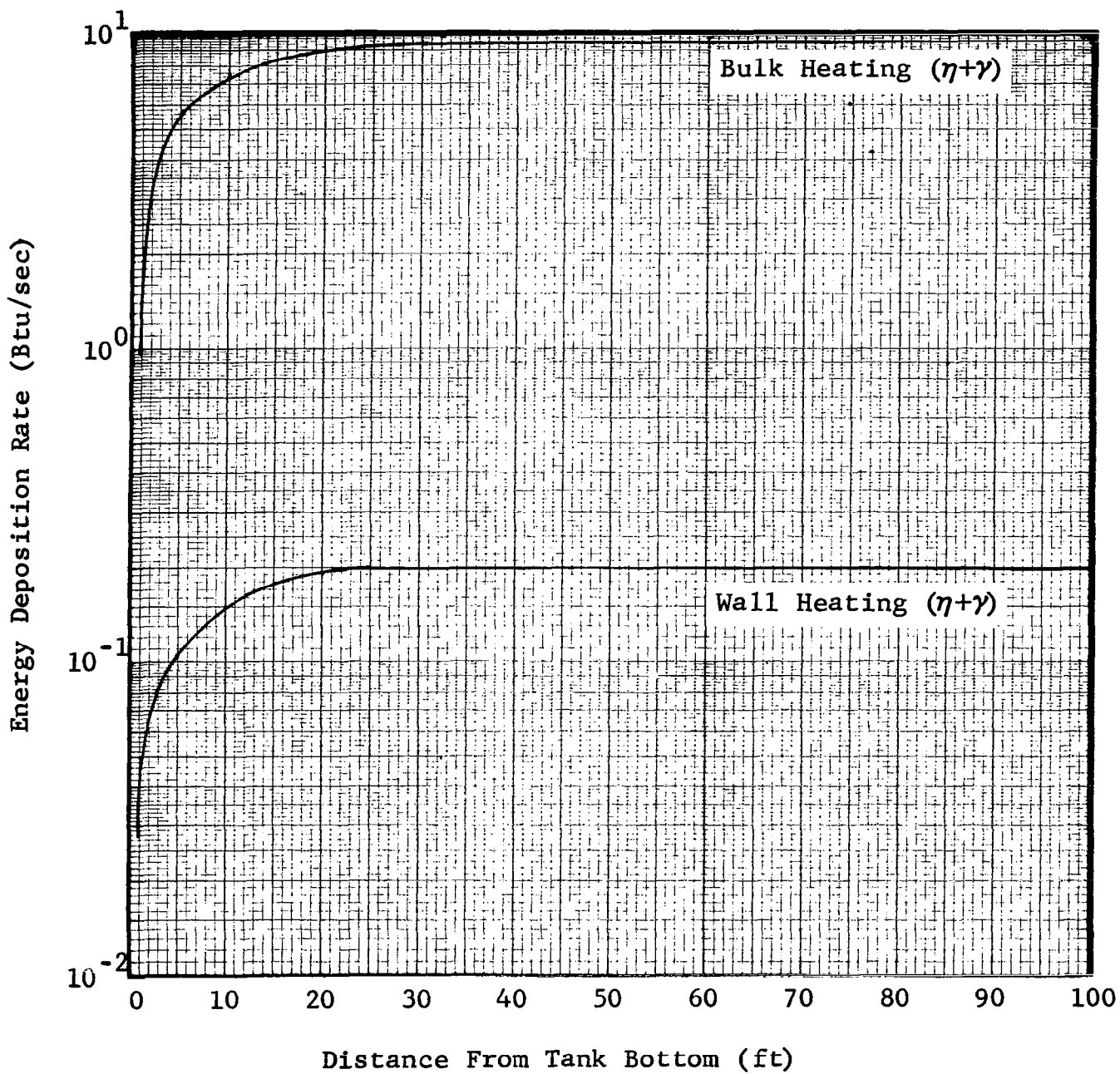
Figure 2-7   Nuclear Energy Deposition Rate - Single Tank 15°
Conical Bottom Configuration

2 in. at points where the angle between wall and the neutron incidence direction is small. The accumulative heating rate for the 15° configuration is given in Figure 2-7.

2.2.3 Hybrid Propulsion Tank

Figures 2-8 and 2-9 show the heating rate distribution and accumulative heating rate distribution, respectively, in the 160-in.-diameter propulsion module of a selected hybrid configuration. The accumulative bulk heating is about 40% less than in the case of the 15° single tank owing to the smaller proportion of hydrogen that lies outside the shadow of the internal shield.

2.2.4 Modular Propulsion Tank

Figures 2-10 and 2-11 show the nuclear input data for a 174-in.-diameter propulsion module of the modular RNS configuration. The data are similar to those for the 15° conical case. The bulk heating rate at 240 in. is some 25% less in the module owing to the fact that the smaller maximum radius does not place as much hydrogen outside of the shadow of the internal shield at the axial position. However, because of a slightly larger tank radius in the region where neutron heating is significant, the accumulative heating is approximately the same in the two configurations.

$$\dot{Q}_b \; (*) \qquad \dot{Q}_W \; (*) \qquad\qquad q_z \; (**) \quad q_e \; (ft^{-1})$$

z	$\dot{Q}_b$ (*)	$\dot{Q}_W$ (*)	q_z (**)	q_e (ft^{-1})
240	0. 024	0. 013	0	0
216	0. 038	0. 021	0	0
192	0. 056	0. 030	0	0
168	0. 093	0. 051	0	0
144	0. 13	0. 078	0	0
120	0. 21	0. 13	0	0
96	0. 37	0. 29	0	0
72	0. 60	0. 57	0	0
48	1. 15	0. 84	0. 050	14. 55
36	2. 00	0. 96	0. 052	5. 97
24	3. 15	0. 96	0. 049	3. 59
12	6. 01	0. 81	0. 047	2. 46

* = Btu/lb-sec x 10^{-3} ** = Btu/ft^3-sec

r(in.)

z(in.)
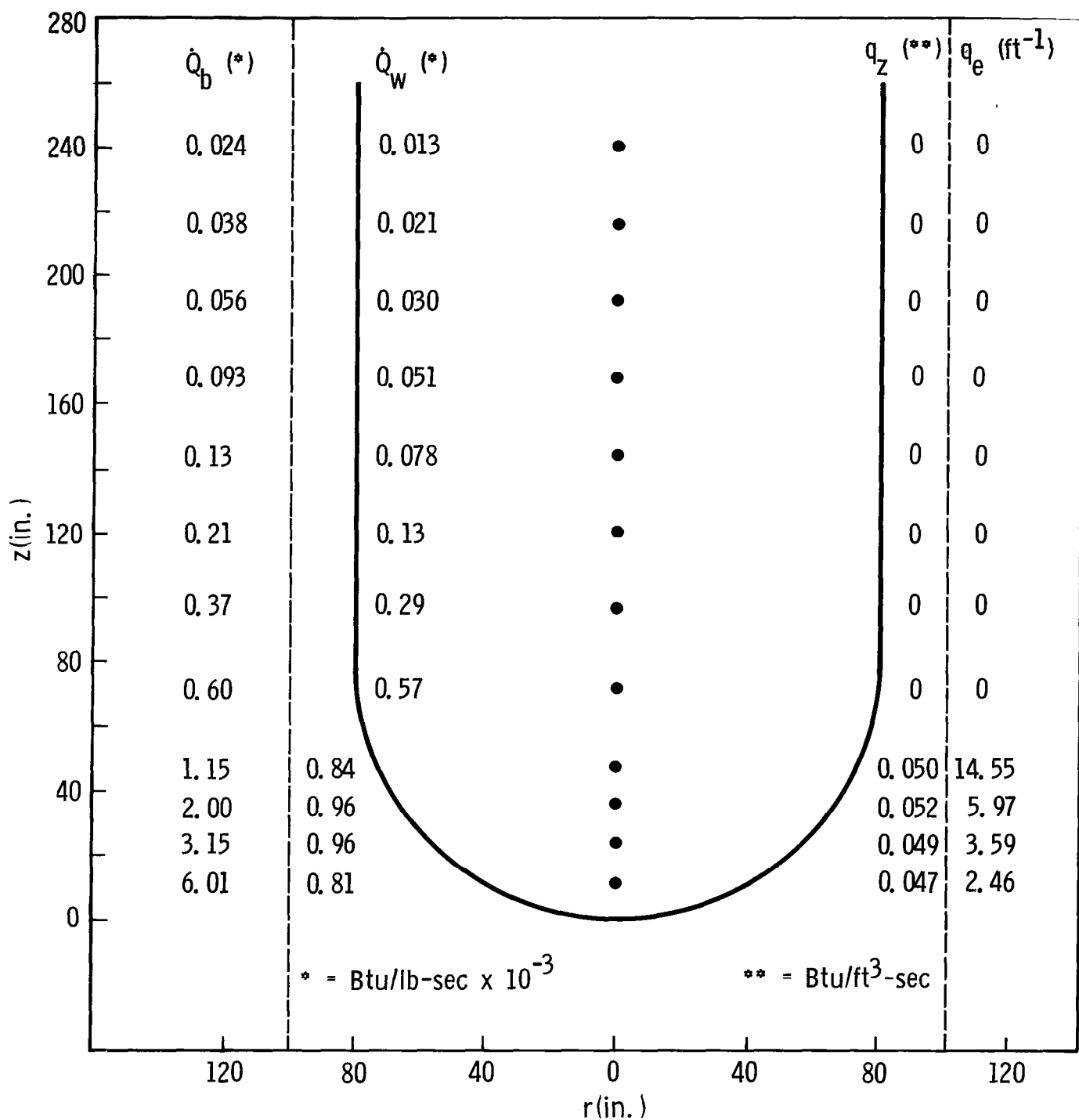
Figure 2-8   Nuclear Heating in Propulsion Tank-Hybrid Configuration

2-18
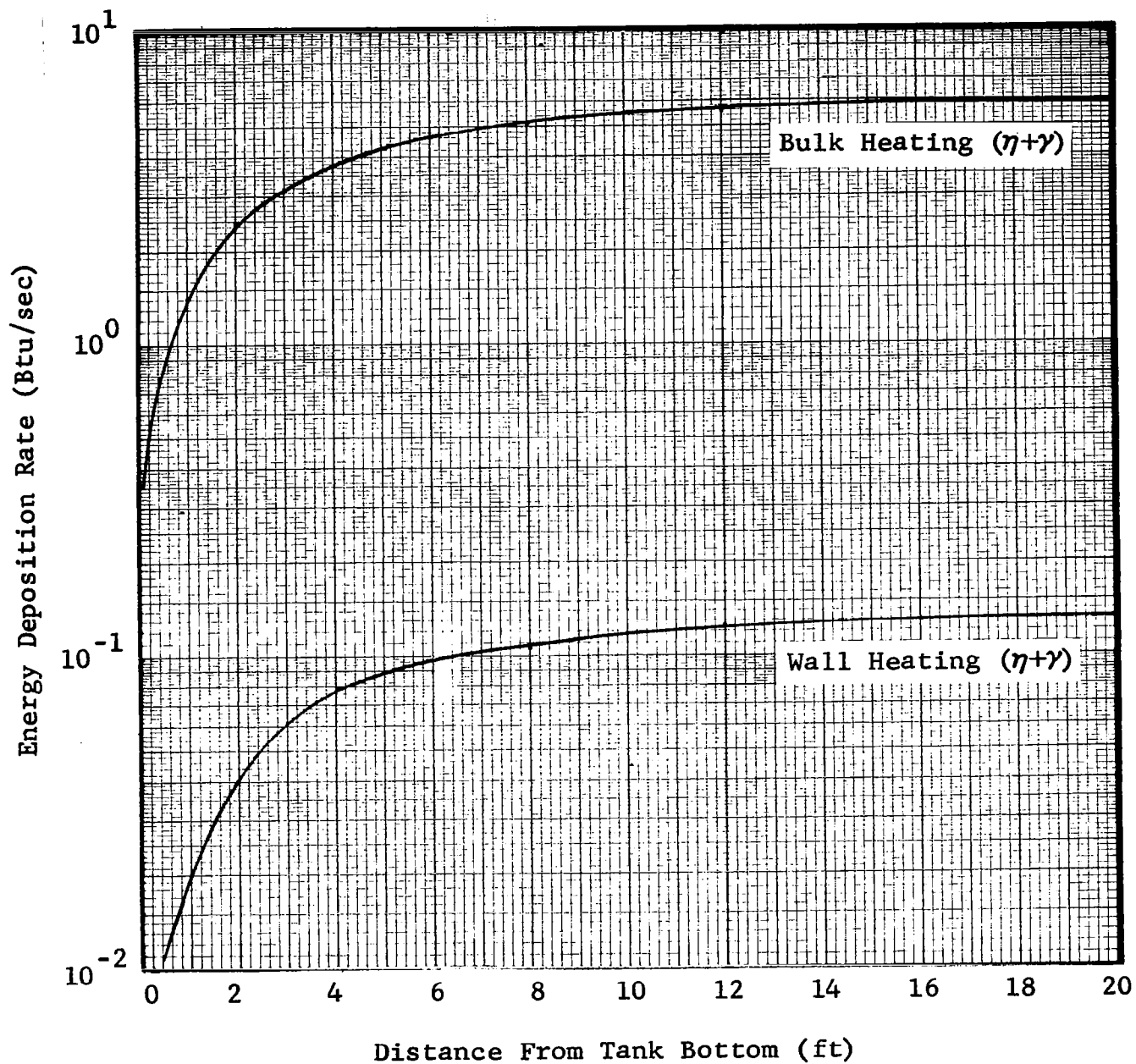
Figure 2-9   Nuclear Energy Deposition Rate - Propulsion Tank
             Hybrid Configuration
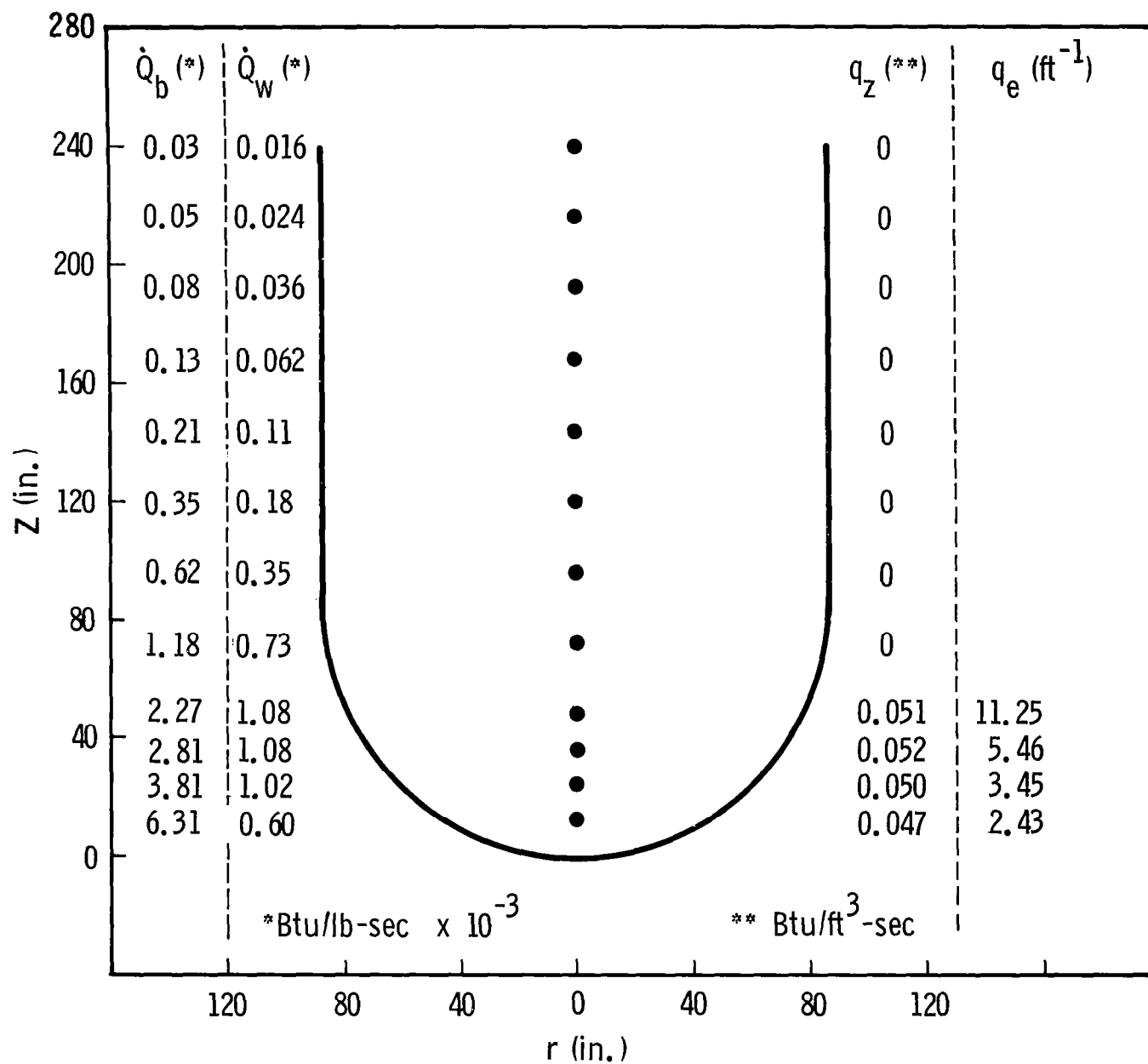
Figure 2-10 Nuclear Heating in 174-in.-Diameter Propulsion Module
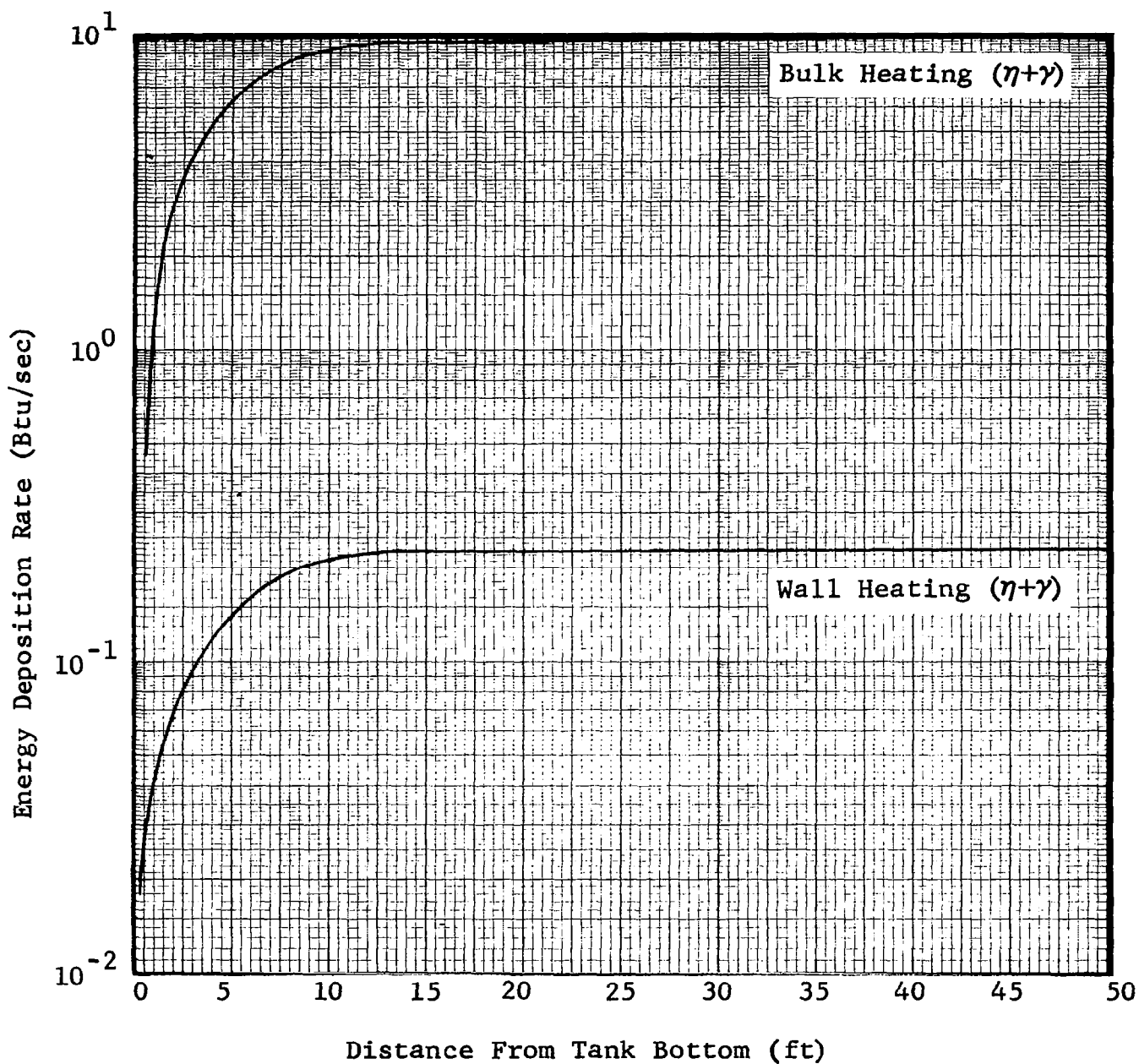
Figure 2-11 Nuclear Energy Deposition Rate - Propulsion
Module Modular Configuration

2.2.5 NARF Test Module

Figure 2-12 shows nuclear heating rates and boundary-layer parameters for the 160-in. NARF test module exposed to radiation from the ASTR at a power level of 1 MW. In the assume configuration, a detailed representation of which is shown in Figure 4-7, the tank bottom is situated 35 in. above the center of the reactor core. The heating rates were obtained from SHADRAC calculations which utilized a set of point fission sources distributed throughout the core volume of the reactor. Comparison of the accumulative heating rates shown in Figure 2-9 (160-in. module, NERVA configuration) and Figure 2-13 (160-in. module, ASTR configuration) shows that at 10 MW the accumulative heating in the ASTR experiment will differ from that in the NERVA hybrid configuration at full power by less than 20%.

$\dot{Q}_b$ (*)	$\dot{Q}_w$ (*)	q_z (**)	q_e (ft^{-1})	z (in.)
0.013	0.006	0	(0)	180
0.016	0.007	0	(0)	
0.020	0.009	0	(0)	160
0.025	0.010	0	(0)	140
0.031	0.012	0	(0)	
0.039	0.014	0	(0)	120
0.051	0.016	0	(0)	
0.064	0.019	0	(0)	100
0.084	0.024	0	(0)	80
0.12	0.035	0	(0)	
0.23	0.067	0	(0)	60
0.55	0.13	0.00083	6.62	
1.62	0.45	0.0028	2.96	40
3.29	0.95	0.0061	1.80	

* = Btu/lb-sec x 10^{-3}

** = Btu/ft^3-sec

$Z = z - 35$ in.

Tank Wall

ASTR

r (in.)
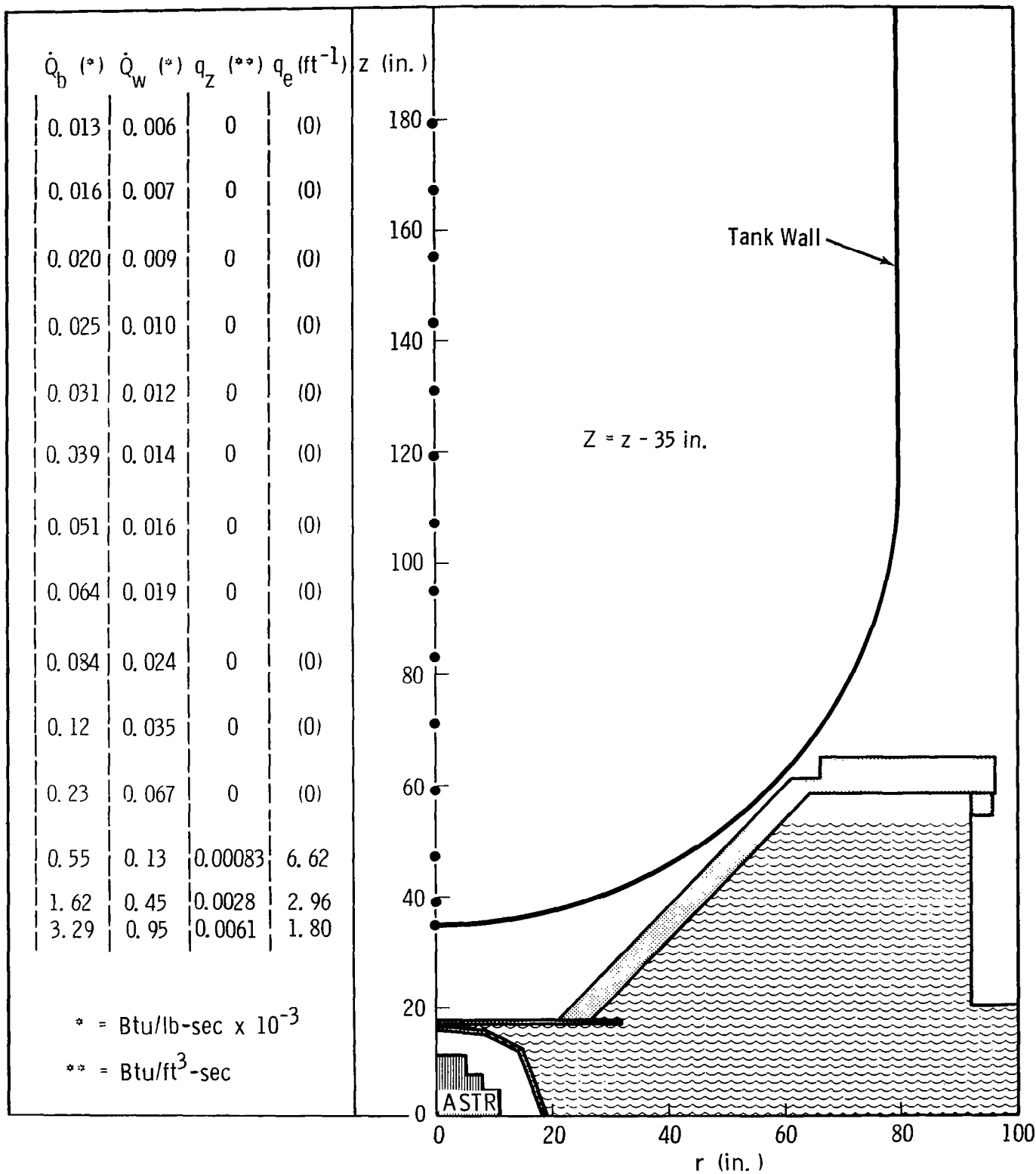
Figure 2-12   Nuclear Heating in NARF Test Module

2-23
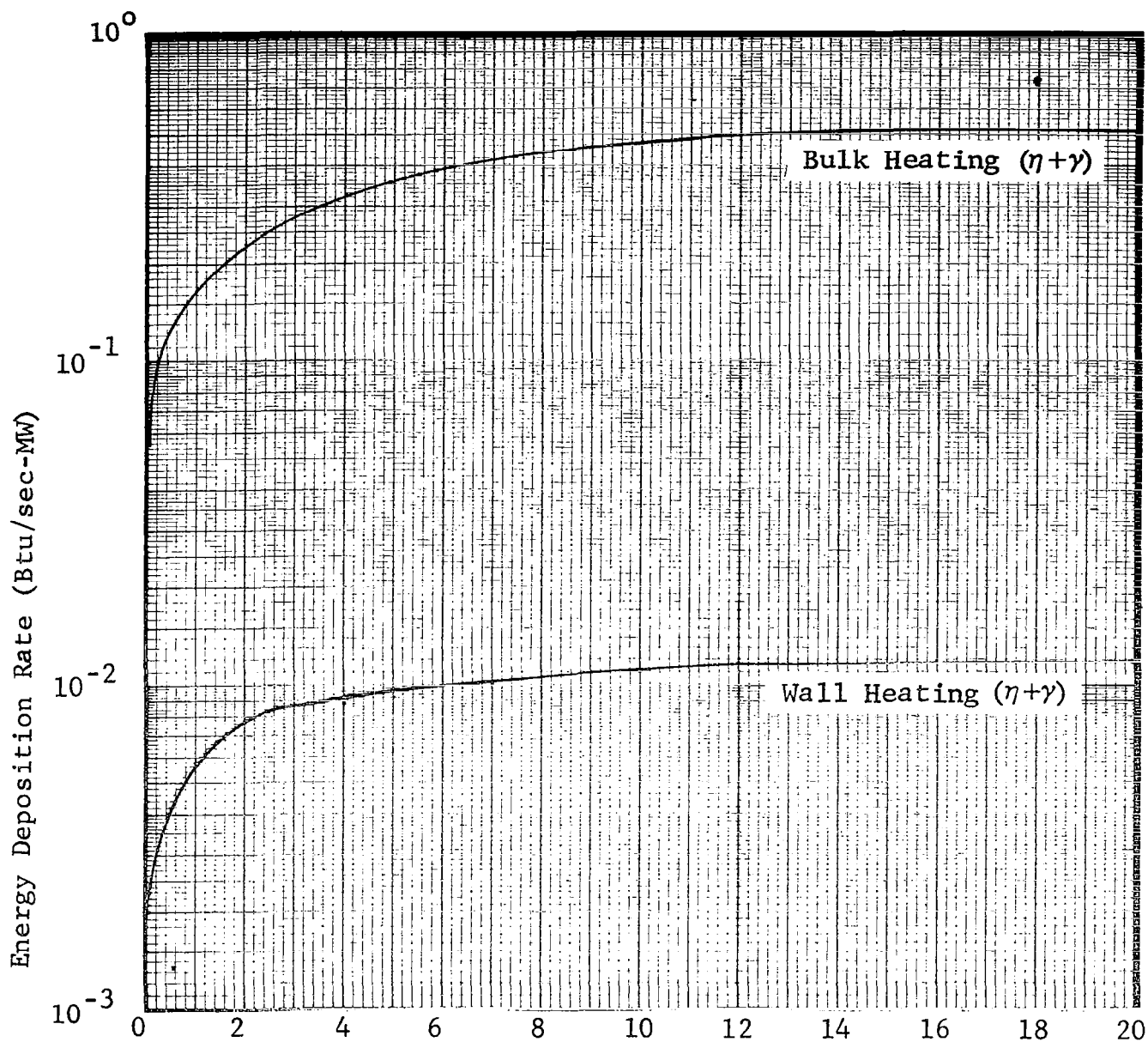
Figure 2-13   Nuclear Energy Deposition Rate in NARF Test Module

III. RNS ANALYSIS

Various RNS configurations were analyzed for a wide range of conditions in order to define the synergistic effects of ambient heating, nuclear heating, tank pressure, tank configuration, and acceleration on the thermodynamic and fluid dynamic phenomena occurring during engine firing. These analyses were conducted to provide the insight required to synthesize and design the propellant heating experiment. Further, the studies allowed the operating characteristics of the computer codes to be more fully understood.

3.1 RNS Configurations and Missions

The RNS configurations and missions developed by the Nuclear Shuttle Definition Study, Phase III contractors (Ref. 2 through 4) were used in defining the baseline tank configurations and mission segments used in the RNS analysis. A detailed description of these baselines is given in the following subsections.

3.1.1 Baseline RNS Configurations

The data presented at the interim briefings of Phase III of the Nuclear Shuttle Definition Study (Ref. 2 through 4) were used to define three basic propellant/propulsion tank concepts, namely, (1) single tank with conical aft bulkhead (2) two-tank hybrid, and (3) multiple-tank modular. Four tank configurations,

based on these three tank concepts, were then defined for use in the RNS analysis. The geometric details of these configurations are shown in Figures 3-1 through 3-4. In all cases the reactor core of the nuclear engine was assumed to be approximately 200 inches below the tank bottom.

Two conical-bottom single-tank configurations were defined in order to adequately cover the wide variation in cone angles under consideration by the various RNS study contractors. The 8° and 15° conical aft bulkhead configurations (Figures 3-1 and 3-2) are based on data presented by North American Rockwell Corporation (Ref. 4). These tanks have a nominal 300,000-pound LH_2 capacity with a 5-percent ullage.

The hybrid configuration shown in Figure 3-3 is one of the RNS concepts developed by the McDonnell Douglas Corporation (Ref. 2). The configuration consists of a propellant tank and a propulsion (run) tank. The tanks have a combined nominal capacity of 300,000 pounds with a 5-percent ullage.

The tank configuration shown in Figure 3-4 is representative of the tanks that would be used in an RNS modular concept compatible with the current Earth Orbit Shuttle cargo bay. The particular configuration shown was developed by Lockheed Missiles and Space Company (Ref. 3) and has a nominal capacity of 36,900 pounds of LH_2 with a 5-percent ullage.
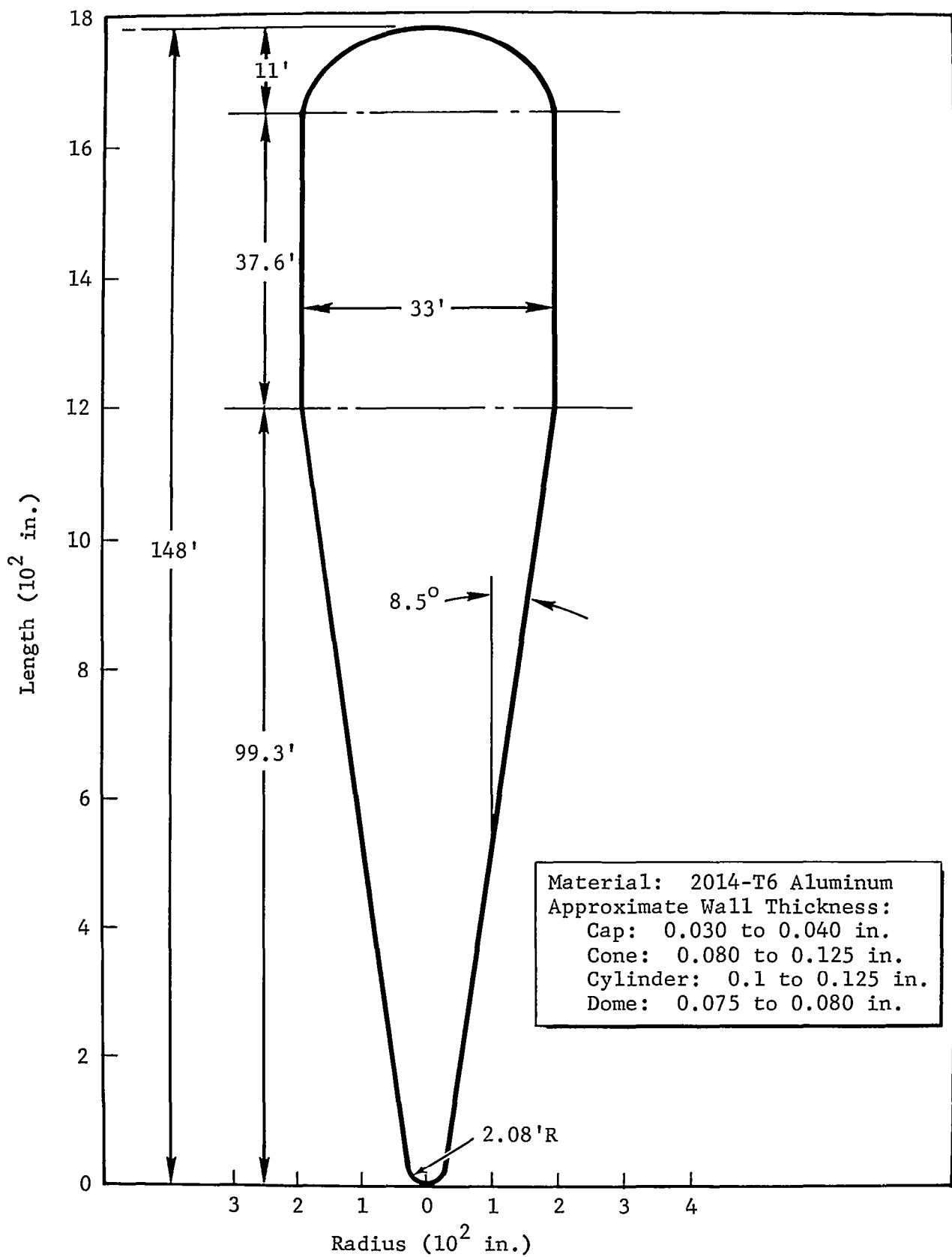
Figure 3-1 Single Tank Configuration with 8.5-Degree Conical
Aft Bulkhead
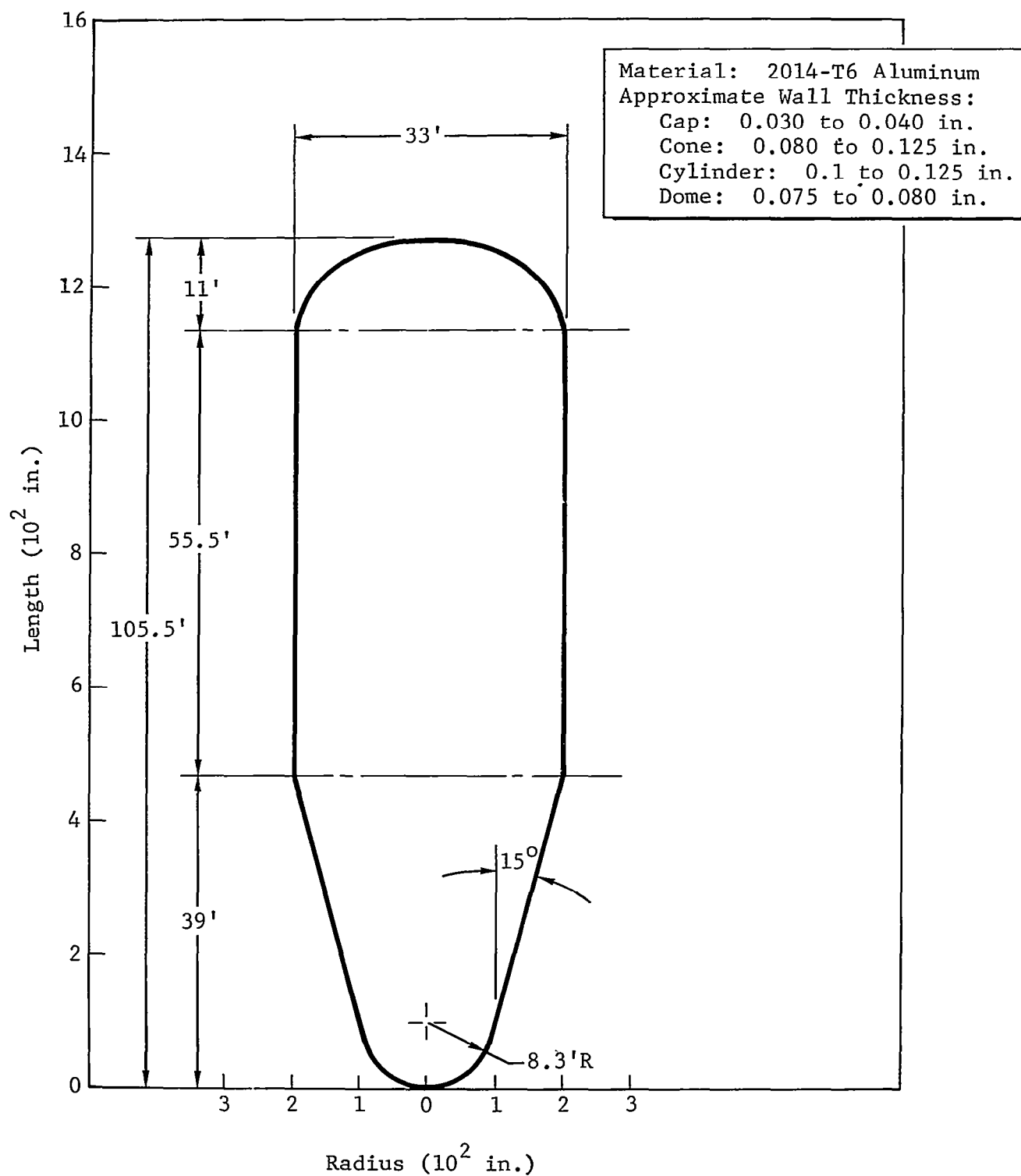
Figure 3-2 Single Tank Configuration with 15-Degree Conical
Aft Bulkhead
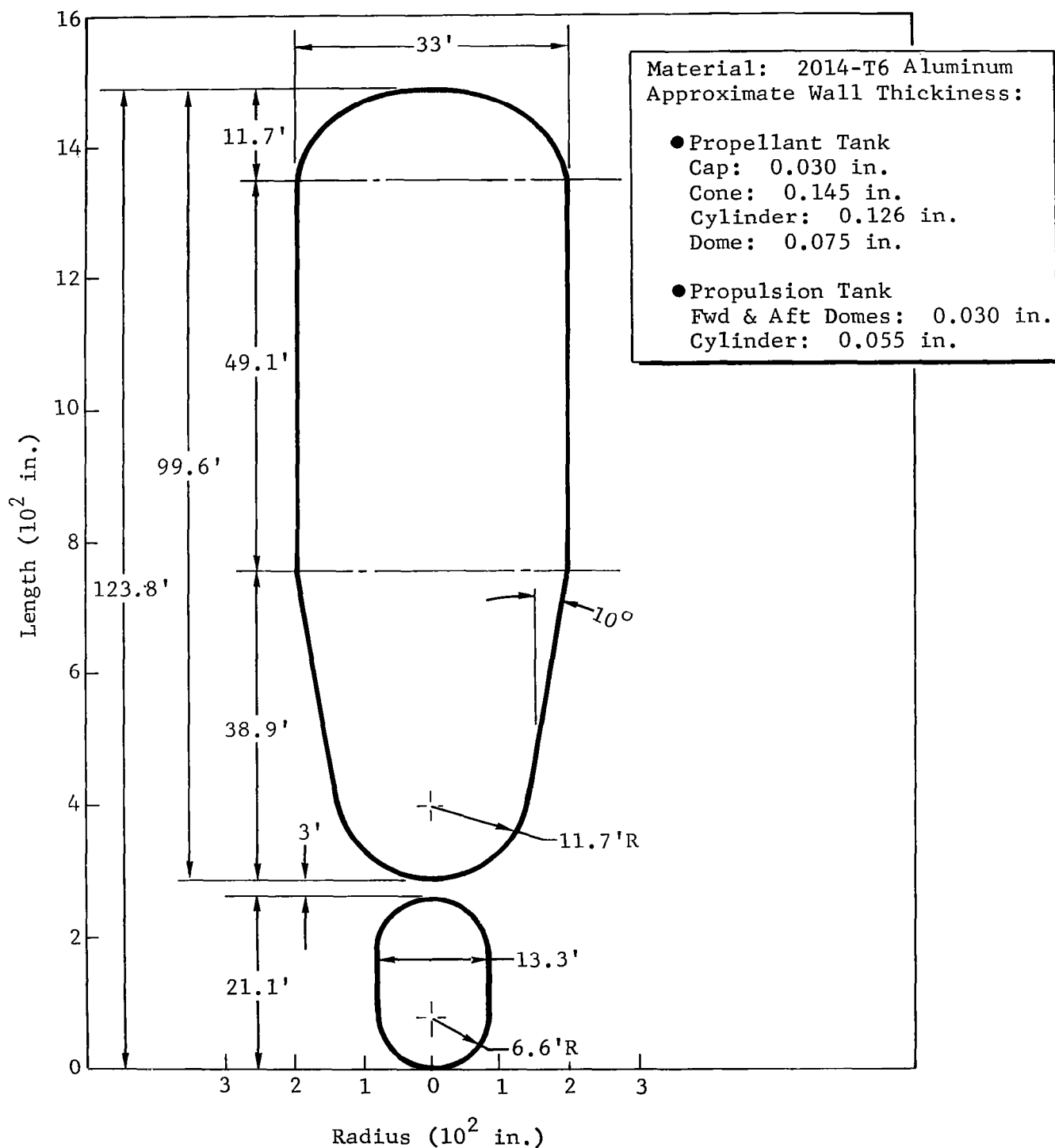
Figure 3-3   Hybrid Tank Configuration
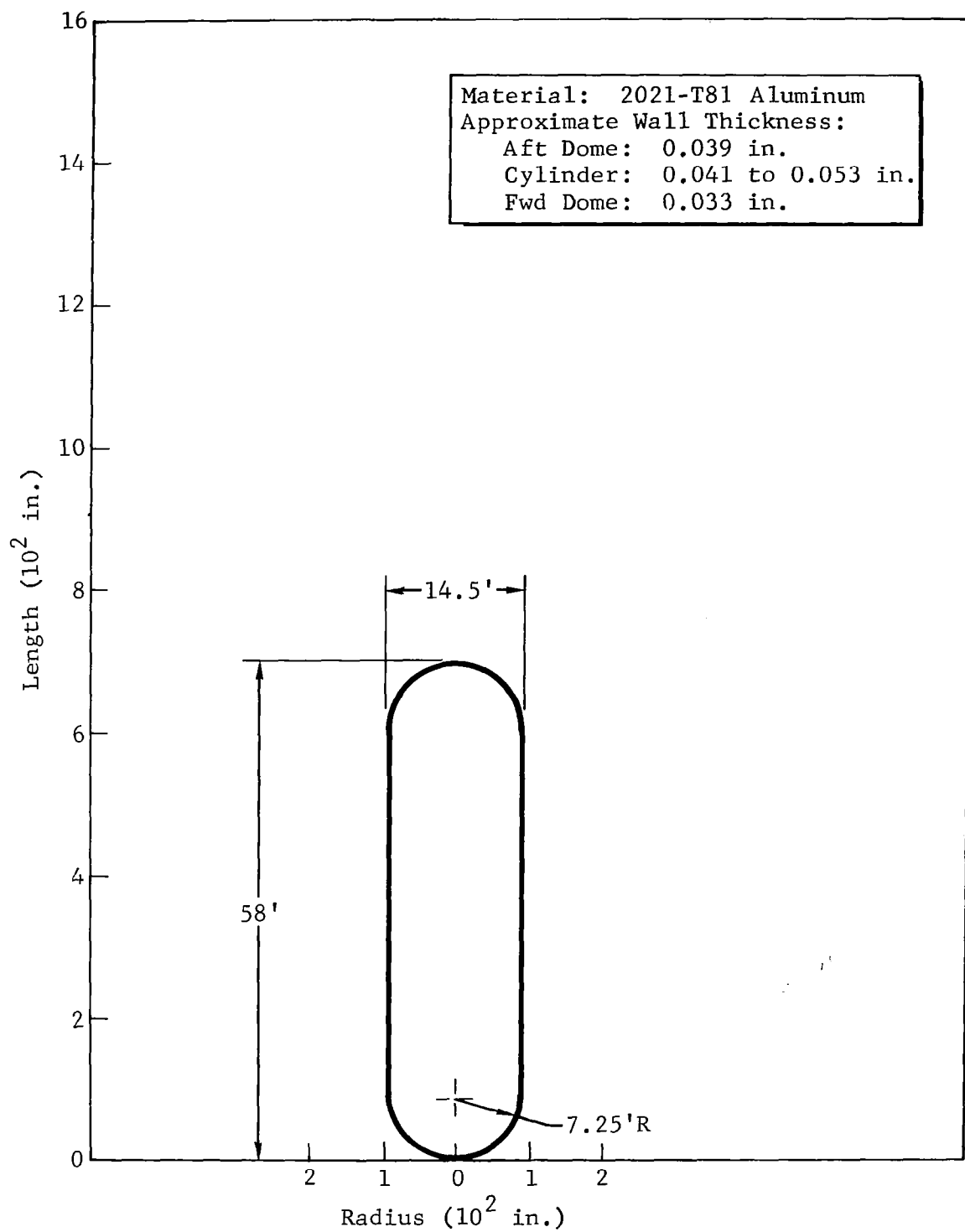
Figure 3-4   Modular Configuration Propulsion Module

3.1.2 Baseline RNS Mission

The lunar shuttle mission was chosen as the baseline mission for the RNS analysis. The mission was assumed to consist of four major burns. These are (1) trans-lunar injection (TLI) - 1800-sec burn, (2) lunar orbit injection (LOI) 390-sec burn, (3) trans-Earth injection (TEI) - 210-sec burn, and (4) Earth orbit injection (EOI) - 560-sec burn.

3.2 Analytical Methods

The analytical methods used in calculating the various RNS fluid dynamic and thermodynamic properties are described briefly below and in greater detail in Appendix B.

3.2.1 Asymmetric Propellant Heating Code

This computer code was developed by LMSC (Ref. 10) and was originally put on the FWO computer system in 1967 and was given the code designation H76. Since LMSC had made several technical improvements in 1968, the H76 code was updated to include these modifications. The most significant changes were:

1. Elimination of laminar boundary-layer consideration

2. Avoidance of large LH_2 mass build-up in top layer

3. Addition of a procedure to calculate the dwell time of draining layers

4. Alteration of output headings

5. Inclusion of boundary layer nuclear heating in boundary-layer calculations

The updated code is designated AG4.

3.2.2 Lewis Research Center Computer Code

This computer code was developed by NASA-Lewis Research
Center for the purpose of calculating temperature profiles in
a propellant tank subjected to wall and bulk (internal) heating
(Ref. 9). The code as originally written included the tank
geometry as an integral part of the program. The program has
been modified to allow either hemispherical, elliptical, or
conical tank bottom geometries to be analyzed. In addition,
the code can be used to calculate the drain temperature based
on a complete-mix model rather than a stratification model.
In the complete-mix model all energy being absorbed by the pro-
pellant is completely and instantly mixed throughout the LH_2
remaining at any time step. The ambient heating is propor-
tional to the wetted tank surface area at any time step. The
nuclear heating is also time variant since it depends upon the
propellant remaining at any time step.

3.2.3 Stratification and Destratification Analytical Methods

The stratification models used were those provided in the
computer code RIO and AG4 (Refs. 9 and 10) and those developed
under contracts NAS8-20330 and NAS8-24882 (Refs. 11 through
14). The destratification models used were those developed
under the above mentioned contracts (Refs. 11 through 15).
Because the references contain detailed descriptions of the

3-8

analytical models and methods no details will be provided here.
Details of the models will, however, be discussed as necessary
in those sections where they were used to calculate the thermo-
dynamic state of the propellant.

3.3 Analytical Studies

The objective of the analytical studies performed on the
various RNS configurations was to provide the parametric data
and operational insight required to design and synthesize an
extended-parameter, propellant heating experiment. In per-
forming these studies the effects of various RNS stage operating
parameters such as pressurization level, acceleration, and
drain rate on the fluid dynamic and thermodynamic state of the
liquid hydrogen propellant were investigated for the four baseline
RNS configurations and mission segments described in Section 3.1.
Also investigated were the effects of the operational character-
istics of the computer codes on calculated answers, the fluid
dynamic and thermodynamic effects of auxiliary internal tank
structure located near the tank bottom, and the radiation-induced
conversion of parahydrogen to orthohydrogen (para-ortho shift)
in the propellant tank.

In addition to the studies conducted on the four baseline
RNS configurations, a cursory analysis of the "Dual-Cell" RNS
concept was also performed at the request of the contractor.

The results of this study are presented separately in Appendix C.

All RNS concepts and conditions analyzed are summarized in Table 3-1. The results of the analyses conducted on the four baseline concepts are discussed below and where applicable compared to the previously calculated 5000-MW NERVA single tank nuclear flight module (NFM) data (Ref. 1).

3.3.1 Heating Rates

To determine the thermodynamic state of the propellant it is necessary to know the amount of energy transferred to the liquid hydrogen and ullage from (1) nuclear energy directly deposited in the propellant and tank wall (nuclear heating) and (2) conduction through the tank insulation and influx of warm pressurant gas (ambient heating). The heating rates due to these sources are discussed in the following subsections.

3.3.1.1 Nuclear Heating

The details of the method of calculation of nuclear energy deposited in liquid hydrogen and the tank wall as well as the resulting heating rates are described in Section II. The data presented show that the bulk heating varies from a low of 0.73 Btu/sec (0.77 kW) to a high of 10 Btu/sec (10.6 kW). The wall heating varies from a low of 0.093 Btu/sec (0.098 kW) to a high of 0.228 Btu/sec (0.240 kW). In both cases the 8° conical

Table 3-1

RNS CONDITIONS ANALYZED

TANK CONFIGURATION AND ENGINE TYPE	MISSION SEGMENT & RUN NO.	BURN TIME (sec)	DRAIN RATE (lb/sec)	AMBIENT WALL HEATING (Btu/ft²-sec x 10⁵)	ULLAGE PRESS. VENT - RUN (psia)	COMPUTER CODE USED	COMP. TIME INCREMENT (sec)	ACCELERATION LEVEL (g)	INITIAL PROP. LEVEL (ft)
Single Tank - 8.5° Conical Bottom, Full Flow Engine 1575 MW	1 TLI	900	91.6	1.8	24 - 30	AG4	30	0.15	145
	2 TLI	1800	↑	↑	↑	↑	60	↑	145
	3 LOI	390					30		98
	4 TEI	210					30		85
	5 EOI	560					30		77
Single Tank - 8° Conical Bottom, Full Flow Engine 1575 MW	6 TLI	1800					60		149
	7 LOI	390					30		102
	8 TEI	210	↓				↑		88
	9 EOI	750	91.6				↓		80
	10 EOI	1150	59.5		24 - 30				80
	11 EOI	1150	59.5		24 - 27.5		30	0.15	80
Single Tank - 15° Conical Bottom, Full Flow Engine 1575 MW	12 TLI	1800	91.6		24 - 30		60	1.0	102
	13 LOI	390	↑		↑		30	↑	55
	14 TEI	210					30	↓	44
	15 EOI	560					30	1.0	38
	16	750	↓				60	0.15	↑
	17	750	91.6				30	↑	
	18	1115	59.5		24 - 30		↑		
	19 EOI	1115	59.5		24 - 27.5				38
Modular - Propulsion Module, Full Flow Engine 1575 MW	20 N/A	405	91.6		18 - 24.9				54
	21 ↑	615	59.5		18 - 24.9				↑
	22	615	59.5		24 - 24.9				↓
	23	330	91.6		24 - 24.9				54
Hybrid - Propulsion Tank, Full Flow Engine 1575 MW	24	106	91.6		24 - 26.2				19
	25	160	59.5		24 - 26.2				↑
	26	160	59.5		24 - 30				
	27	106	91.6		24 - 30		30		
	28	106	91.6		24 - 26.2		10		
	29	160	59.5		24 - 26.2		↑		
	30	160	59.5		24 - 30		10		
	31	106	91.6		24 - 30	AG4	10	N/A	
	32	106	91.6		24 - 26.2	* RIO	N/A	↑	
	33	106	91.6		↑	**			
	34	160	59.5		↓	*			
	35	160	59.5		24 - 26.2	**			
	36	106	91.6		24 - 30	*			
	37	106	91.6		↑	**			
	38 ↓	160	59.5			*			
	39 N/A	160	59.5	1.8		** RIO			19
Dual Cell Elliptical Hot Bleed Engine 1500 MW	40 TLI	1716	90	2.2		N/A			N/A
	41 LOI	381	↑	↑		↑			↑
	42 TEI	221	↓	↓		↓			
	43 EOI	567	90	2.2	24 - 30	N/A	N/A	0.15	N/A

* RIO - Stratified Model
** RIO - Complete Mix Model

bottom single tank has the lowest heating while the propulsion module of the modular configuration is the highest. Pertinent characteristics of the nuclear heating profiles are given in Table 3-2.

Comparisons of the nuclear energy deposition rates of the current 1575-MW NERVA RNS configurations with those of the previous 5000-MW NERVA NFM were made and are shown in Figures 3-5 and 3-6 (bulk and wall deposition, respectively). The data marked NFM are based on a 5000-MW NERVA engine with a 300,000 lb-LH$_2$ capacity elliptical bottom tank.

3.3.1.2 Ambient Heating

A value for the sidewall heat leak was determined by considering the various high performance insulation (HPI) systems and vehicle surface optical properties presented in References 3 through 4. The HPI systems considered were SUPERFLOC, GAC-9, NARSAM, and DAM-NM with thicknesses ranging from 0.5 to 3 inches. Mission-duration (time) averaged temperatures considered ranged from 300°R to 450°R. Based on these considerations the sidewall heating rate value selected for the study was 1.8×10^{-5} Btu/ft^2-sec. In addition, it was assumed that any penetration heat leaks would be of the same order as the sidewall heating, i.e., thermal protection system failure modes were not considered.

TABLE 3-2

RNS NUCLEAR ENERGY DEPOSITION RATE CHARACTERISTICS

	SINGLE TANK		HYBRID	MODULAR
	8° Conical	15° Conical	PROP. MODULE	PROP. MODULE
Tank Height (ft)	152.25	105.5	21.12	58
Total Energy Deposition Rate (kW)				
Bulk	0.775	10.0	6.23	10.6
Wall	0.098	0.208	0.137	0.240
Height and Height Fraction (H/H_o) at Given % of Total Energy Deposition Rate				
Bulk: 60% H	7.5	5	3.1	4.6
H/H_o	0.049	0.0474	0.147	0.0793
90% H	21	15	9.3	9.5
H/H_o	0.138	0.142	0.44	0.164
Wall: 60% H	6.1	5.8	4.8	4.7
H/H_o	0.040	0.055	0.227	0.081
90% H	17.5	15.5	9.8	9.75
H/H_o	0.115	0.147	0.464	0.168
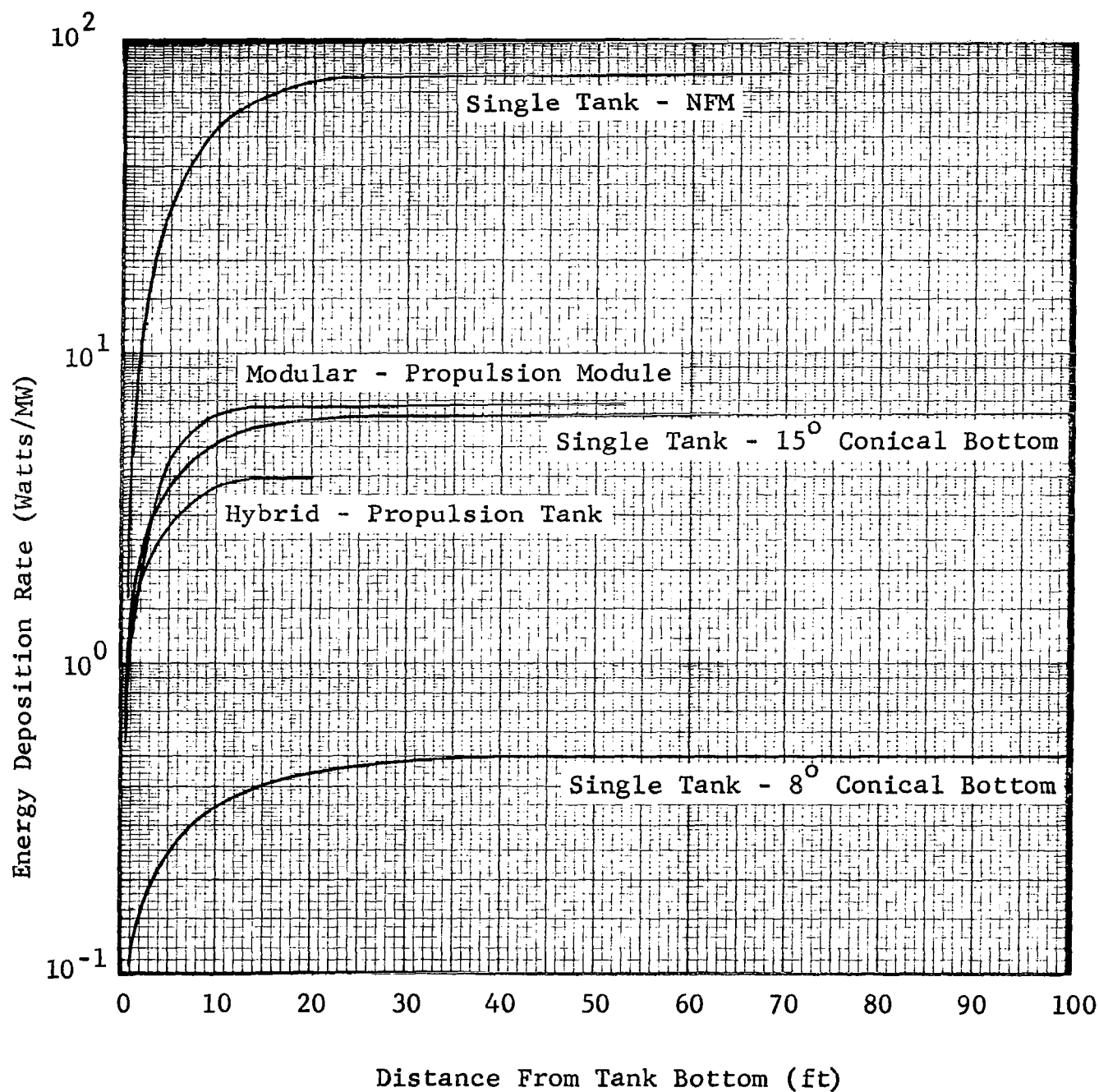
Figure 3-5 Bulk Nuclear Energy Deposition Rate For Various Tank Configurations
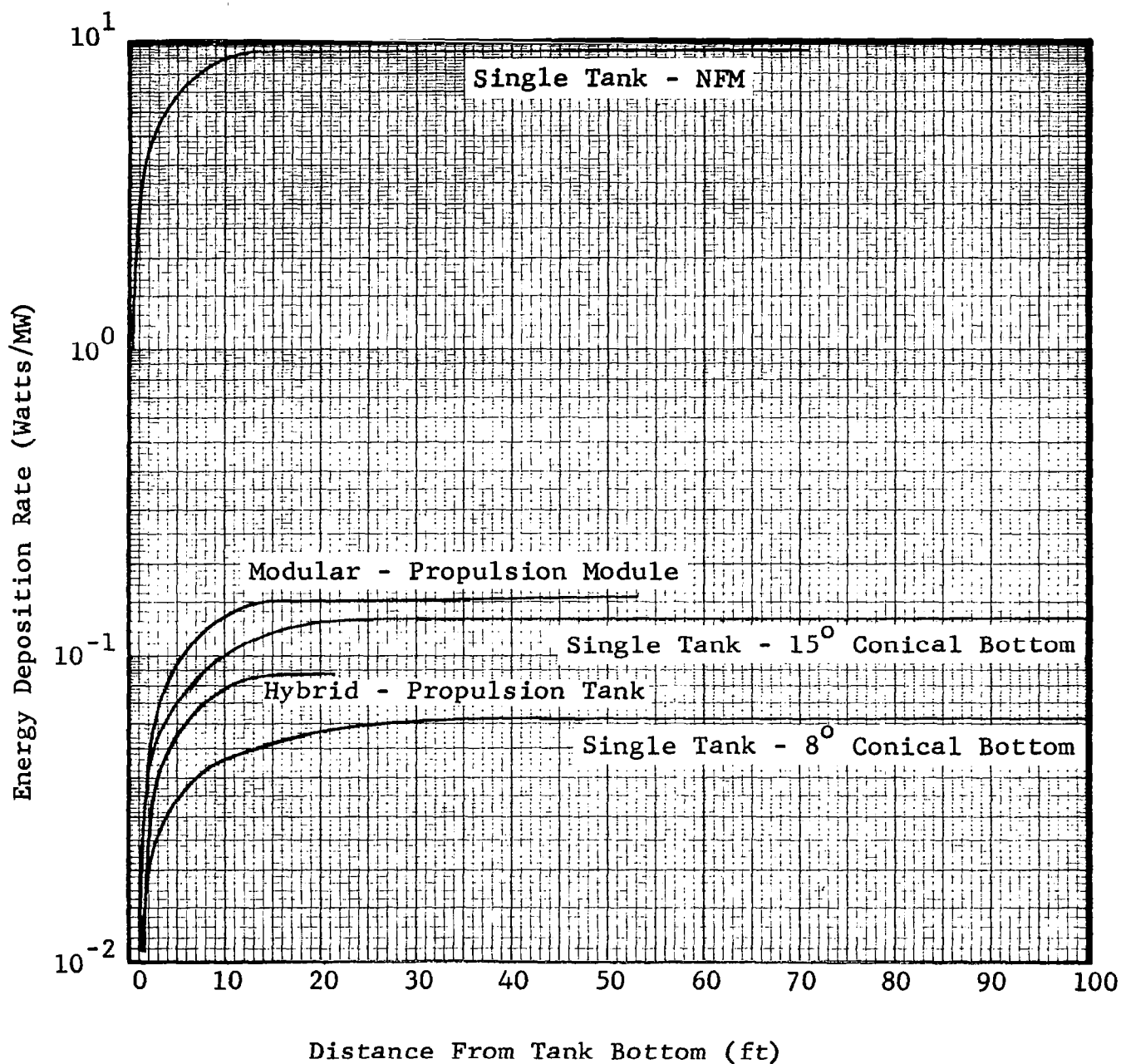
Figure 3-6   Wall Nuclear Energy Deposition Rate
             For Various Tank Configurations

3.3.2 Drain Temperatures

In order to have a consistent base from which to evaluate the drain-temperature profiles of the various configurations the following assumptions were made:

1. Propellant settled at start of burn

2. Propellant and ullage in thermal equilibrium at vent pressure at start of burn

3. Drain rate reached instantaneously at start of burn

4. Pressurant gas (GH_2) at a constant temperature of $230^{\circ}R$

5. Acceleration reached instantaneously at start of burn and constant

6. Wall and bulk nuclear heating instantaneous at start of burn.

The most important of the above assumptions is number 2. This assumption minimizes the drain temperature rise since no stratification is assumed to exist prior to tank drain (engine firing). This is, however, a plausible mode of operation since all RNS configurations can be vented and propellant mixed prior to engine operation.

Drain temperatures were calculated for a wide range of RNS operating conditions; the most significant of which are shown in Table 3-1. The individual effect of these operating conditions on drain temperature are discussed briefly in the paragraphs below and are discussed in detail in Subsections 3.3.4 through 3.3.9.

3.3.2.1   Single Tank Configuration - 8° Conical Bottom

The drain-temperature profiles for the 4 segments of the baseline lunar mission are shown in Figure 3-7 (Runs 6 through 9, Table 3-1). The vent and run pressures were 24 and 30 psia, respectively, and the initial propellant temperature was 39.75°R. The maximum temperature rise was 0.09°R and occurred during the TLI burn. The temperature rise for the LOI, TEI, and EOI were 0.05, 0.05, and 0.06°R, respectively.

Two runs were made using a turbopump malfunction flow rate of 59.5 lb/sec (corresponds to single turbopump operation) and vent/run pressures of 24/30 and 24/27.5 psia (Runs 10 and 11). The drain temperatures for these conditions were within 0.02°R of one another and at 870 seconds had drain temperatures of 39.81°R and 39.79°R, respectively.

Prior to selection of the 8° conical bottom single tank configuration, drain temperatures had been calculated for the 8.5° conical bottom (Runs 1 through 5). The drain temperatures were, for all practical purposes, identical to those predicted for the 8° conical bottom. The largest variation was less than 0.01°R. The drain temperatures are shown in Figure 3-8.

3.3.2.2   Single Tank Configuration - 15° Conical Bottom

Conditions analyzed for this configuration included various accelerations, pressure levels, and flow rates (Runs 12 through
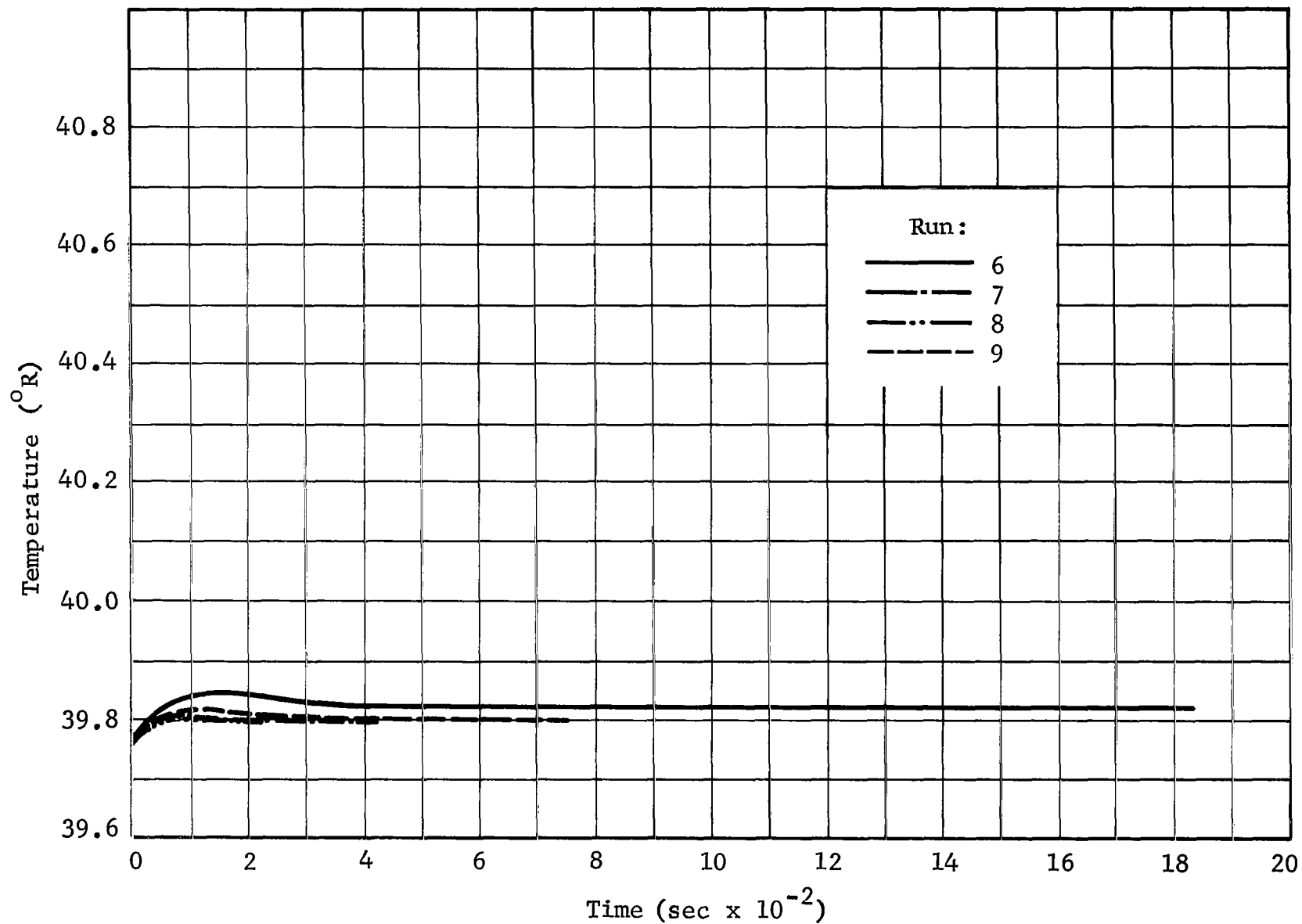
Figure 3-7 Drain-Temperature Profiles for Lunar Shuttle Mission –
Single Tank 8° Conical Bottom Configuration
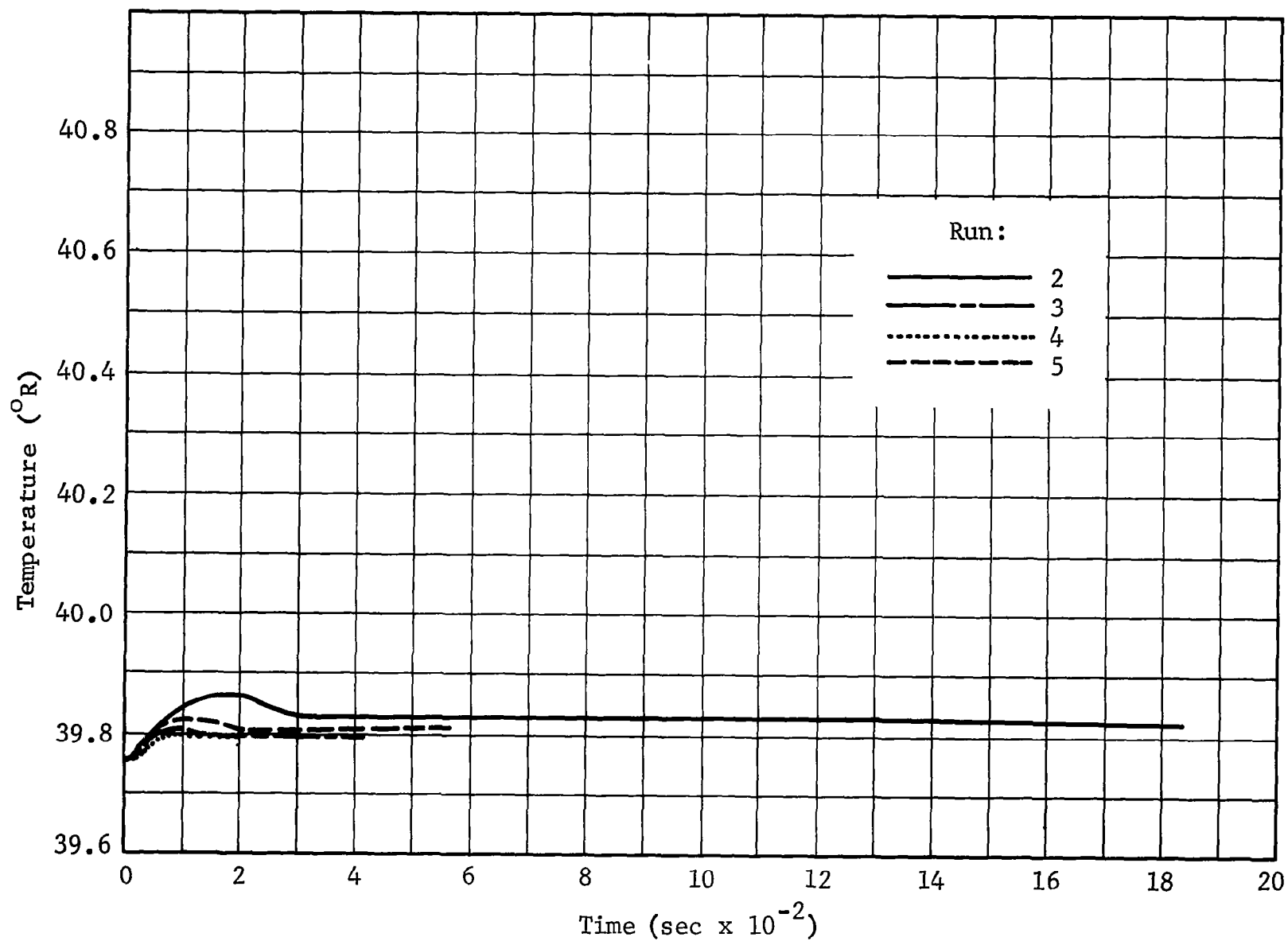
Figure 3-8 Drain-Temperature Profiles for Lunar Shuttle Mission –
Single Tank 8.5° Conical Bottom Configuration

19). Runs 17, 18, and 19 are applicable to the baseline lunar mission and the results will be discussed here. The results of the other runs are discussed in the applicable parameter effects subsections.

The temperature rise for the EOI mission segment with normal operating conditions of 91.6-lb/sec drain rate and 24/30 psia vent/run pressure was $0.11^{O}R$ to $39.86^{O}R$ at 560 seconds. Runs made with the malfunction mode 59.5-lb/sec drain rate for vent/run pressures of 24/30 and 24/27.5 psia predicted drain temperatures of 39.82 and $39.83^{O}R$, respectively, at 870 seconds. The drain-temperature data for runs 17, 18, and 19 are shown in Figure 3-9. The drain-temperature data are shown through times corresponding to 1000-lb LH_2 or less residual in the tank. The drain temperatures corresponding to the baseline mission are obtained by simply reading the temperature at the appropriate burn time.

3.3.2.3 Modular Configuration

Drain temperatures for the modular RNS configuration were determined for pseudo EOI conditions or malfunction mode stage operations. That is, it was assumed that, for whatever the reason, only the propulsion tank was operable and no flow from any of the propellant tanks into the propulsion tank could take place. The initial amount of propellant in the propulsion tank was set at 36,900-
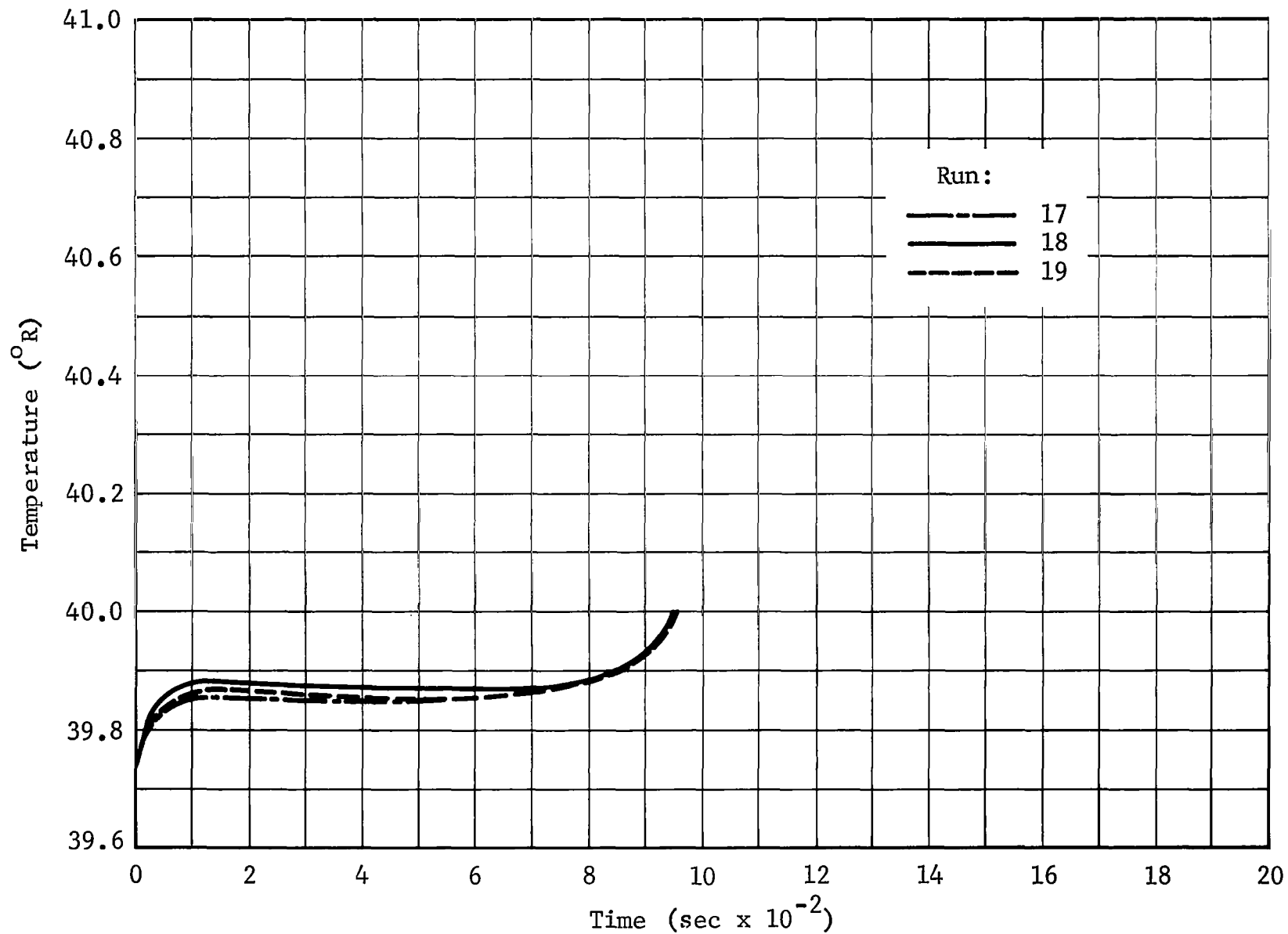
Figure 3-9   Drain-Temperature Profiles for EOI Mission Segment —
Single Tank 15° Conical Bottom Configuration

lb LH$_2$ which corresponds to an ullage fraction of 5 percent.
These assumptions were necessary in order to eliminate the need
to calculate the thermodynamic state of the LH$_2$ flowing into
the propulsion tank from the various propellant tanks, a task
beyond the scope of this study.

Four sets of operating conditions were analyzed (Runs 20
through 23). The data for these runs are presented in plotted
form in Figure 3-10. The maximum drain temperature possible
is 39.99^{o}R which corresponds to the 24.9 psia run pressure. As
can be seen in Figure 3-10, this temperature is not achieved
until very near the end of the drain period which is about 620
seconds for the 59.5-lb/sec (turbopump malfunction mode) drain
rate and 403 seconds for the 91.6-lb/sec drain rate.

3.3.2.4 Hybrid Configuration

As in the case of the modular RNS configuration only the
propulsion (run) tank of the hybrid RNS configuration was
analyzed. Both computer code AG4 and RIO were used to calculate
the drain-temperature profiles under various RNS operating con-
ditions (Runs 24 through 39). In all cases the initial amount
of propellant was set at 9,700-lb LH$_2$ which corresponds to a
5 percent ullage and a liquid surface height of 19 ft.

The maximum drain temperature possible was 41.36^{o}R for
the run pressure of 30 psia and 40.36^{o}R for the run pressure

3-22
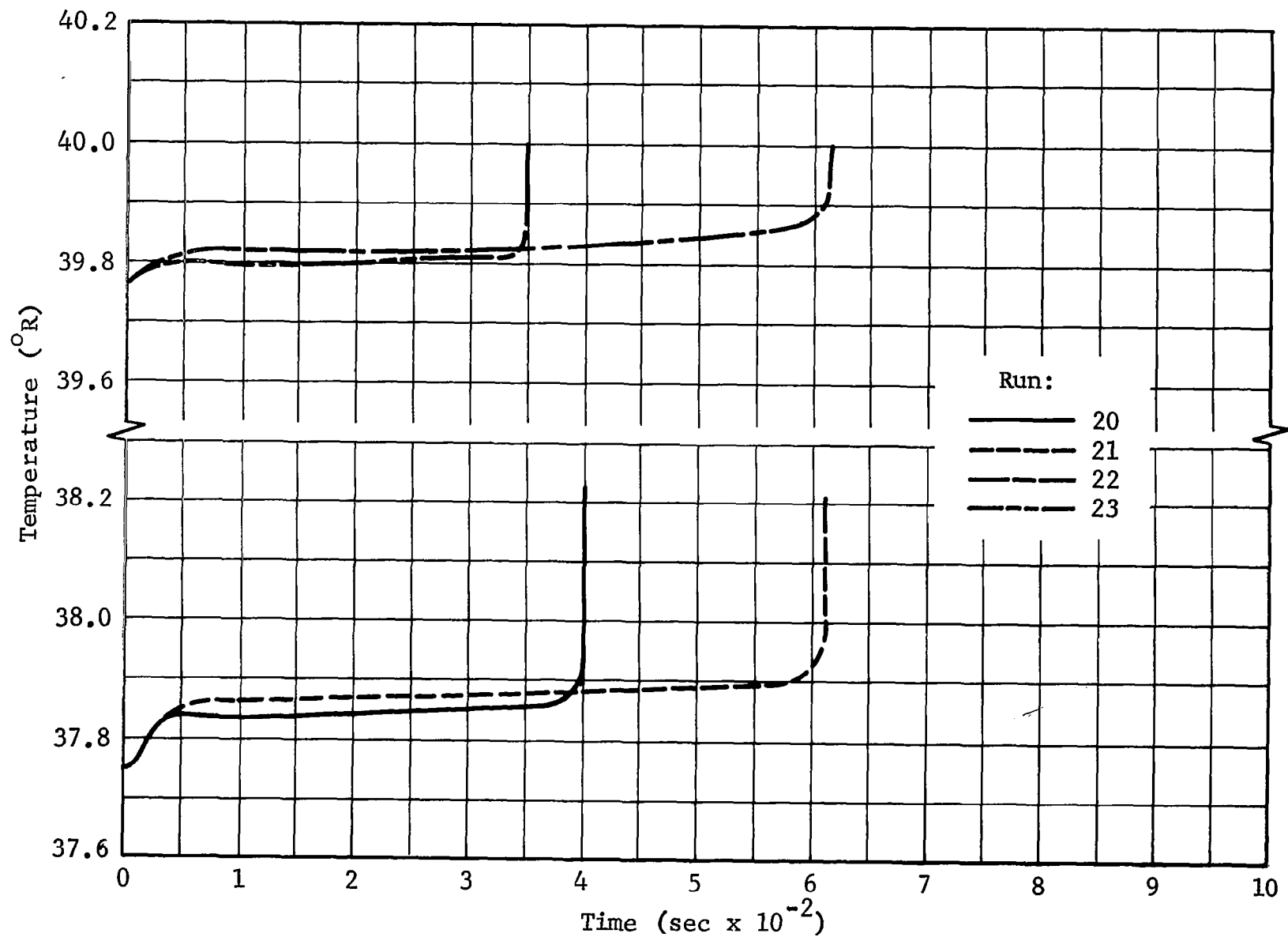
Figure 3-10   Drain-Temperature Profiles for Propulsion
Module — Modular Configuration

of 26.2 psia. The drain temperatures calculated using AG4 with a 10-second compute increment (Runs 28 through 31) are shown in Figure 3-11. The 10-second compute increment data are considered to be better predictions than those calculated with a 30-second compute increment (see Subsection 3.3.4 for further details).

Drain temperatures under identical RNS operating conditions were also calculated using both the complete-mix and stratified models of code RIO (Runs 33 through 39). The temperatures predicted using the complete-mix model were lower by about 0.02°R than those predicted using the stratified model. This indicates that for the operating conditions analyzed very little stratification occurred. The drain temperatures are shown in Figures 3-12 through 3-15.

3.3.3 Pressurization Requirements

The pressurization gas mass requirements were calculated for the conditions listed in Table 3-1 using computer code AG4 (Runs 1 through 31). The pressurant gas (GH), supplied by an autogenous pressurization system, was assumed to have an enthalpy of 780 Btu/lb. Because of the possible differences in engine chamber pressure, pump spin rate, and turbine exhaust supply during the start-up phase of the different RNS configurations, the pressurant gas enthalpy was treated as a constant
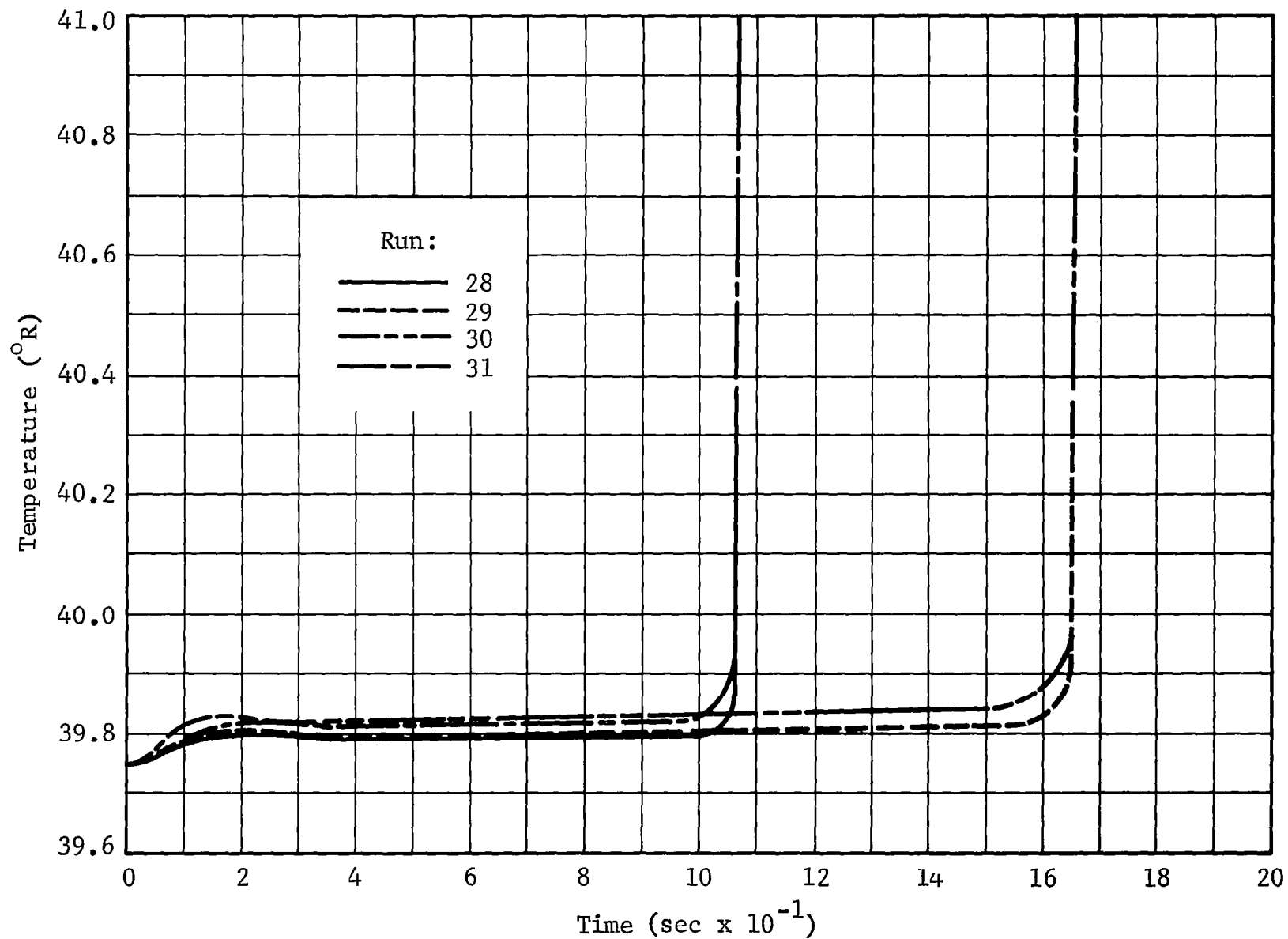
Figure 3-11   Drain-Temperature Profiles for Propulsion Tank —
Hybrid Configuration; Code AG4 Data
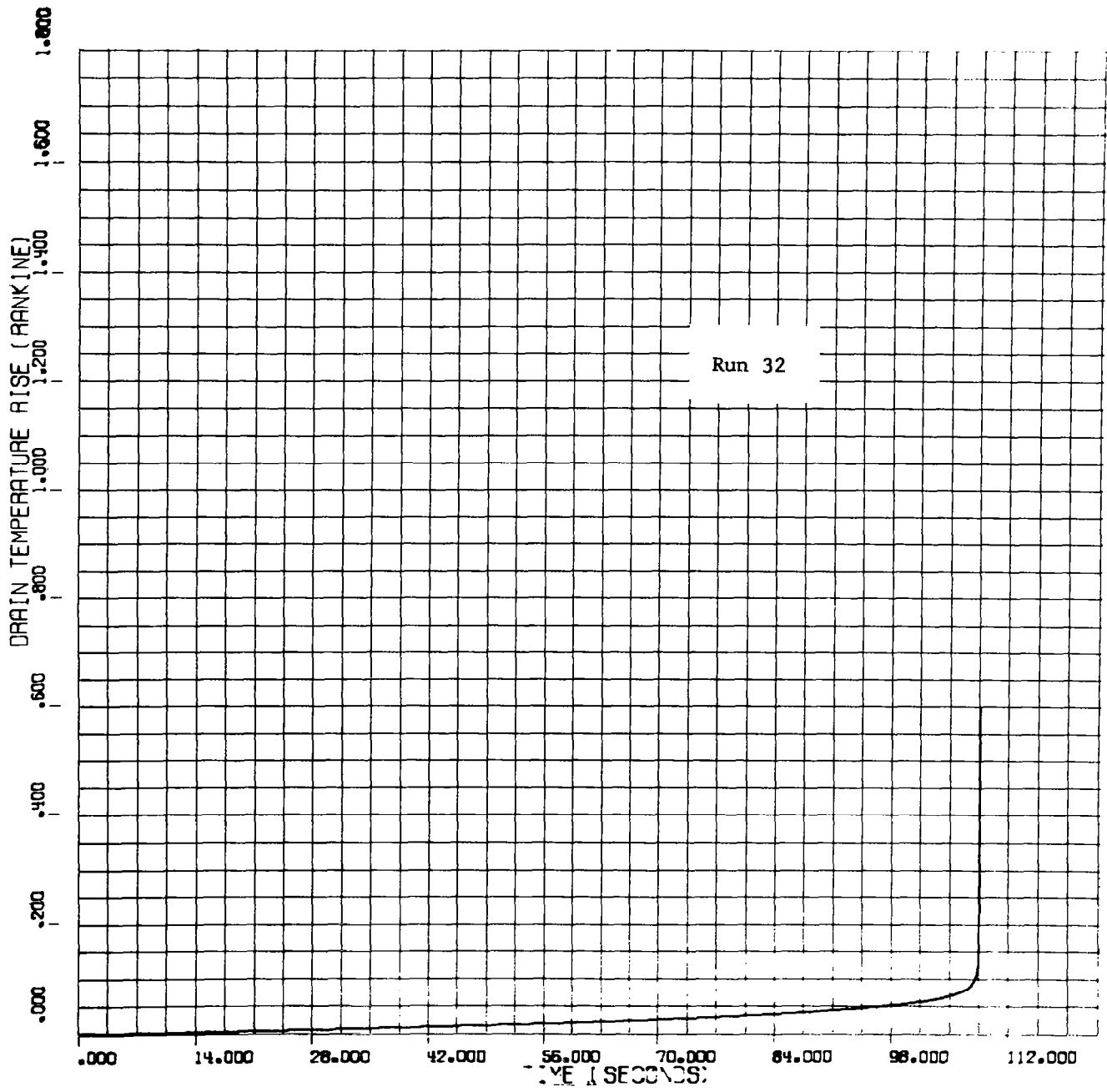
Figure 3-12   Drain-Temperature Profiles For Propulsion Tank
Hybrid Configuration Code RIO, Run 32
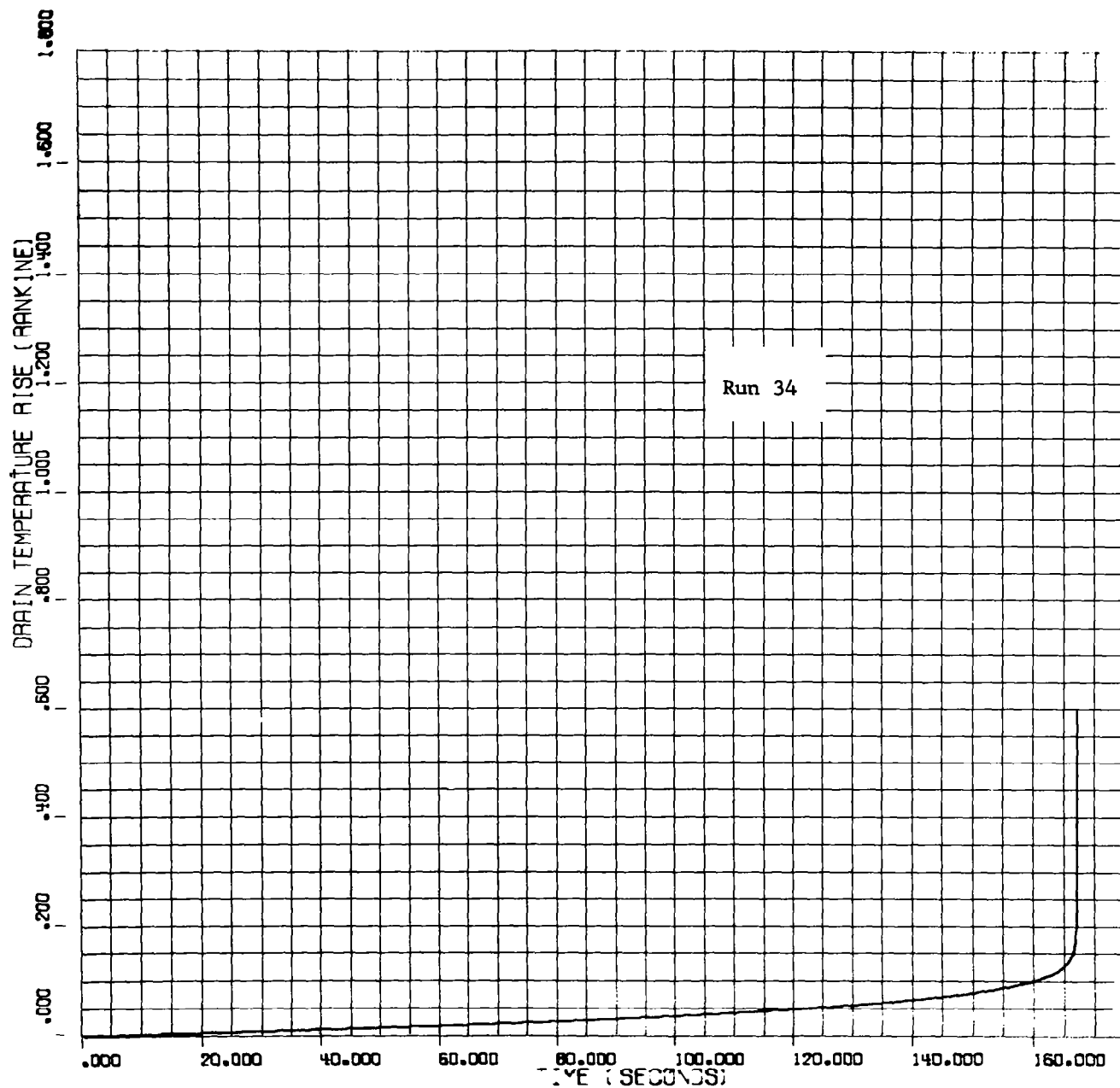
Figure 3-13   Drain-Temperature Profiles For Propulsion Tank
Hybrid Configuration; Code RIO, Run 34

3-27
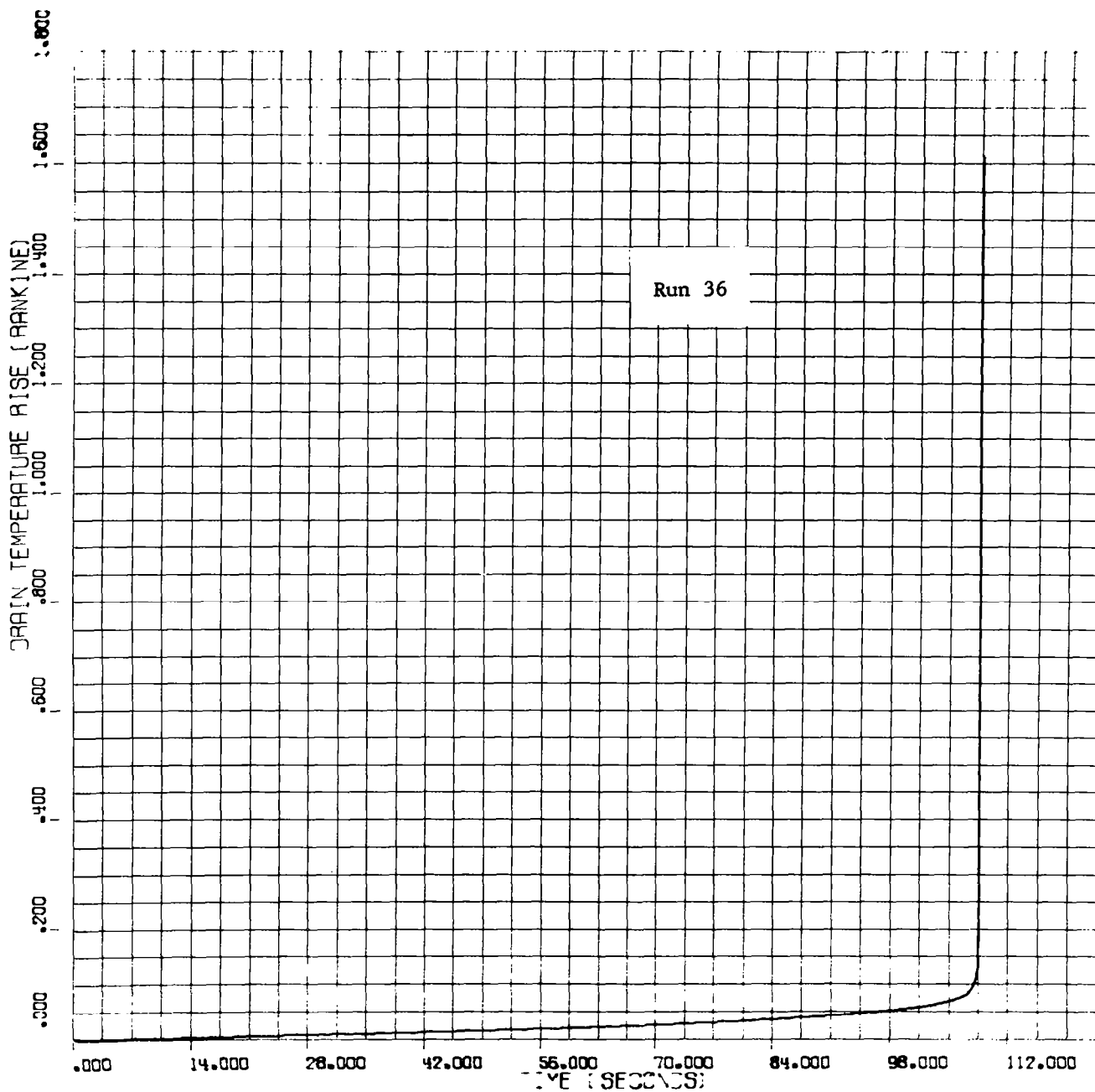
Figure 3-14   Drain-Temperature Profiles For Propulsion Tank
Hybrid Configuration; Code RIO, Run 36
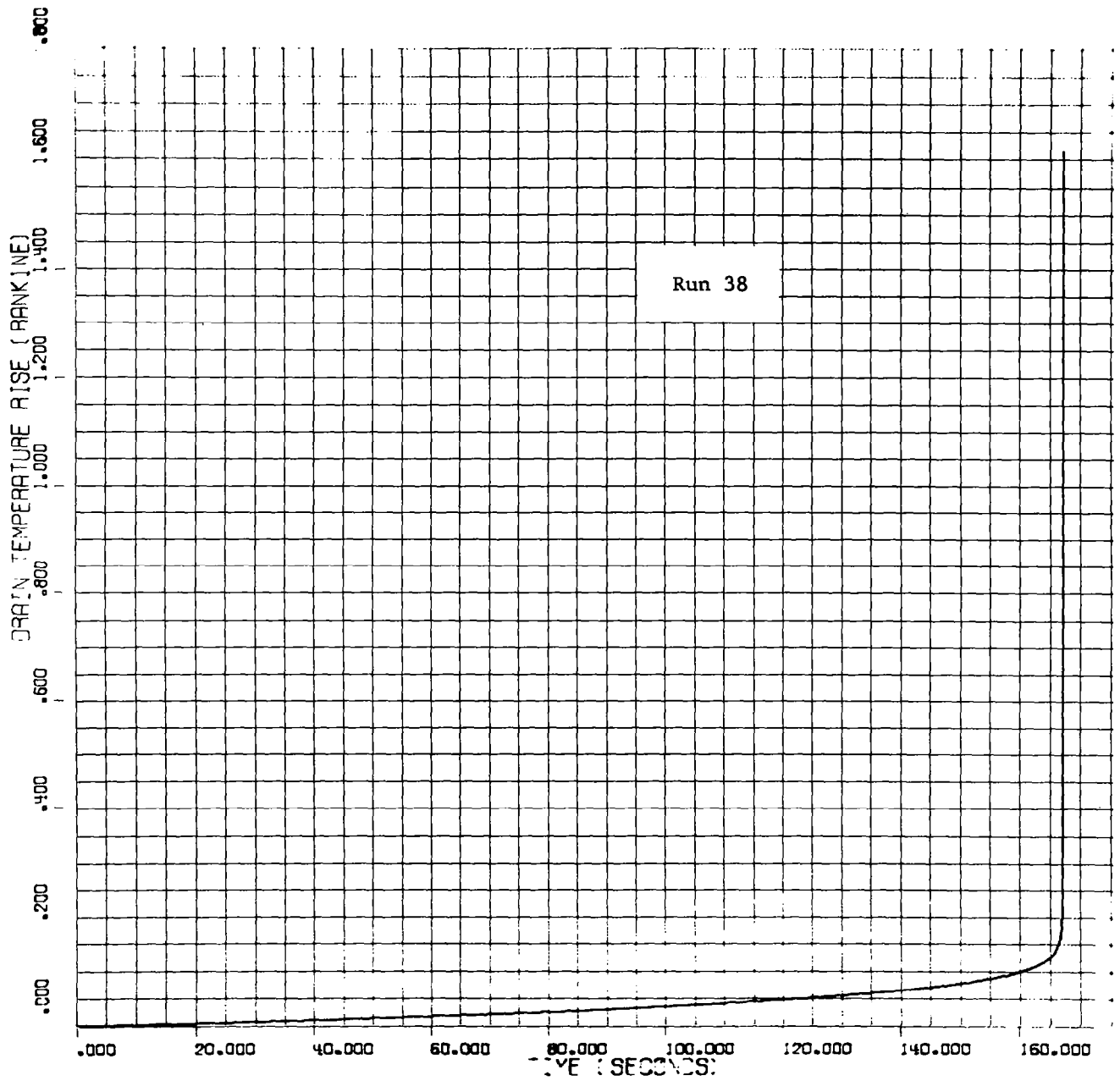
Figure 3-15   Drain-Temperature Profiles For Propulsion Tank
Hybrid Configuration; Code RIO, Run 38

in all the cases analyzed. All other stage operational charac-
teristics were the same as those listed in Subsection 3.3.2.

3.3.3.1 Single Tank Configuration - 8° Conical Bottom

Pressurant gas requirements for the TLI, LOI, TEI, and
EOI segments of the lunar shuttle mission were predicted to be
3008, 1132, 973, and 1620 lb, respectively, or a total of 6733
lb. The cumulative pressurant mass versus time for the four
mission segments are shown in Figure 3-16.

Prior to selection of the 8° conical bottom configuration,
pressurant requirements had been calculated for a 8.5^o conical
bottom (Runs 1 through 5). The mass requirements for this con-
figuration were very close to those predicted for the 8° coni-
cal bottom. The largest variation was 36 lb and occurred
during the EOI burn. The predicted pressurant mass require-
ments for the TLI, LOI, TEI, and EOI burns are 3010, 1127, 969,
and 1656 lb, respectively. The total mass was 6762 lb compared
to 6733 lb for the 8° conical bottom. The pressurant mass
versus time for the four mission segments are shown in Figure
3-17.

3.3.3.2 Single Tank Configuration - 15° Conical Bottom

The pressurization requirements for the four segments of
the lunar shuttle mission (Runs 12 through 15) are shown in
Figure 3-18. The results shown here are for a 1-g acceleration

3-30
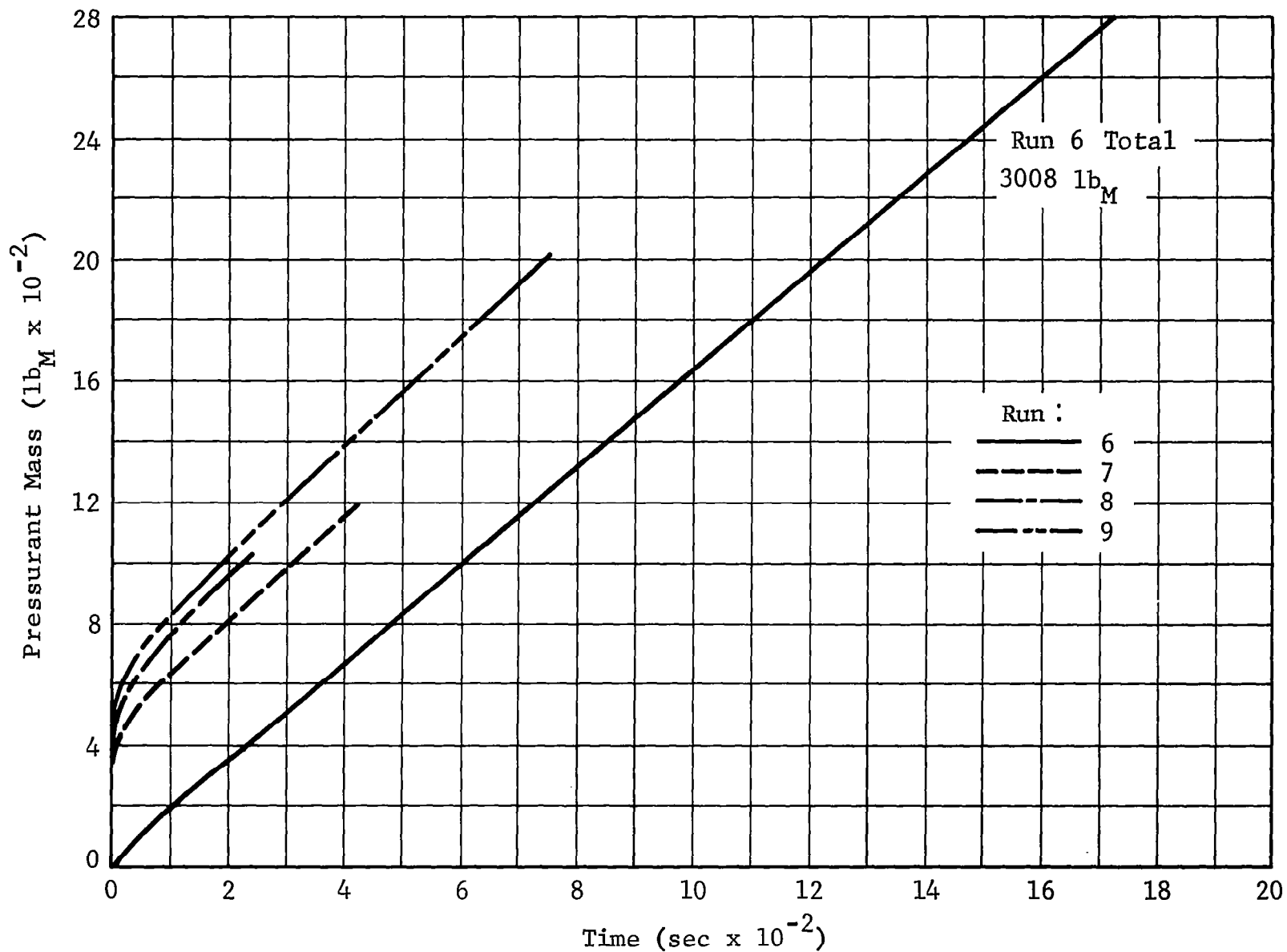
Figure 3-16 Pressurant Requirements for Lunar Shuttle Mission – Single Tank 8° Conical Bottom Configuration
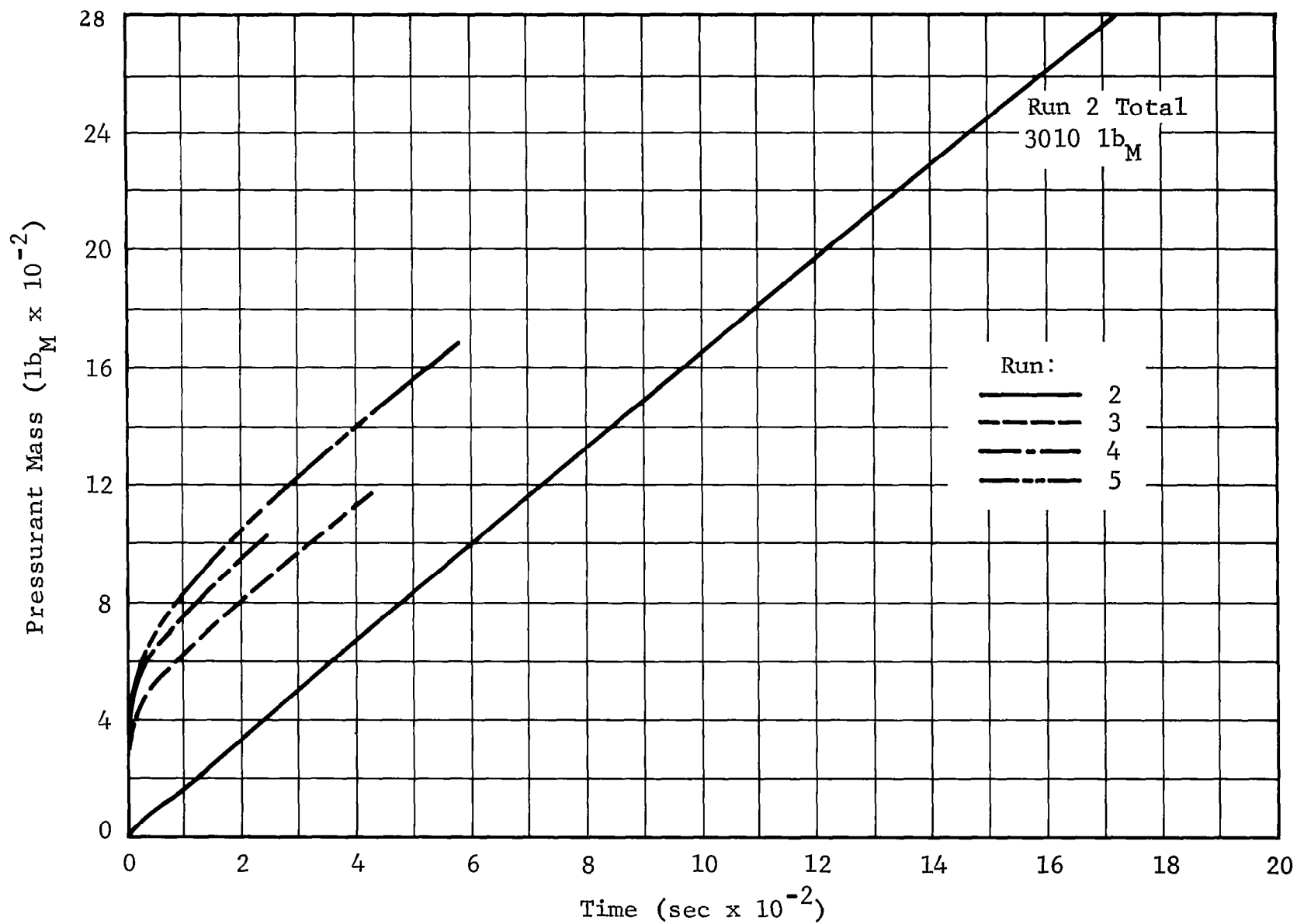
Figure 3-17 Pressurant Requirements for Lunar Shuttle Mission —
Single Tank 8.5° Conical Bottom Configuration
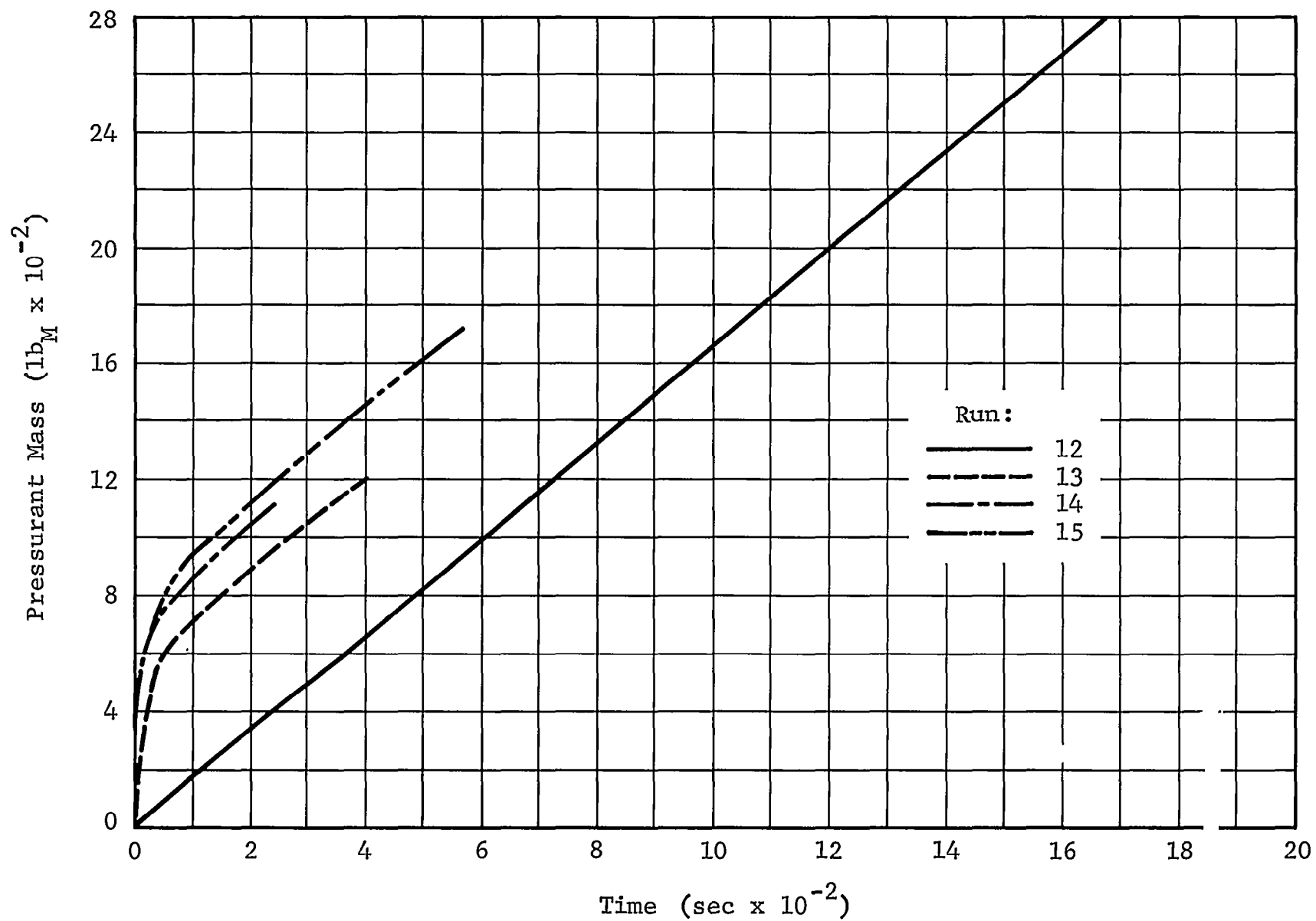
Figure 3-18   Pressurant Requirements for Lunar Shuttle Mission —
Single Tank 15° Conical Bottom Configuration

level. The cumulative mass for the TLI, LOI, TEI, and EOI segments were 3000, 1180, 1060, and 1700 lb, respectively, or a total of 6930 lb. This total mass compares very well with that predicted for the 8° single tank configuration: 6733 lb vs 6930 lb, or less than a 3 percent difference.

Comparison of the EOI segment data run at a 0.15-g acceleration level (Run 17) indicate that the total mass requirements were 1698 lb. This is almost identical to the 1700-lb requirement for the 1-g case. The maximum flow rate was, however, higher for the 1-g case. Acceleration effects are discussed in Subsection 3.3.5.

3.3.3.3 Modular Configuration

Pressurization requirements were determined for conditions wherein only the propulsion tank was operable and no flow from any of the propellant tanks could take place. In all cases analyzed the initial LH_2 mass was set at 36,900 lb which corresponds to an ullage volume fraction of 5 percent. These assumptions were used in order to avoid analyzing the large number of variations on the draining sequence of the various propellant tanks, a task beyond the scope of this study.

The results of the four sets of conditions analyzed are shown in Figure 3-19. The data show that the level of pressurization as well as drain rate have very little effect upon
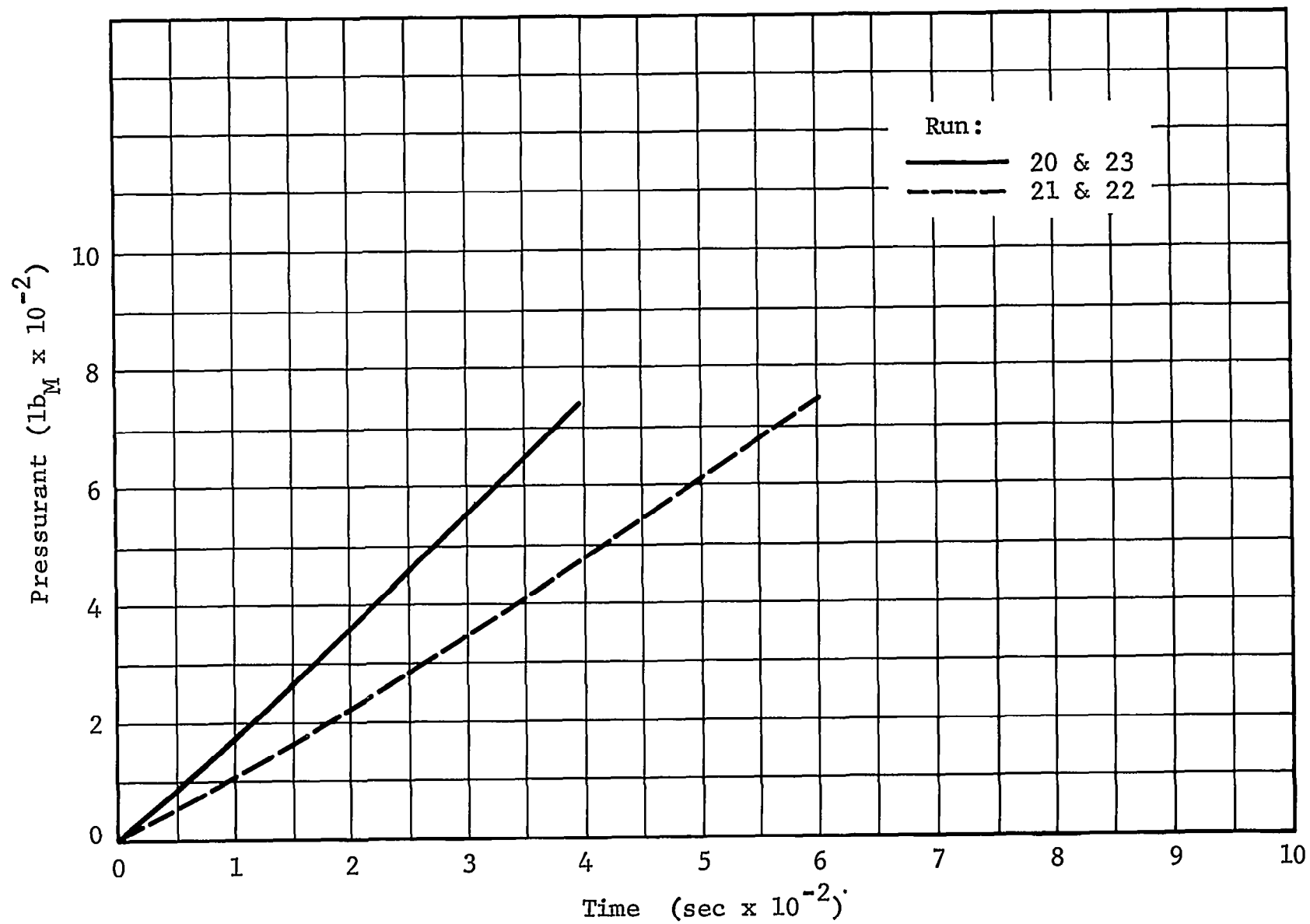
Figure 3-19 Pressurant Requirements for Propulsion Tank —
           Modular Configuration

the total amount of pressurant required, about 740 lb. The
rate of flow is, of course, dependent upon the drain rate.
This effect can be seen by comparing the slope of the curves
shown in Figure 3-19.

3.3.3.4 Hybrid Configuration

The pressurant requirements for the propulsion (run) tank
of the hybrid RNS configuration were determined for the normal
91.6-lb/sec and malfunction 59.5-lb/sec drain rates under two
different vent/run pressure levels (24/26.2 and 24/30 psia)
using code AG4 with a 30-second and 10-second compute-time
increment (Runs 23 through 31). The requirements calculated
using a 10-second compute increment are shown in Figure 3-20.
The 10-second compute increment data are considered to be the
better predictions (see Subsection 3.3.4 for details).

The tank was assumed to contain 9,700 lb of LH_2 with an
ullage volume of 5 percent at the start of drain. As can be
seen in Figure 3-20, the total amount of pressurant required
was about 190 lb for all cases. The flow rate averaged about
1.72 lb/sec for a drain rate of 91.6 lb/sec and 1.12 lb/sec for
the 59.5-lb/sec drain rate.

3.3.4 Compute-Time Increment Effects

Several different compute-time increments were used in
using code AG4 to calculate drain temperatures and pressurant
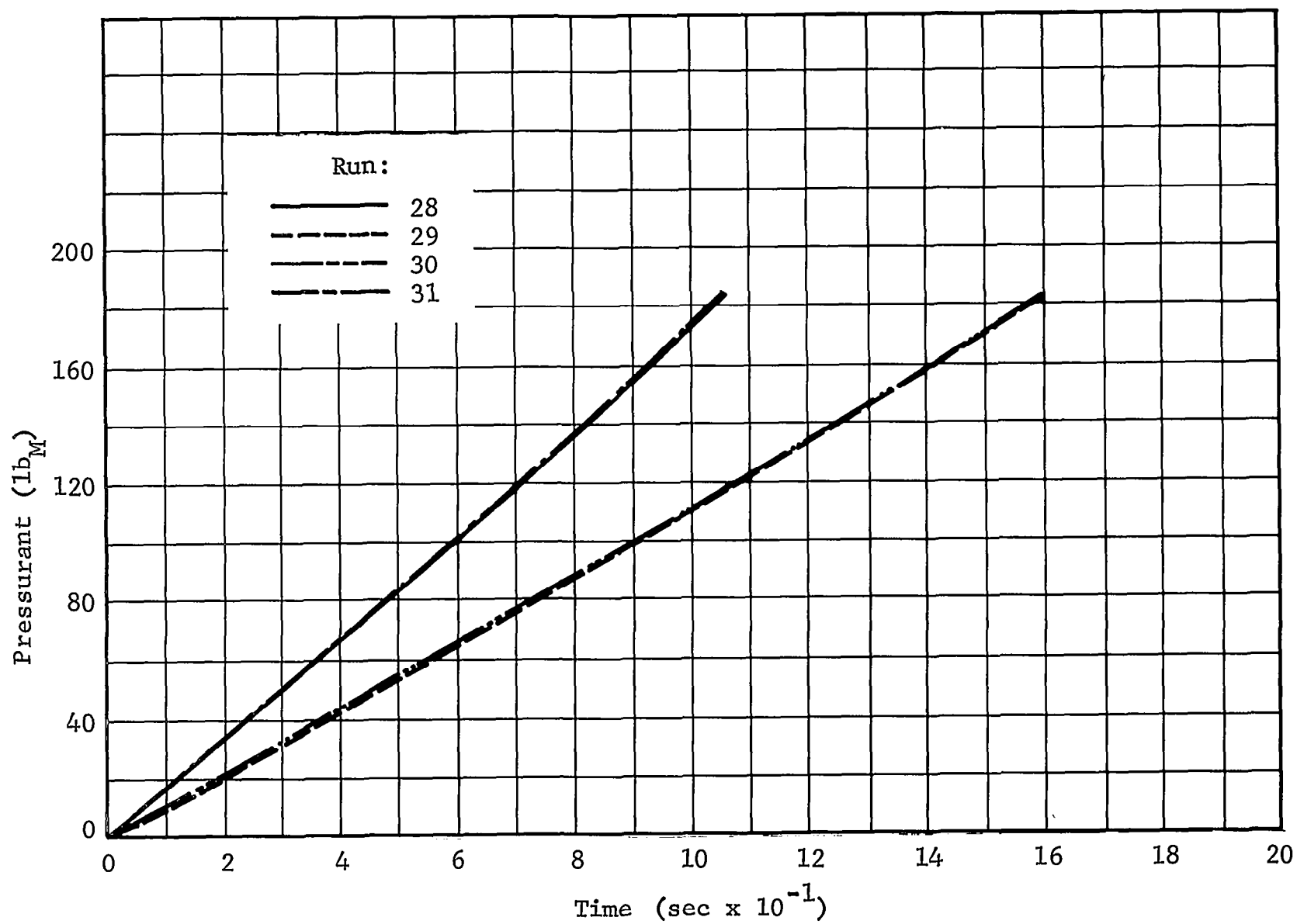
Figure 3-20   Pressurant Requirements for Propulsion Tank —
Hybrid Configuration

requirements. While the use of small time increments tends to increase the accuracy of the calculated numbers, the amount of computer time required per problem becomes too large to be economical for parametric or trade studies. For example, increasing the time increment from 30 seconds to 60 seconds reduced the computer run-time about 60 percent. The effect of compute-time increment on the calculated drain temperatures and pressurant requirements are discussed below.

3.3.4.1 Drain Temperature

Six sets of runs were made in which all variables were identical except for the compute-time increment (Runs 1 & 2; 16 & 17; 24 & 28; 25 & 29; 26 & 30; 27 & 31). Analysis of the drain temperatures calculated showed that in all cases the larger compute-time increment results were 0.02° to $0.05^{\circ}R$ higher than for the smaller increment. In addition, the drain temperature response to compression heating was faster when smaller time increments were used. A typical set of data are shown in Figure 3-21. The particular drain-temperature profiles shown are for the 15° conical bottom single tank configuration during EOI burn.

3.3.4.2 Pressurization Requirements

The series of runs analyzed in the preceeding subsection were also used to investigate the effects of compute-time
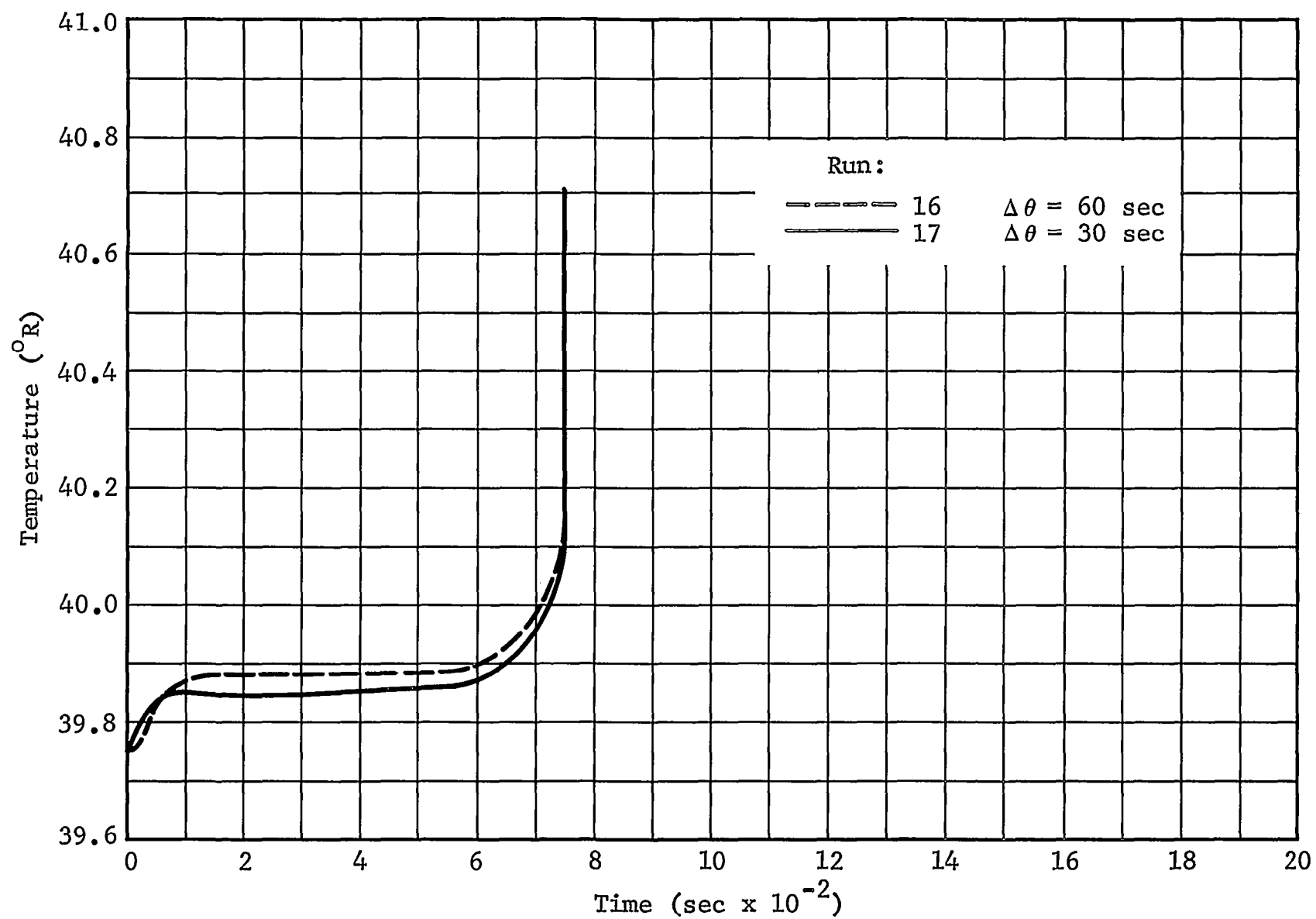
Figure 3-21   Effect of Compute-Time Increment on Drain —
Temperature Profiles

increment on pressurization requirements. The results of this investigation are shown in Table 3-3.

The numbers shown in Table 3-3 indicate that the smaller compute-time increments predicted smaller pressurant mass requirements (evaluated over the same time span). The longer run times and larger tank volumes showed the greatest differences. For example, on one hand, the 8.5° and 15° conical bottom single tank configurations had a 10 to 15% difference in pressurant required for the TLI burn. On the other hand, the pressurant requirements for the propulsion tank of the hybrid configuration were for all purposes identical with the maximum difference being 1.1 lb. The pressurant requirements for the 15° conical bottom single tank configuration are shown in Figure 3-22.

3.3.5 Acceleration Effects

A complete lunar shuttle mission was run at an acceleration of 1 g instead of the baseline 0.15 g as a means of investigating the effect of acceleration level on the drain-temperature profile and pressurant requirements. The drain-temperature profiles calculated under this condition for the 15° conical bottom single tank configuration are shown in Figure 3-23.

No marketed effects were found in any of the baseline mission segments. Since the run times were short (maximum 1800

Table 3-3

EFFECT OF COMPUTE-TIME INCREMENT ON PREDICTED PRESSURANT REQUIREMENTS

RUN NO. (TABLE 3-1)	COMPUTE-TIME INCR. (SEC)	TIME BASE (SEC)	CUM. PRESSURANT AT RUN TIME (lb_M)
1	30	900	1481
2	60	900	1750
16	60	720	2151
17	30	720	1905
24	30	90	154.8
28	10	90	154.1
25	30	150	171.0
29	10	150	170.5
26	30	150	172.6
30	10	150	171.9
27	50	90	156.4
31	10	90	155.3
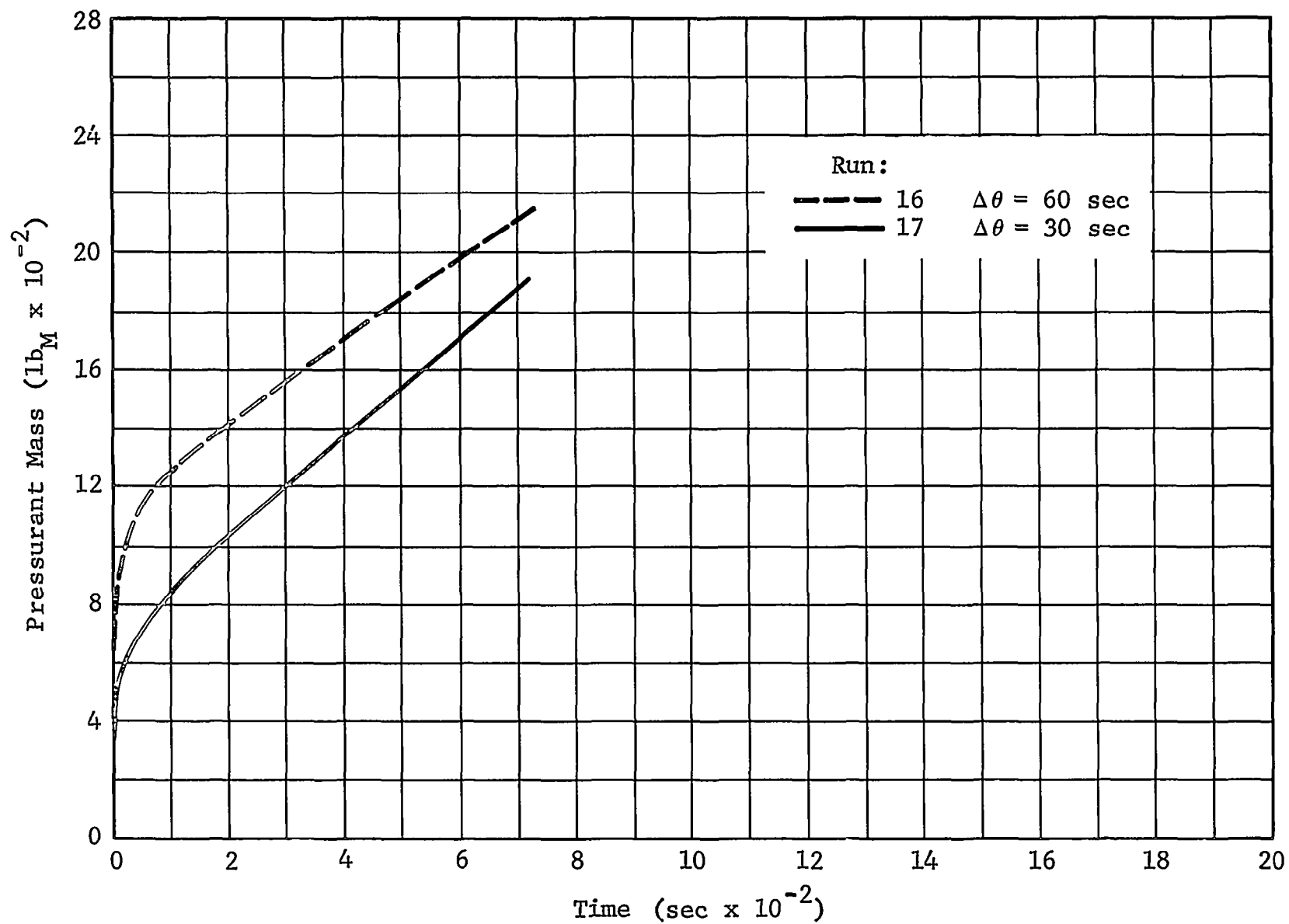
Figure 3-22 Effect of Compute-Time Increment on Pressurant Requirements
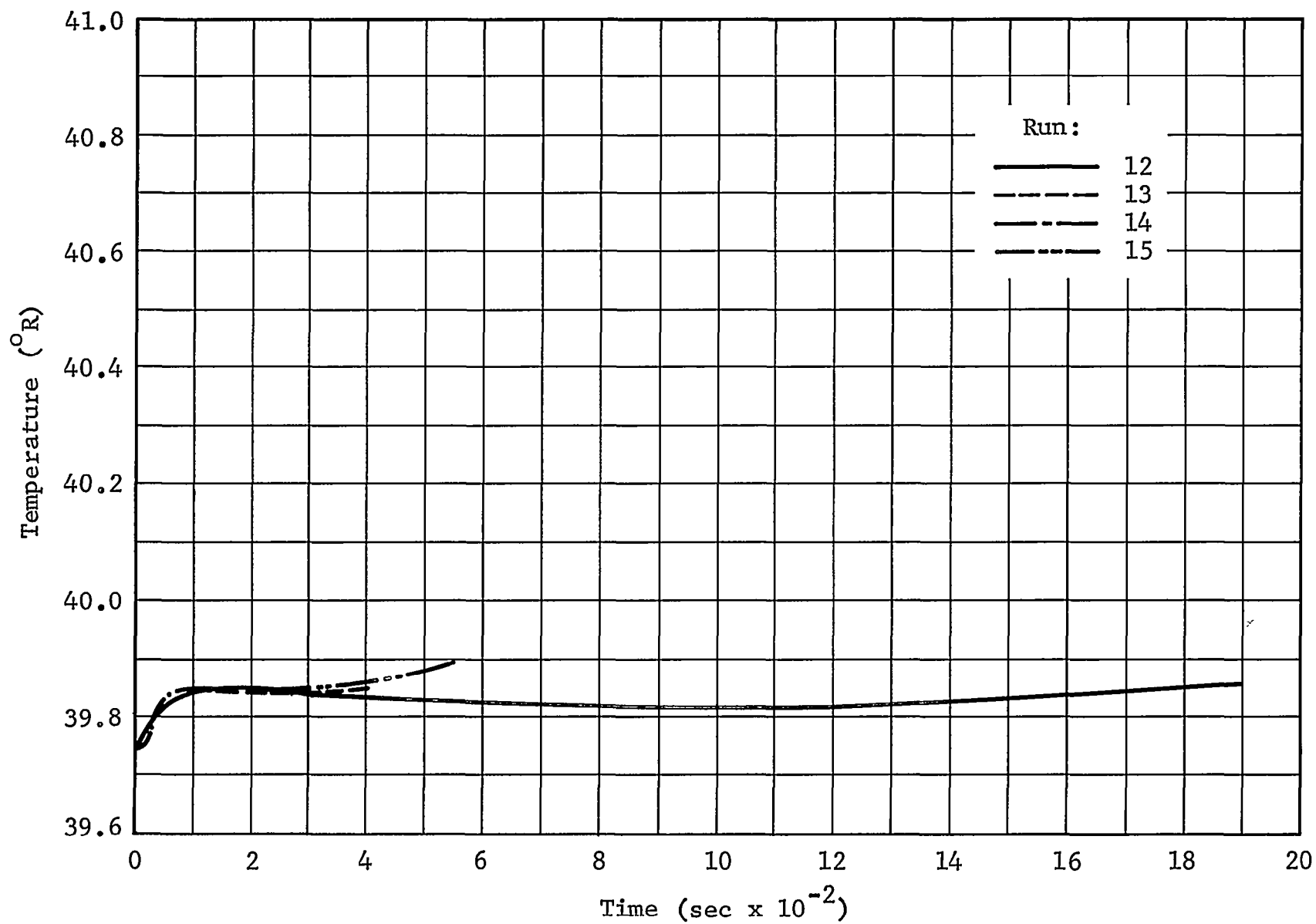
Figure 3-23   Drain-Temperature Profiles for 1-g Acceleration
Level — Single Tank 15° Conical Bottom Configuration

sec), very little stratification due to free convection took place, even though the acceleration level was 1 g, or roughly 7 times normal. A comparison of the EOI drain-temperature profiles for identical conditions except for acceleration level is shown in Figure 3-24. The data show a slight reduction in the compression heating spike and a faster temperature rise near the end of the burn due to an increased rate of stratification at 1 g.

No pressurant mass requirement effects (increase or decrease) were observed. This was as expected for several reasons. First, the ullage model used in AG4 is one node and hence does not allow for a stratified ullage, and second, the additional heat transfer from the tank walls to the ullage by free convection is not large enough to have a noticeable effect on the ullage mass during the relatively short burn period.

3.3.6 Pressurization Pressure Effects

Many different pressurization levels were investigated during the course of the study. The pressurant mass requirements for the four baseline configurations using these different levels are presented in Subsection 3.3.3 and will not be discussed here. Two salient points concerning tank pressurization and its effect upon drain temperature and pressurant mass will be discussed, namely, run pressure level and the difference, or delta pressure, between vent and run pressure levels.
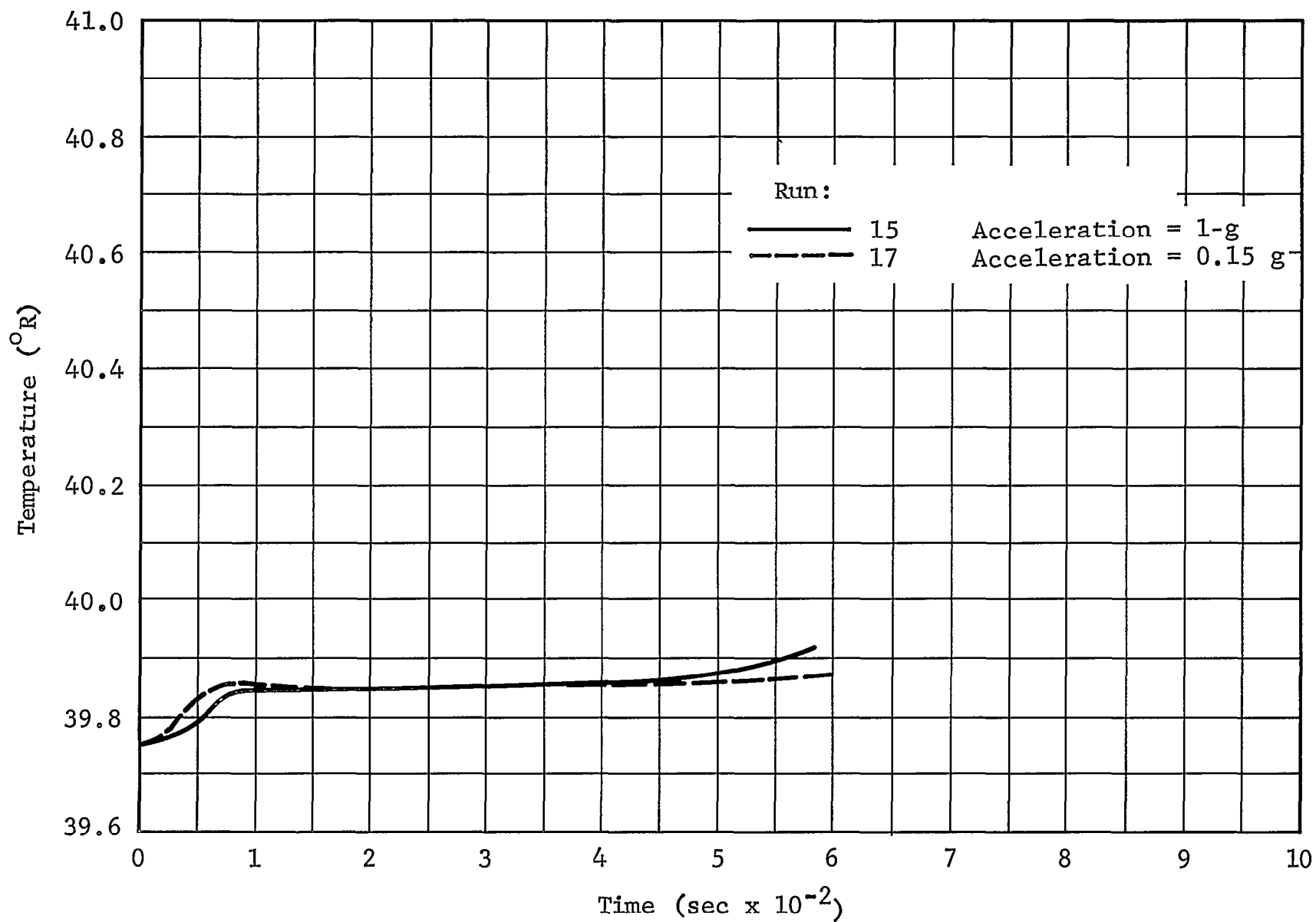
Figure 3-24   Effect of Acceleration on Drain-Temperature Profile

The run ullage pressure sets the propellant surface temperature. For example, if equilibrium conditions are assumed, an ullage pressure of 18 psia will dictate a surface temperature of about 37.75°R while an ullage pressure of 30 psia will support a surface temperature of approximately 41.36°R. If non-equilibrium conditions (stratified ullage and liquid) were to exist these temperatures would be generally higher. Equilibrium ullage conditions and ullage-liquid interface conditions were assumed in these studies. Drain temperatures for the 8° conical bottom single tank configuration during EOI burn are shown in Figure 3-25 for run pressures of 27.5 and 30 psia and with an initial (vent) pressure of 24 psia. The temperature profile for the 30-psia pressure shows a slightly higher compression heating hump and slightly higher temperature throughout the drain. For all practical purposes there is very little difference so long as any residual propellant is in the tank. The temperature profile also indicates that only a very thin stratified layer exists in the propellant. This is due to the assumption of a equilibrium condition at the vent pressure at start of burn.

The effect of the delta pressure (run/vent) is shown in Figure 3-26. The data show that the greater the difference in vent and run pressure the larger the pressurant mass requirement and the greater the initial mass flow rate. Tanks of
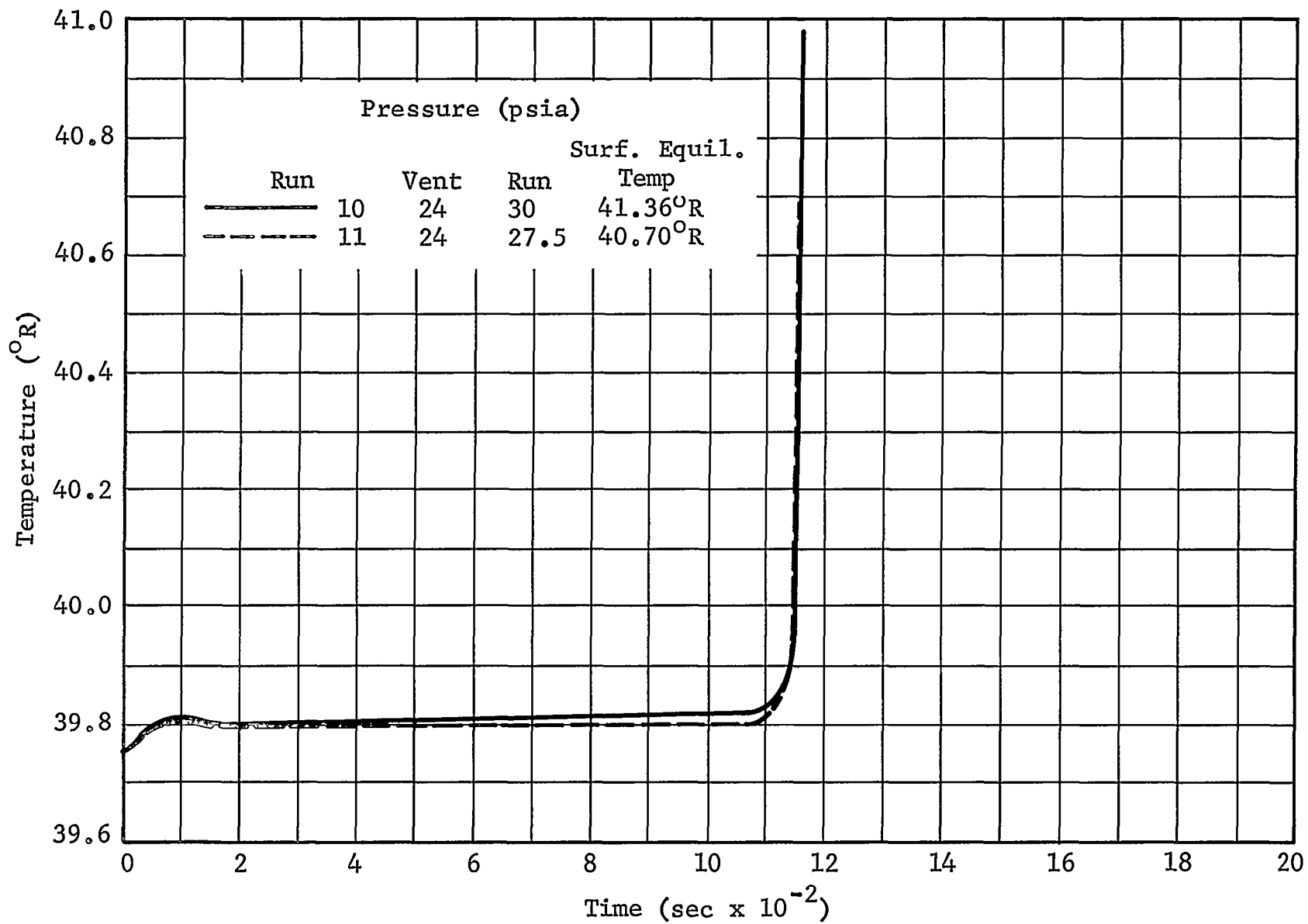
Figure 3-25   Effect of Tank Pressurization Level on Drain-Temperature Profile
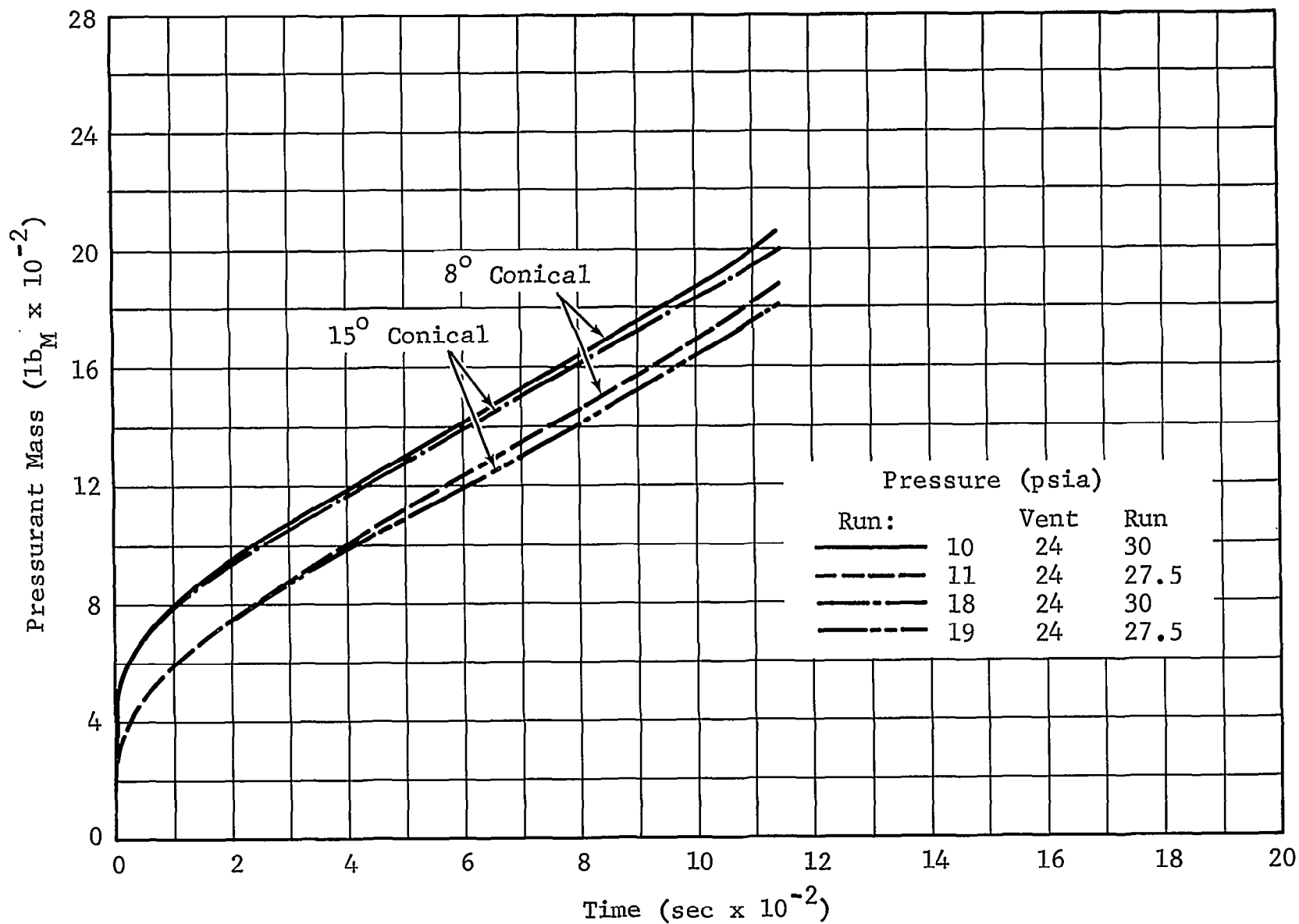
Figure 3-26   Effect of Tank Pressurization Level on Pressurant
Mass Requirements

similar volume exhibit similar tendencies, as can be seen in Figure 3-26 by comparing the 8° and 15° conical bottom single tank configuration data. The run tank and propulsion module of the hybrid and modular configurations showed similar trends.

3.3.7 Drain Rate Effects

Runs 24 and 25 (propulsion tank, hybrid configuration) were chosen to illustrate the effect that drain rate has on pressurant requirements and drain temperature. Run 24 has a drain rate of 91.6 lb/sec and Run 25, 59.5 lb/sec. The vent/run ullage pressures for both runs were 24/26.2 psia.

The effect of drain rate on pressurant requirements are shown in Figure 3-27. The total pressurant mass requirements for the two different flow rates are very close, within 30 lb. The pressurant gas flow rates are proportional to the drain rates. The trends shown by the results are as would be expected considering the physical situation.

The effect of drain rate on drain temperature is shown in Figure 3-28. The longer residence time of the propellant in the tank afforded by the lower flow rate allows the propellant to be heated more and allows stratification to build up to a greater extent. Both these effects are evident in the data presented in Figure 3-28.
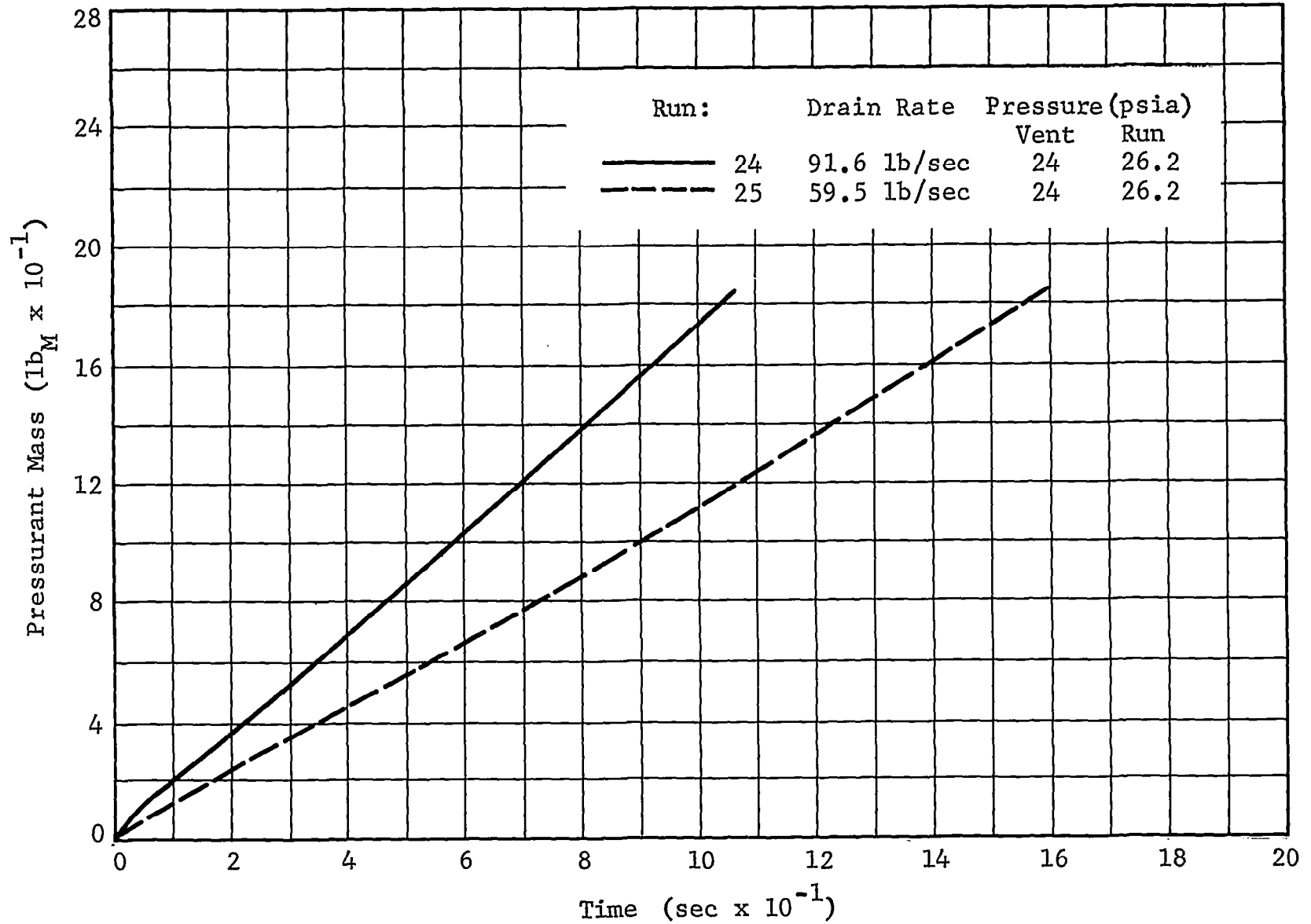
Figure 3-27 Effect of Drain Rate on Pressurant Requirements —
Propulsion Tank Hybrid Configuration

41.0

40.8

40.6

40.4

40.2

40.0

39.8

39.6

Temperature (^{o}R)

0   2   4   6   8   10   12   14   16   18   20

Time (sec x 10^{-1})

	Run:	Drain Rate	Pressure (psia)

Run: Drain Rate   Pressure (psia)
                                Vent   Run
——— 24   91.6 lb/sec   24   26.2
- - - 25   59.5 lb/sec   24   26.2
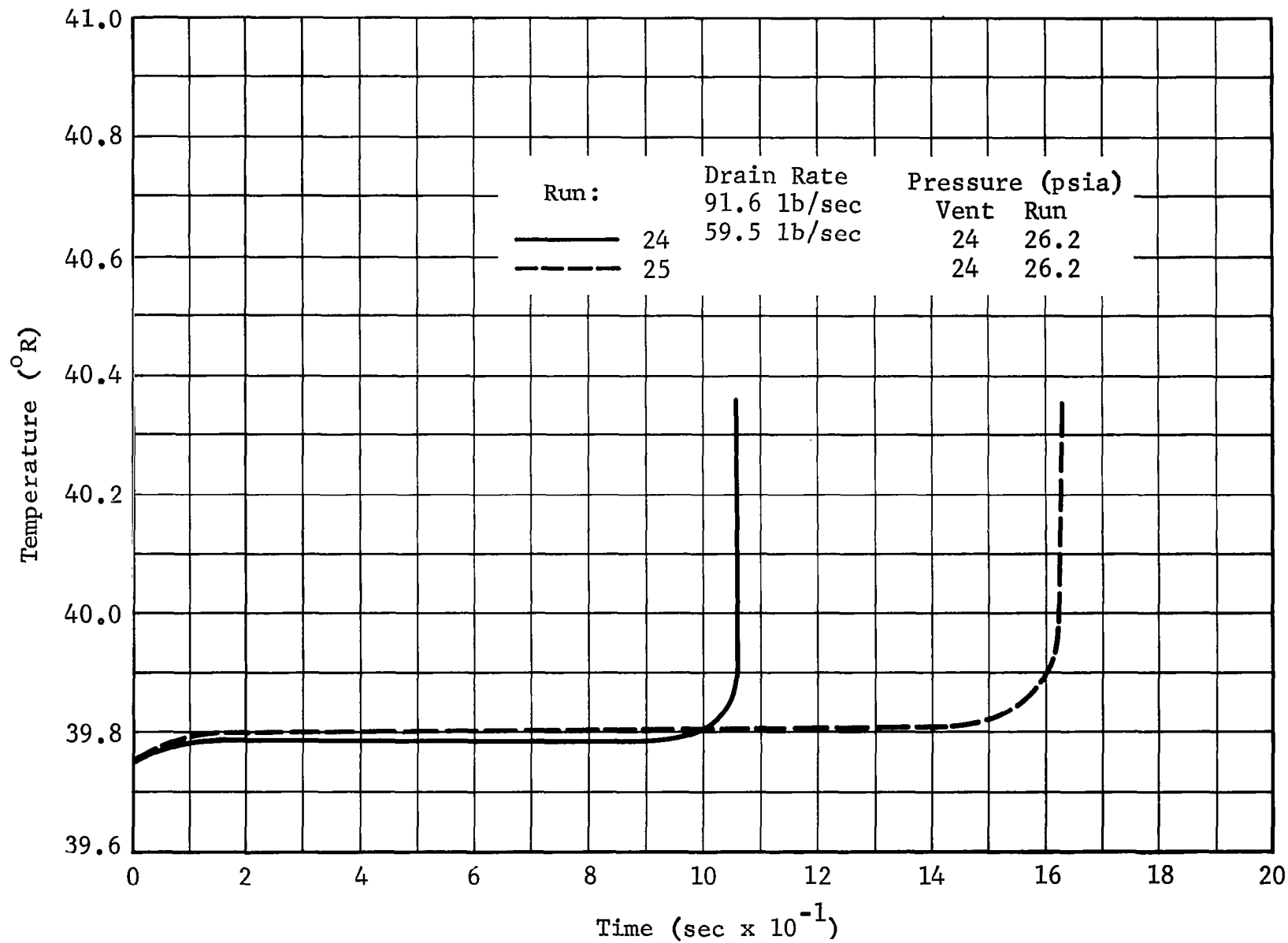
Figure 3-28   Effect of Drain Rate on Drain-Temperature Profile —
Propulsion Tank Hybrid Configuration

3.3.8 Auxiliary Internal Structure Effects

A cursory investigation into the effect of auxiliary structure and/or components such as antislosh baffles, antivortex baffles, propellant retention and acquisition systems, and thermal conditioning devices on the propellant thermodynamics and fluid dynamics was performed during this study. The results indicate that the nuclear heating of these components and structure could lead to convective (nonmechanical) mixing of the propellant during the burn portions of the mission. It is also possible, depending upon the location of the auxiliary components and structure, to have mixing during the cooldown portion of the mission. Although a thermodynamic vent is used in the sump, it is unlikely that it will be effective in removing the energy from the antivortex baffles and retention devices located at a distance from the heat exchanger coils of the vent system.

It was found that the impact of a mixed stratified propellant could be substantial in terms of the ΔT in the tanks of the various RNS configurations. In the case of mixed propellant, the ΔTs were always less than $0.5^{\circ}R$, while if stratification were allowed to occur the ΔTs could reach 6° to $8^{\circ}R$. The question of whether or not stratified or mixed propellant is desirable, and if so, to what degree, is dependent upon the pressurization methodology and planned residuals of the particular RNS configuration.

The important point is that stratification or the lack of it, i.e., mixing, must be predictable with a reasonable degree of accuracy. While much data and some criteria have been developed for the case of stratification due to sidewall heating, the effects of bottom wall heating and source heating of the LH_2 bulk and internal structure near the bottom of the tank on convective mixing and/or stratification are not as well known.

3.3.9 Para-Ortho Shift Effects

The radiation-induced conversion of parahydrogen to orthohydrogen in the propellant tank is unlikely to constitute a significant factor either in regard to nuclear heating rates or propellant properties. Radiation produces conversion efficiently only under conditions in which the pH_2-oH_2 transition corresponds to a decrease in free energy. Since the equilibrium composition of hydrogen at LH_2 temperature is over 99% pH_2, conversion of pH_2 cannot be effected by catalytic action and can only be induced by a process involving the dissociation of H_2 molecules. It can be shown that the absorption of nuclear energy by dissociative conversion is negligible compared to the thermal energy that would be evolved.

In principle, a prolonged irradiation of parahydrogen maintained at liquid hydrogen temperature by a heat sink would produce a steady-state composition consisting of 75% oH_2 and

3-53

25% pH_2. However, an amount of ionizing radiation sufficient to convert more than a few percent of the hydrogen in an adiabatic process would vaporize all of the hydrogen involved. Furthermore, even if the parahydrogen were 75% converted, the corresponding change in propellant properties would not represent a major design variable. The insensitivity of thermodynamic properties of liquid hydrogen to pH_2-oH_2 composition is due to the fact that both modifications are in their rotational ground states at low temperature. In this case thermodynamic disparities result only from minor differences in the equations of state. For example, at 38^oR the vapour pressure of liquid normal hydrogen (75% ortho) is only 0.6 psi less than that of parahydrogen (18.7 psia), or 3.2% below the absolute pH_2 vapour pressure.

Two pH_2-oH_2 problems that might conceivably arise under special conditions are as follows.

(1) If the hydrogen used in a propellant tank contained orthohydrogen in excess of the oH_2 fraction corresponding to equilibrium at operating temperature, radiation would cause equilibrium with a small release of energy. The amount of energy released would be only on the order of $1.3x + 2.6x^2$ (Btu/lb) where x is the excess orthohydrogen fraction.

(2) If hydrogen passing through the nozzle and reflector is used to pressurize the tank, the rate of mass transfer

between the warmed gas and the liquid would not conform exactly to the case of a parahydrogen pressurization, since the temperature of hydrogen passing through the reflector is in the range where radiation induced conversions may be appreciable.

The latter effect can result in a loss of energy available to turbines run on reflector-heat pickup, but this problem is not relevant to energy distribution in the propellant tank.

IV. EXPERIMENT SYNTHESIS AND DESIGN

This section presents the studies that were conducted in reviewing the work accomplished previously (Ref. 1) and in investigating the requirements imposed by the four baseline RNS configurations. The analyses, discussion of results, experimental equipment requirements, and test criteria are presented in the following subsections.

4.1 Scaling

Nuclear and ambient heating of the liquid hydrogen propellant can result in large weight penalties for the RNS. Evaluation of the severity of the weight penalties associated with these phenomena and the implications on RNS design are currently based primarily on analytical models.

The objectives of the propellant heating test (PHT) are to generate data that can be used to determine the accuracy and applicability of current analytical models, develop correlations useful in nuclear stage design, and simulate typical flight module conditions when possible. To achieve these objectives it is necessary to investigate the relevant physical phenomena, ranges of associated physical parameters, and the resultant implications on the establishment of scaling laws to be utilized in the design of the experiment (test).

The following subsections contain a discussion of the development of scaling parameters as well as a comparison of the range of these parameters expected in flight and ground test environments.

4.1.1 Scaling Parameter Development

When conducting tests with scale models, it is required that the physical phenomena be simulated so that the results may be applied with confidence to the full-scale conditions. Obviously, exact duplication of all physical parameters can be achieved only with full-scale testing, if at all. Exact duplication of all relevant similarity parameters in a scaled test would also ensure duplication of full-scale physical phenomena and the applicability of the results. This is, however, impossible in the case under consideration because of the complex nature of the problem and the number of variables involved. Thus it is necessary in practice to base scaling variables on duplication of the similarity parameters associated with those physical phenomena felt to be dominant, while additionally running extremes of test conditions to generate data that will be useful in case the selection of similarity parameters was not optimum.

Development of the scaling parameters was accomplished by two independent methods. The first method was the normalization of the governing differential equations that comprise the

mathematical model of an actively pressurized, draining cylindrical tank, with side and bottom heating, no ullage interaction, and a turbulent free-convection boundary layer. The second method used was a dimensional analysis of the model used in the normalization procedure. The details of these analyses are presented in Appendix A. The ten scaling parameters developed in the normalization and dimensional analysis procedures are listed below:

$$N_1 = \frac{x}{H_o} \qquad N_6 = \frac{\dot{w}}{\rho \nu D} = Re$$

$$N_2 = \frac{\nu t}{H_o^2} \qquad N_7 = \frac{g \beta q_w H_o^4}{k \nu^2} = Gr*$$

$$N_3 = \frac{T - T_i}{T_s - T_i} \qquad N_8 = \frac{q_b D^2}{\dot{w} c_p (T_s - T_i)}$$

$$N_4 = \frac{D}{H_o} \qquad N_9 = \frac{\dot{w}^2}{g \rho^2 D^4 H_o} = Fr$$

$$N_5 = \frac{q_b}{q_w} \qquad N_{10} = \frac{\nu c_p \rho}{k} = Pr$$

N_1, N_2, N_3 are nondimensional distance, time, and temperature, respectively. N_4 involves geometric similarity. N_5 is a relationship between heat inputs reaching the stratified layer and heat inputs deposited in the bulk. N_6 is a Reynolds number where the characteristic velocity is the surface velocity of the

draining tank ($V = \dot{w}/\rho D^2$). N_7 is the modified Grashof number, important to free-convection flow. N_8 relates to nondimensional bulk temperature rise. N_9 is the Froude number and is important to tank out-flow conditions. N_{10} is the Prandtl number of the liquid.

4.1.2 Comparison of Scaling Parameters

The scaling parameters and, hence, the test conditions must be varied over as wide a range as possible since both RNS tank geometry and engine operating parameters are subject to future change. The comparisons discussed in this subsection are based on the RNS variables presented in Table 4-1. The 15° conical bottom single tank and the propulsion tank of the modular configuration were chosen as typical tanks to illustrate the scaling parameters ranges available in the PHT. The PHT tank diameter, liquid height, and drain rate variables contained in this table are based on H_o/D and Reynolds number considerations and are nominal values.

Scaling groups N_1, N_2, and N_3 do not impose any design constraints on the experiment. Indeed, they may be thought of more as correlation parameters than strict scaling parameters. For example, in the case of temperature they simply indicate when and where comparable values between the RNS and the model can be found.

N_4 is a geometric constraint which was considered in the sizing of the tank. N_{10} is a scaling condition met by using the same fluid, liquid hydrogen in this case.

Table 4-1

COMPARISON OF VARIABLES

Variable	RNS				PHT	
	8° Conical	15° Conical	Hybrid	Modular	15° Conical	Modular
Diameter (ft)	33	33	33/13*	14.5	5.5	4.25
Liquid Level (ft)	149	105	91/21*	57	17	17
Gravity Ratio Coast (g/g_o) Fire	10^{-5} 0.12-0.35	10^{-5} 0.12-0.35	10^{-5} 0.12-0.35	10^{-5} 0.12-0.35	1.0	1.0
Drain Rate (lb/sec)	91.6	91.6	91.6	91.6	15.3	11.8
Sidewall Heat Flux (Btu/sec-ft^2)	1.8×10^{-5}	1.8×10^{-5}	1.8×10^{-5}	1.8×10^{-5}	4.0×10^{-5}	4.0×10^{-5}
Reactor Power (MW)	1575	1575	1575	1575	0-10	0-10

*Propellant/Propulsion

Group N_5 is the ratio of bottom-to-sidewall heat fluxes.
A comparison of this parameter between the RNS and the test tank
is shown in Figure 4-1. This scaling parameter is important in
defining the method by which energy is transferred into the
tank. The bottom heat flux, q_b, accounts for all energy passing
through the bottom of the tank. This includes the nuclear
energy deposited both in the tank wall and directly in the
liquid hydrogen. In addition, N_5 may be used to indicate how
much energy goes into the boundary layer relative to that which
goes into the core. High core heating may cause bulk mixing
and therefore reduce stratification.

The Reynolds number, N_6, represents the relationship be-
tween the inertia and viscous forces which influence both the
free-convection and forced-convection boundary-layer charac-
teristics. The forced-convection boundary layer is caused by
draining the tank.

Figure 4-2 indicates how Reynolds number for the PHT tank
compares with that for the RNS.

The modified Grashof number Gr*, N_7, is a ratio of the
buoyant and viscous forces. These forces govern the natural
convection process for a constant wall-heat-flux condition.
Because of the fourth power dependence on H, a small-scale tank
would require a large increase in sidewall heat flux to dupli-
cate the full-scale Gr* if the same fluid is used. These high
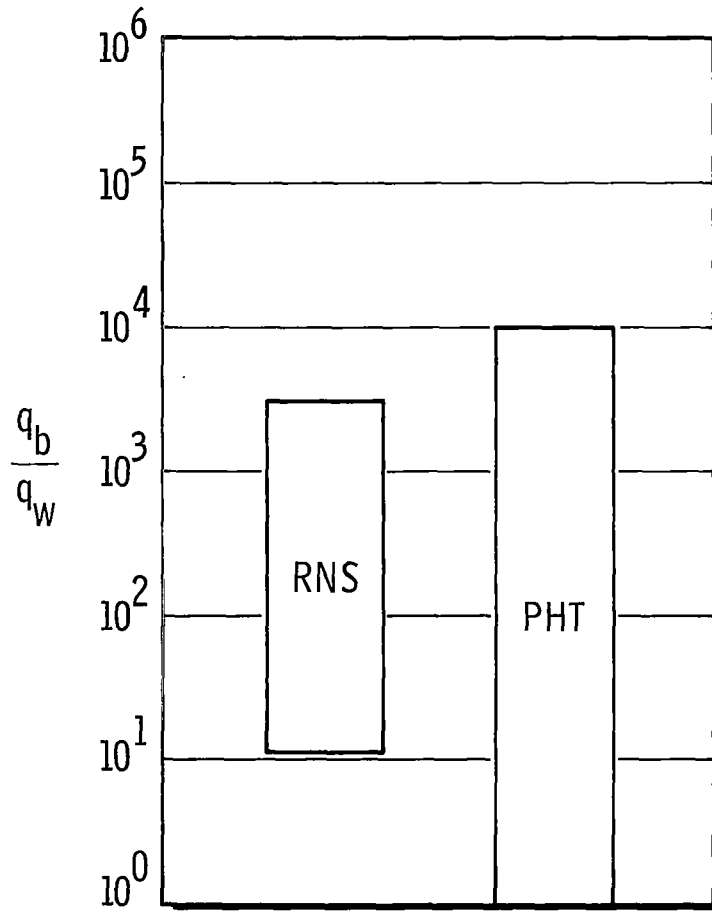
Figure 4-1 Bottom-to-Sidewall Heat-Flux
           Ratio
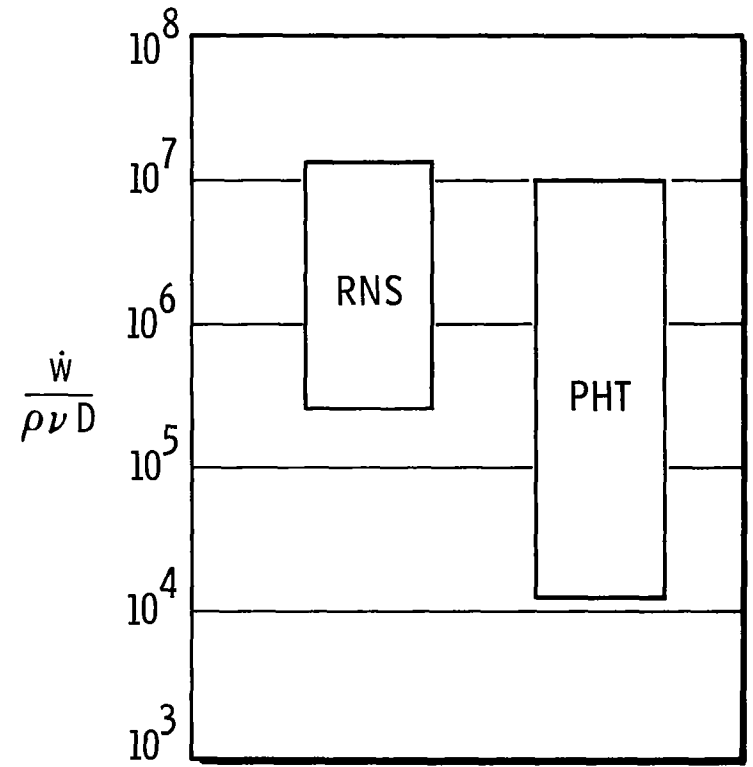
Figure 4-2 Reynolds Number

heat fluxes would cause boiling and change the fluid dynamic as well as thermodynamic nature of the problem. Therefore, it is not possible to duplicate the Gr* exactly. It has been found experimentally, however, that it is necessary only that the boundary layer be similar in basic nature, that is, either turbulent or laminar. Figure 4-3 shows that a turbulent boundary layer is to be expected in both the PHT tank and RNS.

Figure 4-4 shows a comparison of the parameter N_9, the Froude number, which indicates the relation between inertial and gravitational forces that govern the free-surface and draining conditions. This parameter is of interest for matching RNS and PHT tank suction dip characteristics.

Nondimensional parameters, other than those derived above, could well be important to drain-temperature profiles. The quantities of energy deposited in the bottom tank wall, in the internal structural arrangements near the bottom, and in the LH_2 near the drain suggest the possibility that some energy may be carried out the drain line before it can mix with the bulk fluid. This could alter drain-temperature profiles and, thus, fuel residuals. In this connection, in addition to the Froude number previously mentioned, the spatial distribution of the heating would also be important. However, it is felt that without further experimental insight, it is not justifiable to develop additional scaling parameters at this time.

$$\frac{\dot{w}^2}{g\rho^2 D^4 H_o}$$

Figure 4-4   Froude Number

$$\frac{g\beta q_w H_o^4}{k\nu^2}$$
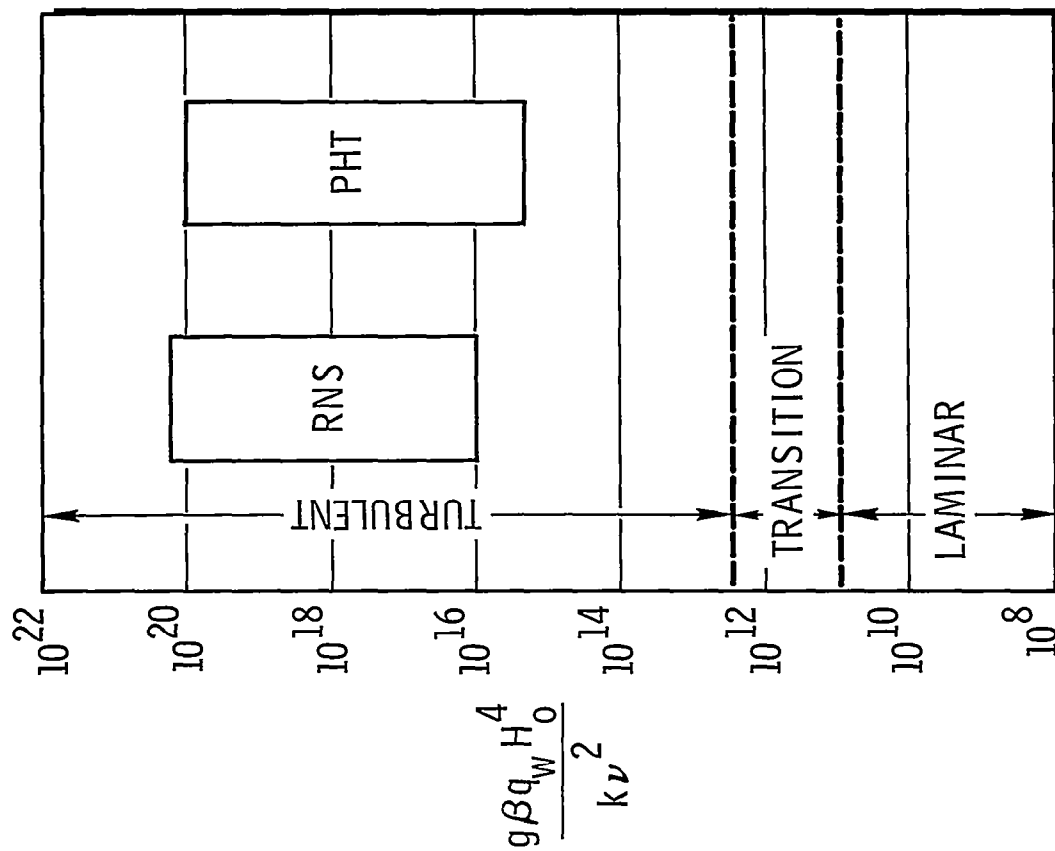
Figure 4-3   Modified Grashof Number
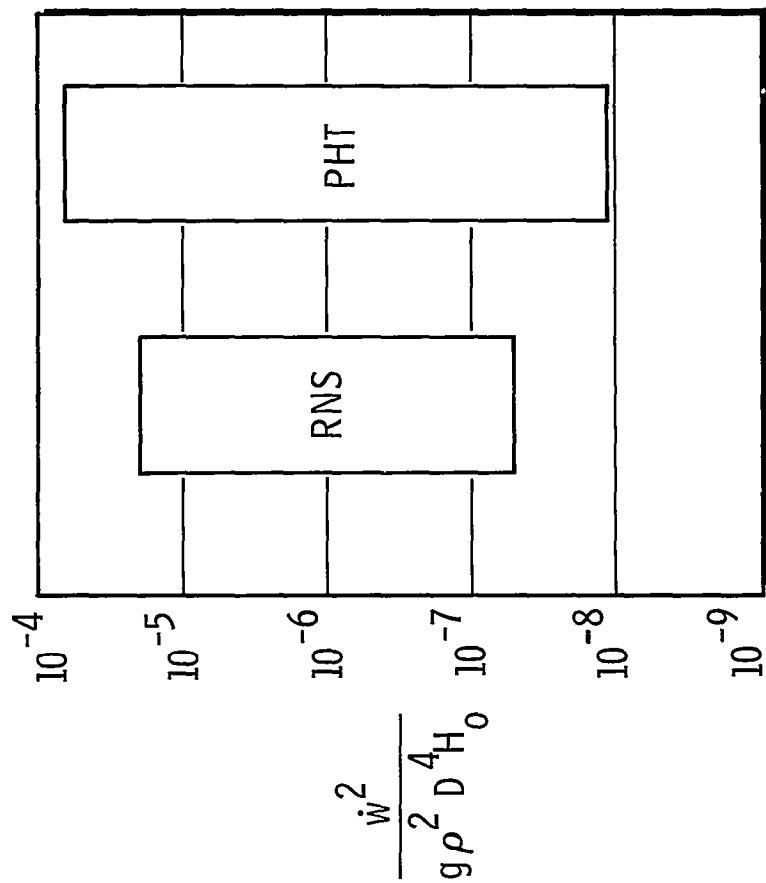
4.2 Propellant Heating Test Analytical Studies

The analytical work performed in investigating the PHT con-
sisted of test tank selection and facility compatability
studies, determination of nuclear and ambient heating rates,
calculation of typical drain-temperature profiles for various
test conditions, an investigation of the stratification and de-
stratification test conditions obtainable, and a definition of
the pressurization and ullage behavior of the test tank.

Analyses performed in Section III indicated that for the
particular stage operating assumptions used, the EOI burn is
the most critical from the fluid dynamic and thermodynamic
stand-point. This is especially true when operating in the mal-
function (single pump) mode. For this reason the stage operat-
ing conditions of the EOI mission segment were chosen as a
representative set of test conditions in determining the PHT
characteristics.

4.2.1 Tank Selection

Preliminary sizing studies for the test tank and facility
were conducted to determine the feasibility of modeling any one
of the four baseline RNS configurations in the Fort Worth opera-
tion's Aerospace Systems Test Reactor (ASTR) facility. The
results indicate that based on both the scaling parameters
developed in Sec. 4.1 and the physical constraints, all four
baseline RNS configurations can be adequately modeled in the

ASTR facility. Schematics of the test tank setup in the ASTR facility for round bottoms and conical bottom tanks are shown in Figures 4-5 and 4-6, respectively. The 160-in.-diameter, 253-in.-high propulsion tank of the Class 1 hybrid was selected for study. This tank has several advantages, one of which is that it represents a typical RNS configuration. A schematic of this tank in the ASTR facility is shown in Figure 4-7.

The test tank will be of a dewar-type (double wall with vacuum) construction. Auxiliary heaters will be located on the exterior of the inner tank. These heaters will allow heat leaks and different wall heating profiles to be simulated. Propellant fill and drain lines and pressurant lines will be located and sized as dictated by the RNS design. For purposes of analysis, the inner tank material was assumed to be aluminum with the forward and aft bulkheads being 0.030 in. thick and the cylinder 0.055 in. thick.

4.2.2 Heating Rates

To determine the thermodynamic state of the propellant and fluid dynamic effects caused by free convection it is necessary to know the amount of energy in and transferred to the liquid hydrogen and ullage by nuclear and ambient heating. The heating rates due to these sources for the test configuration shown in Figure 4-7 are discussed in the following subsections.
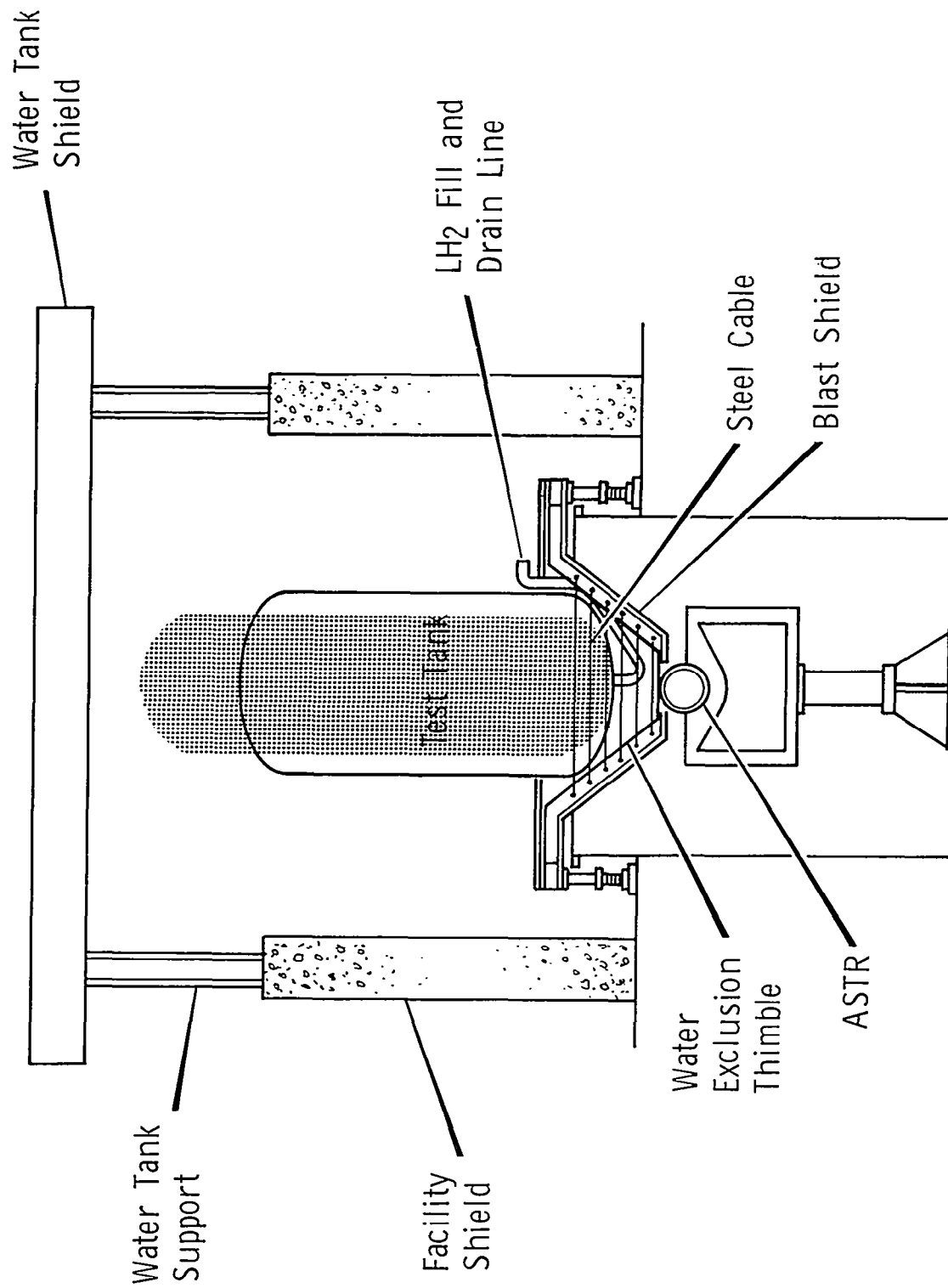
Figure 4-5 ASTR/Test Tank Schematic for Round Bottom Tanks
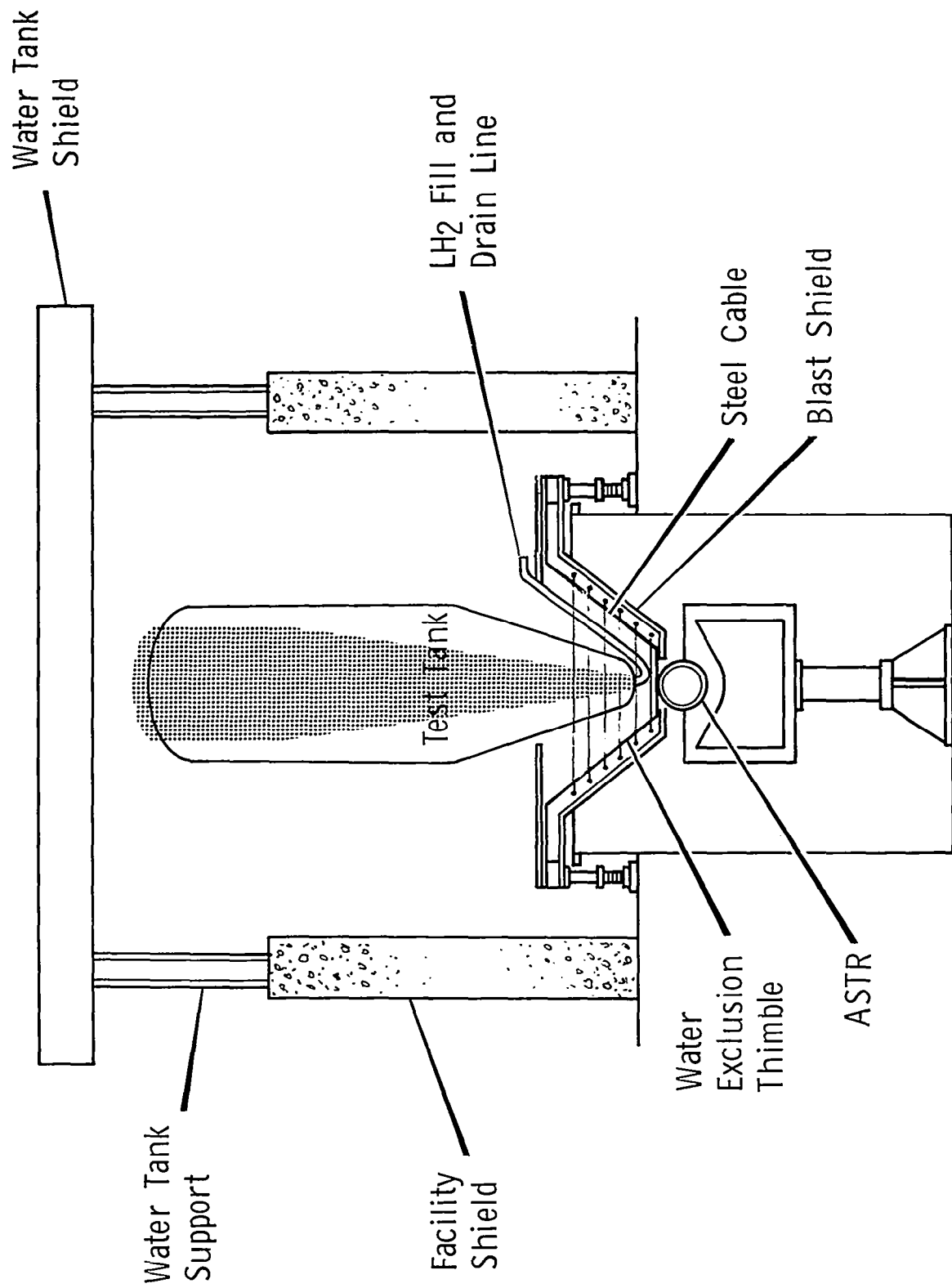
Figure 4-6   ASTR/Test Tank Schematic Conical Bottom Tanks
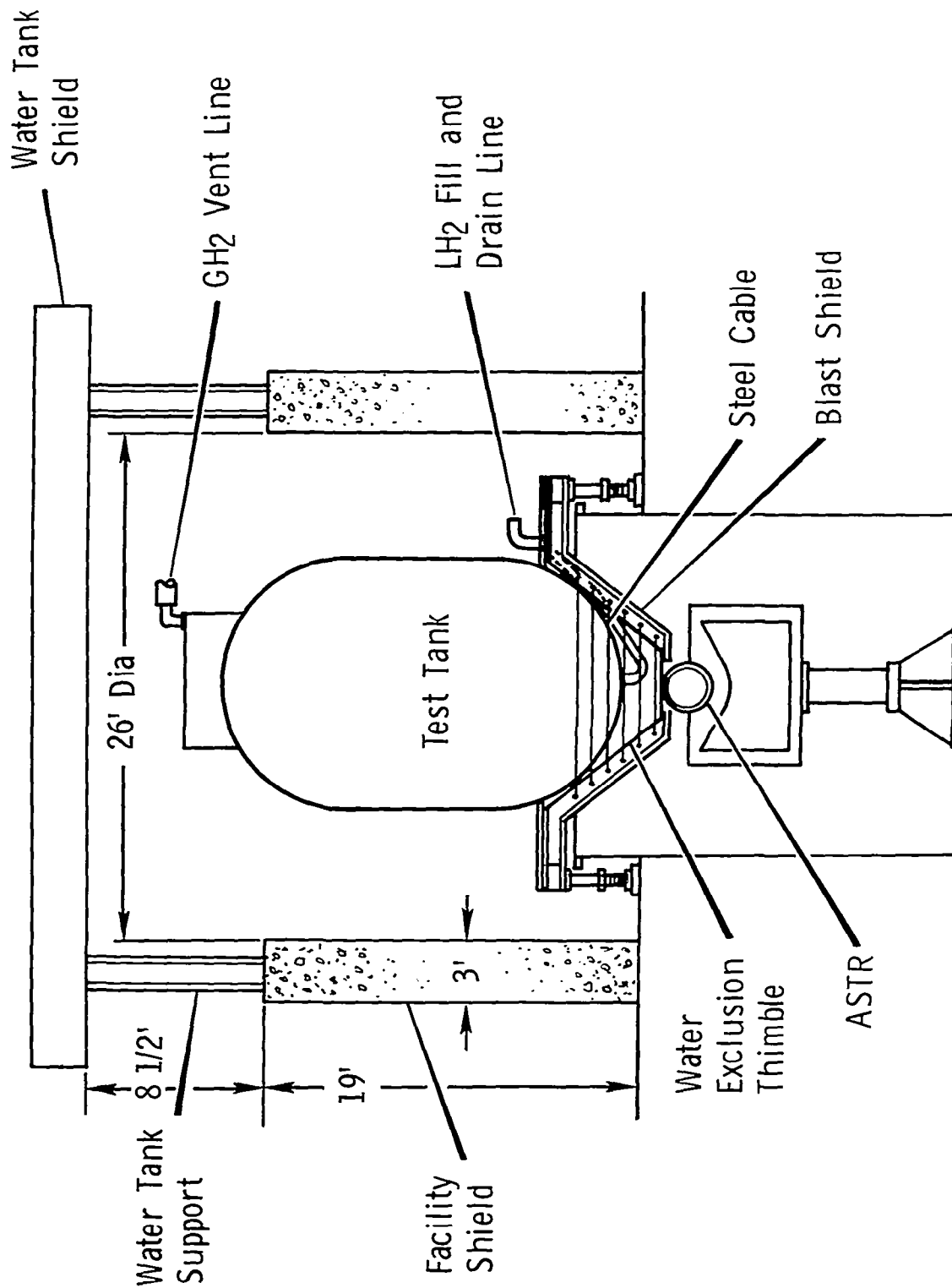
Figure 4-7 Full Scale Propulsion Tank — Hybrid Configuration in ASTR Facility

4.2.2.1 Nuclear Heating

Details of the method of calculation of the nuclear energy deposited in liquid hydrogen and the tank wall are discussed in Section II. The resulting nuclear heating rates are discussed in Subsection 2.2.5 and are shown in plotted form in Figure 2.13. The data presented show that the bulk heating is predicted to be 538 watts/MW, or at the full-power rating of the ASTR (10 MW) 5,380 watts. This compares favorably with the 6230 watts predicted for the flight configuration of the 1575-MW NERVA. The wall heating is predicted to be 12.4 watts/MW, or 124 watts at 10 MW. The corresponding heating rate of the flight configuration is 137 watts.

The heating rates can be, of course, varied over a wide range by running the reactor at different power levels. The bulk and wall heating rates can be increased over the values mentioned above by different methods. The bulk heating can be increased by decreasing the size of the tank from full size to some smaller scale and adjusting the "window" on the ASTR so as to deposit the majority of the nuclear radiation within the tank. The wall heating can be increased by increasing the wall thickness or by coating the wall with a radiation absorbing material.

4.2.2.2 Ambient Heating

The baseline value for the sidewall heat leak used in the PHT analytical predictions is 1.8×10^{-5} Btu/ft^2-sec. Since the design of the test tank will provide a means of varying the sidewall heating, additional values of 4, 9, and 18×10^{-5} Btu/ft^2-sec were also used in the analytical studies. Penetration heat leaks were not studied because the computer codes (AG4 and RIO) used for analyzing the tank thermodynamic and fluid dynamics are not capable of predicting the effects of point heat leaks.

4.2.3 Drain Temperatures

In order to have a consistent base from which to evaluate the drain-temperature profiles of the various test conditions, the following assumption were made:

1. Propellant settled at start of drain.

2. Propellant and ullage in thermal equilibrium at vent pressure at start of drain.

3. Drain rate reached instantaneously at start of drain.

4. Pressurant gas (GH_2) at a constant temperature of 230°R.

5. Wall and bulk nuclear heating instantaneous at start of drain.

As can be seen in Tables 4-2 and 4-3, drain temperatures were calculated for a wide range of test conditions. The results of the drain temperature and pressurant requirement studies are discussed in the following subsections.

Table 4-2

TEST CONDITIONS STUDIED
USING CODE RIO

RUN NO.	DRAIN RATE (lb/sec)	AMBIENT WALL HEATING (Btu/ft^2-secx10^5)	ULLAGE PRESS. (PSIA) VENT – RUN	REACTOR POWER (MW)
1 RN	91.6	1.8	24-26.2	10
2	91.6			5
3	91.6			1
4	59.5			10
5	59.5			5
6	59.5		24-26.2	1
7	91.6		24-30	10
8	91.6			5
9	91.6			1
10	59.5			10
11	59.5			5
12	59.5			1
13	30.0			10
14	30.0			5
15	30.0		24-30	1
16	91.6		14.7-16.9	10
17	59.5		14.7-16.9	
18	30.0	1.8	14.7-16.9	
19	30.0	4.0	24-26.2	
20	30.0	9.0		
21	15.0	1.8		
22	15.0	4.0		
23	15.0	9.0		
24	91.6	4.0		
25	91.6	9.0		
26	59.5	4.0		
27	59.5	9.0		
28	59.5	18.0		
29	91.6			
30	30.0			
31 RN	15.0	18.0	24-26.2	10

Table 4-3

TEST CONDITIONS STUDIED
USING CODE AG4

RUN No.	DRAIN RATE (lb/sec)	AMBIENT WALL HEATING (Btu/ft^2-sec x 10^5)	ULLAGE PRESS. (PSIA) VENT - RUN	REACTOR POWER (MW)
1 AN	91.6	1.8	24-26.2	10
2	59.5		24-26.2	
3	30.0		24-26.2	
4	91.6		14.7-16.9	
5	59.5		14.7-16.9	
6 AN	30.0	1.8	14.7-16.9	10

4.2.3.1 Drain Rate Effects

The total amount of nuclear energy deposited in the liquid hydrogen and in the tank wall is a function of time. Therefore, the lower the flow rate the greater the rise in drain temperature will be. Figures 4-8 through 4-11 show the drain temperature rise calculated using code RIO for drain rates of 91.6, 59.5, 30, and 15 lb/sec respectively. The test conditions for these runs were: reactor power 10 MW, run pressure 30 psia, wall heating 1.8×10^{-5} Btu/ft^2-sec.

The temperature rise evaluated just prior to complete drain varies from a low of 0.1^{O}R at 91.6 lb/sec to high of 0.5^{O}R at 15 lb/sec. These temperature rises are probably as low as can be expected since the drain temperature rise would be much greater if the tank were not vented prior to drain, that is, if nonequilibrium conditions (stratification) existed at the start of pressurization and drain. Also the nuclear heating of internal structure such as slosh and antivortex baffles as well as propellant retention screens would also tend to increase the drain temperature.

It is interesting to compare the PHT drain temperature predictions shown in Figures 4-8 and 4-9 with those predicted for the RNS flight case under identical stage operating parameters as given in Figures 3-14 and 3-15, respectively. The profiles are identical in shape and are for all practical
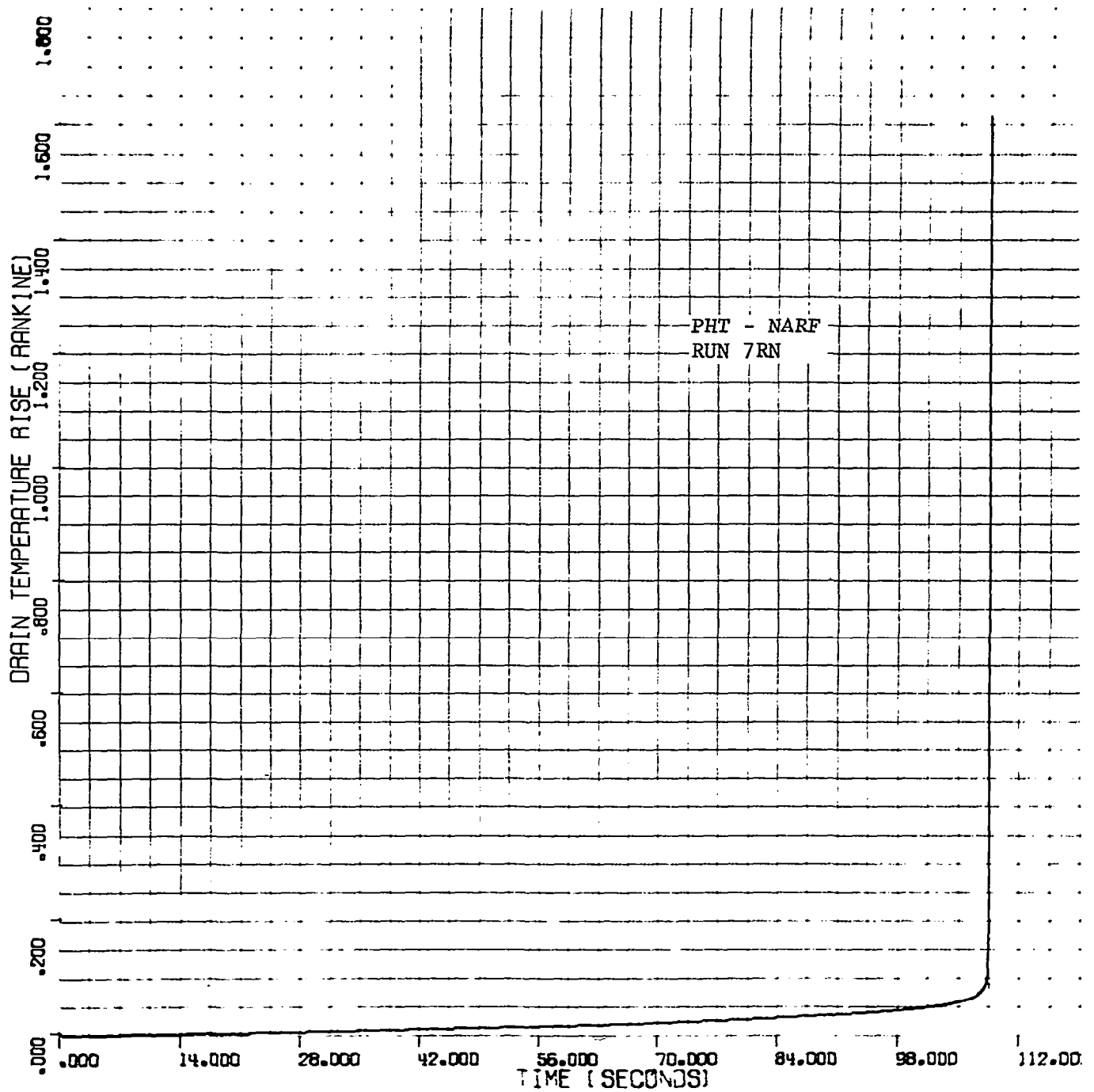
Figure 4-8   PHT Drain Temperature Profile For 91.6 lb/sec
Drain Rate
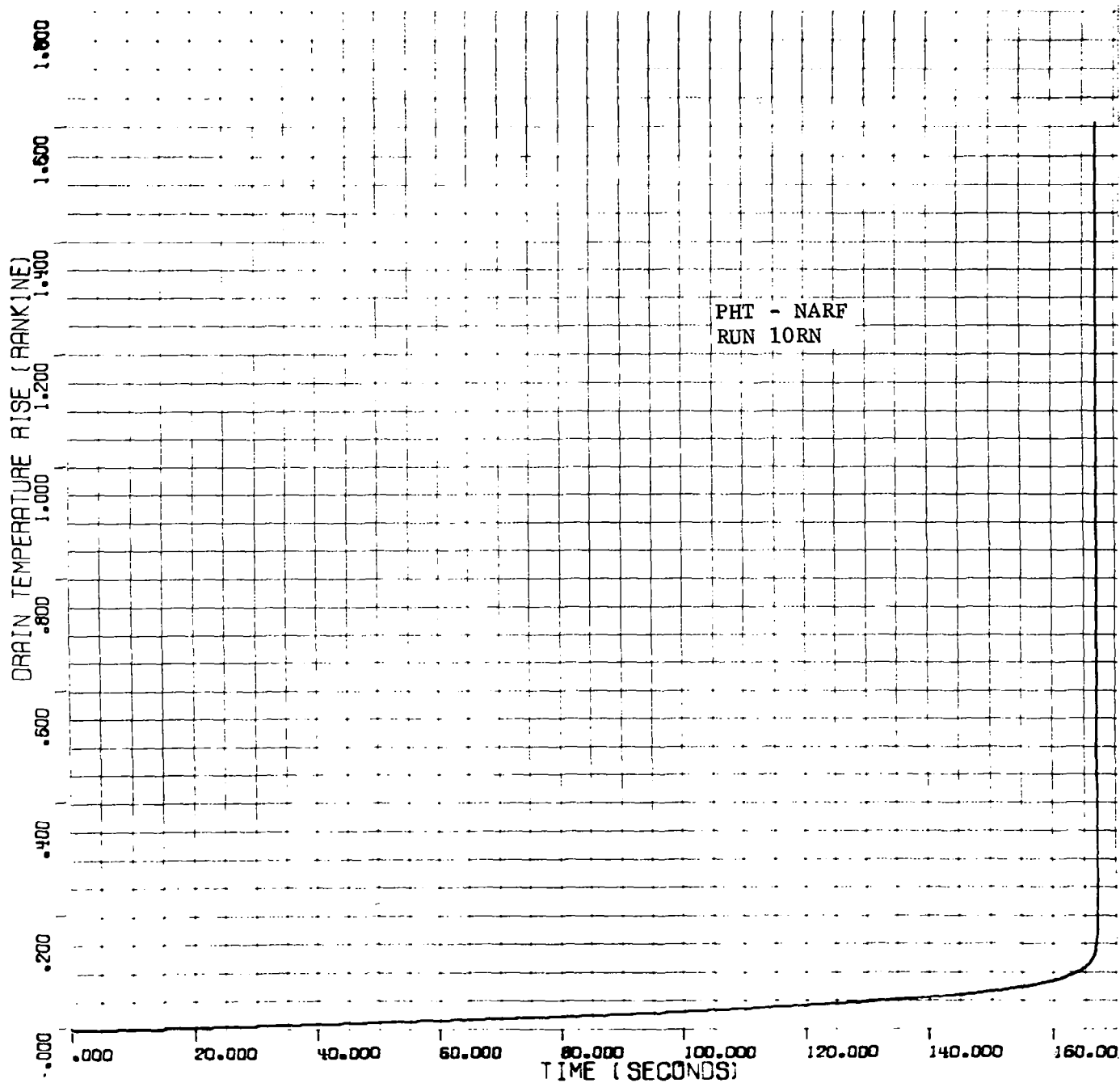
Figure 4-9   PHT Drain Temperature Profile For 595 lb/sec Drain Rate
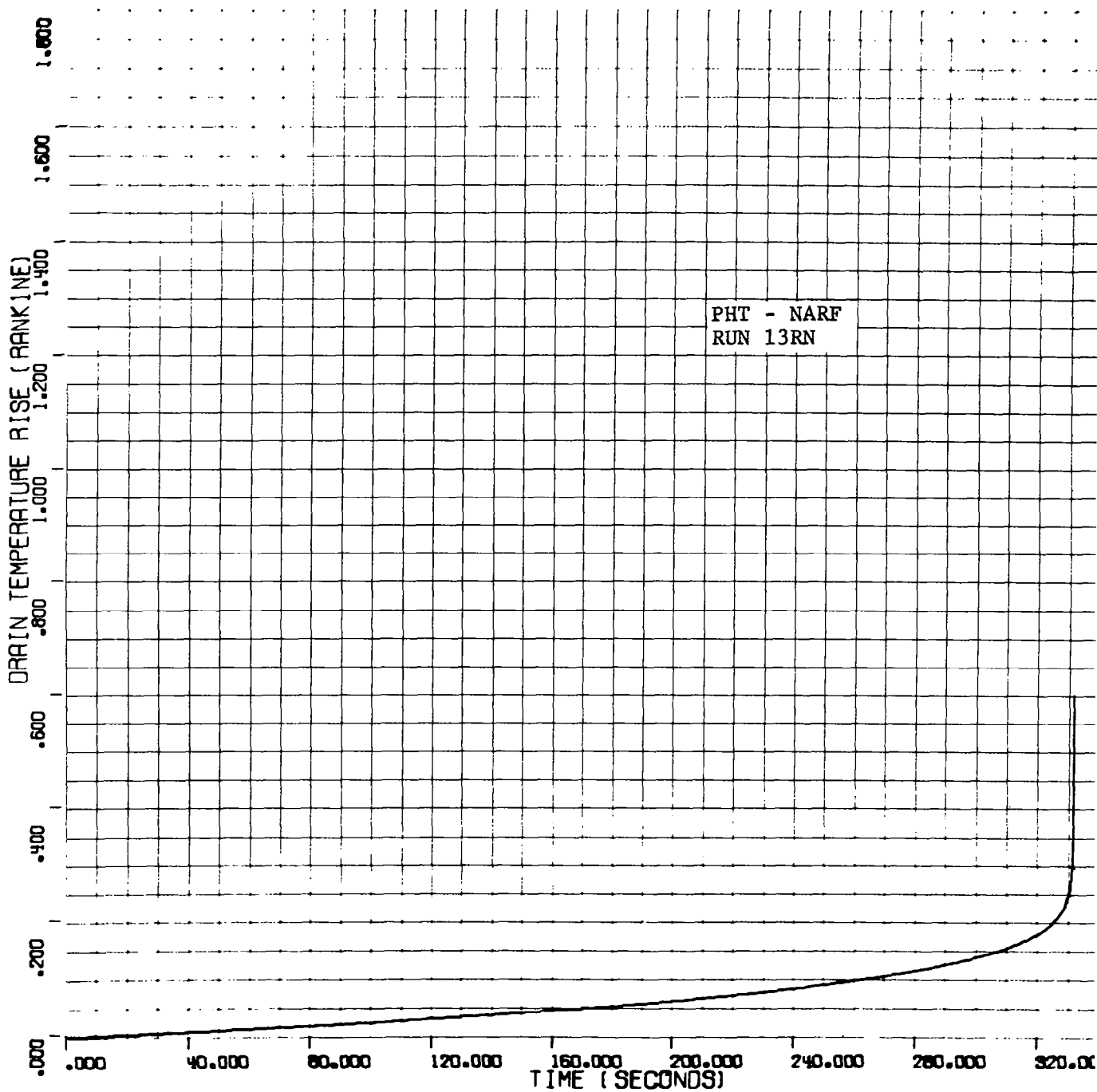
Figure 4-10   PHT Drain Temperature Profile For 30 lb/sec Drain Rate
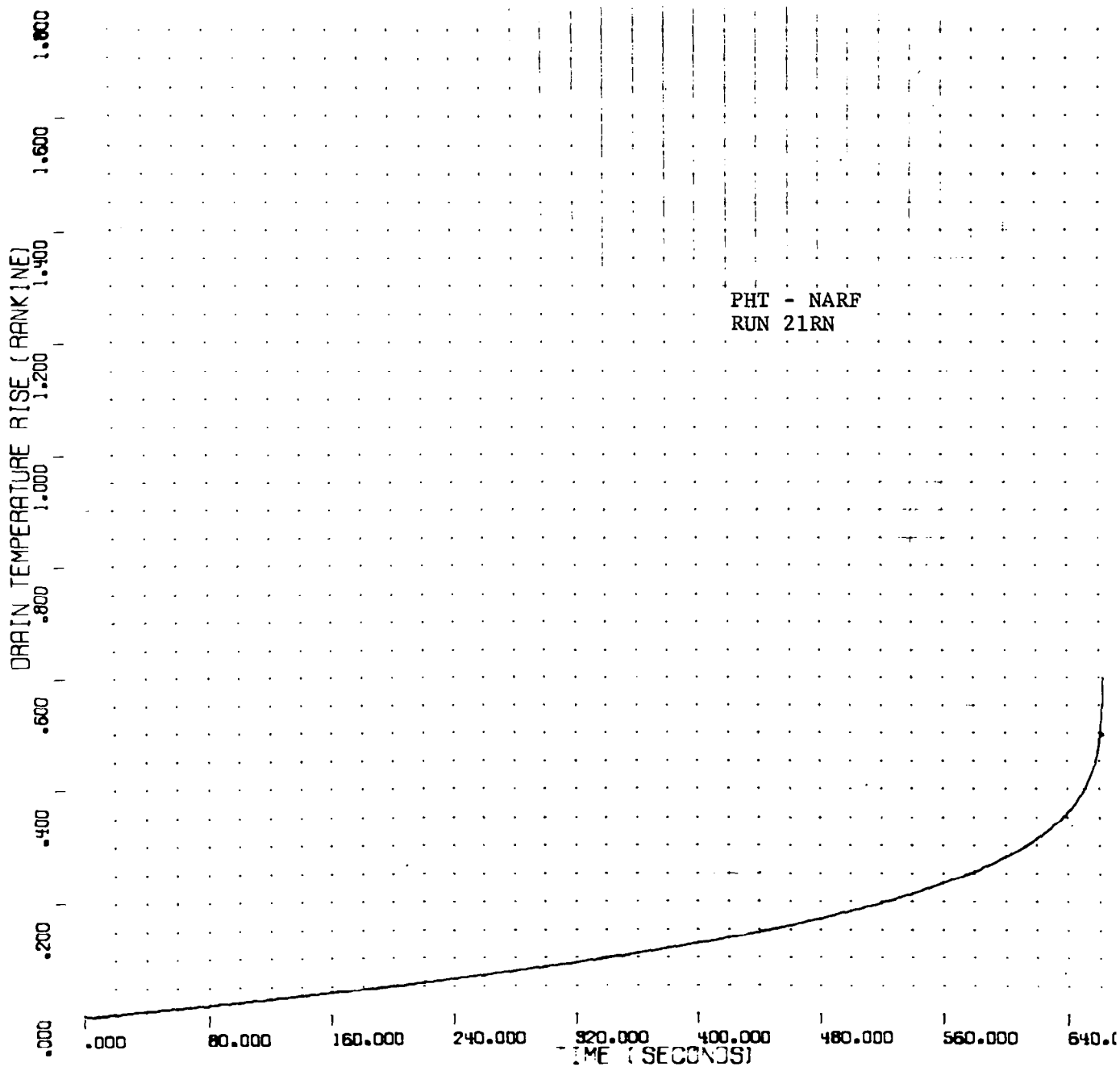
Figure 4-11   PHT Drain Temperature Profile For 15 lb/sec Drain Rate

considerations identical in time-temperature. This indicates
that the RNS propulsion tank(s) drain-temperature profiles can
be simulated in the PHT facility.

4.2.3.2 Reactor Power Effects

The effect of reactor power level on the drain-temperature
profile is similar to that of drain rate - the higher the
reactor power the greater the temperature rise. This effect
for a drain rate of 59.5 lb/sec is shown in Figure 4-12. The
temperature rise for all power levels is fairly small; the
1 MW reactor power case could not be accurately measured. At
reactor powers of 5 MW or greater (for this test tank configura-
tion) accurate drain-temperature profiles could be obtained.
As was discussed earlier, a smaller tank would yield greater
temperature rises.

4.2.3.3 Sidewall Heating Effects

The sidewall heating was varied from a low of 1.8×10^{-5}
to a high of 18×10^{-5} Btu/ft^2-sec. The effect on the drain-
temperature profile over this range was found to be nil. In
fact, the two drain-temperature profiles were identical for all
practical purposes. While these results indicate that within
the range studied sidewall heating has little effect during drain,
the effect on long-term storage tank thermodynamics can not be
neglected.
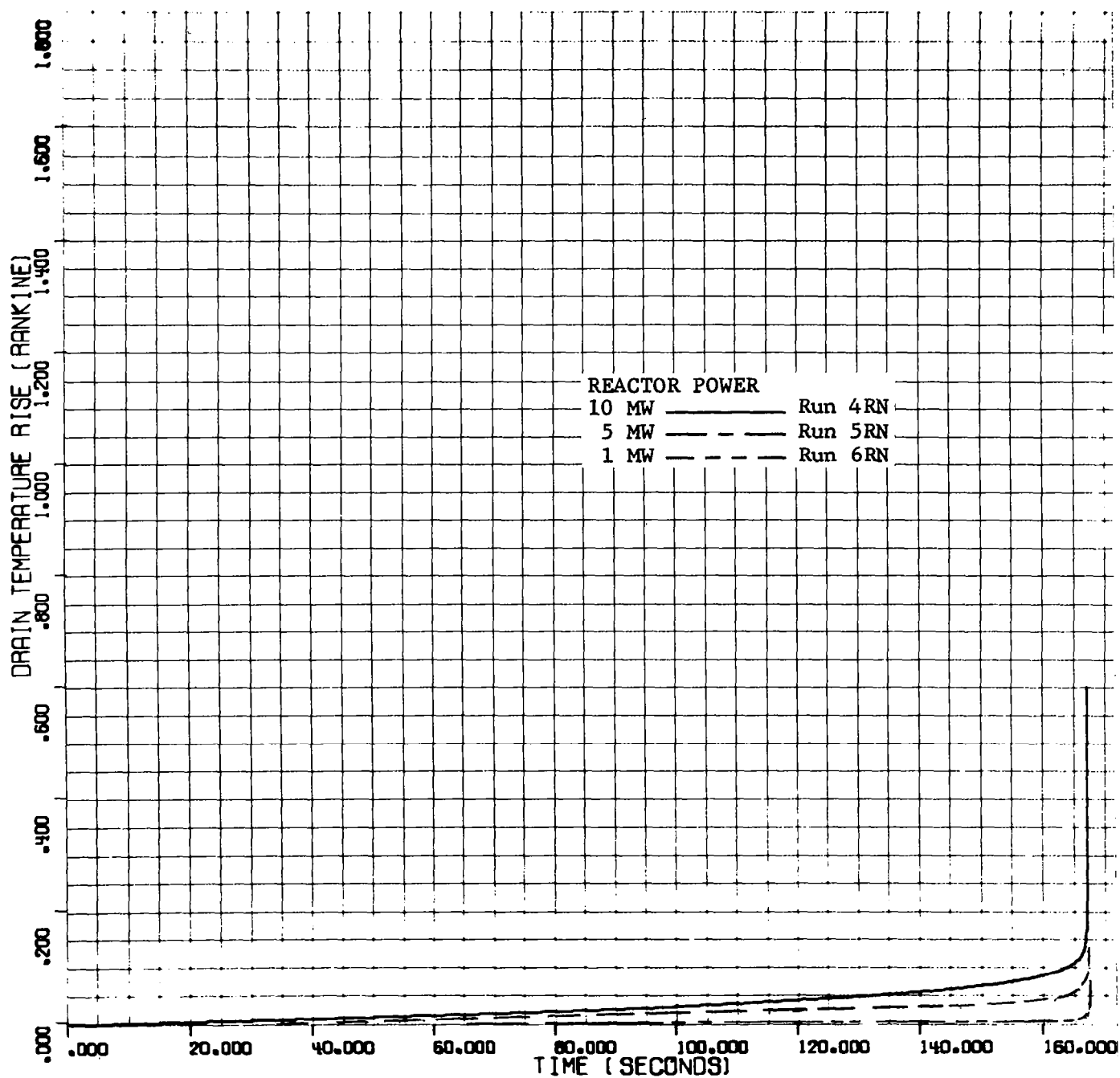
Figure 4-12 Effect of Reactor Power on PHT Drain Temperature Profile

4.2.3.4 Computational Effects on Drain Temperatures

The temperature profiles predicted by the two computer codes used in this study were found to be different for identical input. The drain-temperature profiles calculated by RIO and AG4 for identical conditions are shown in Figure 4-13. The AG4 profile shows an initial rise in temperature followed by a fairly flat section and then a sharp rise near the end of the drain period. The RIO profile shows a fairly steady rise that accelerates near the end of drain. The significance of the profile shape is in the prediction of the amount of residuals that might occur if a complete drain were necessary. In general, code AG4 would predict lower residuals.

4.2.4 Pressurant Requirements

The pressurant requirements were predicted for three flow rates and two vent/run pressure schedules. The flow rates were 91.6, 59.5, and 30 lb/sec and the vent/run pressures were 24/26.2 psia and 14.7/16.9 psia. The results are shown in Figures 4-14 and 4-15.

The data in these figures show that the total pressurant mass required is not a strong function of either flow rate or pressure level. The requirements for all six runs vary from about 170 lb to 190 lb. The pressurant flow rates, of course, vary directly with drain rate as can be seen by comparing the shape of the plots down in Figures 4-14 and 4-15.
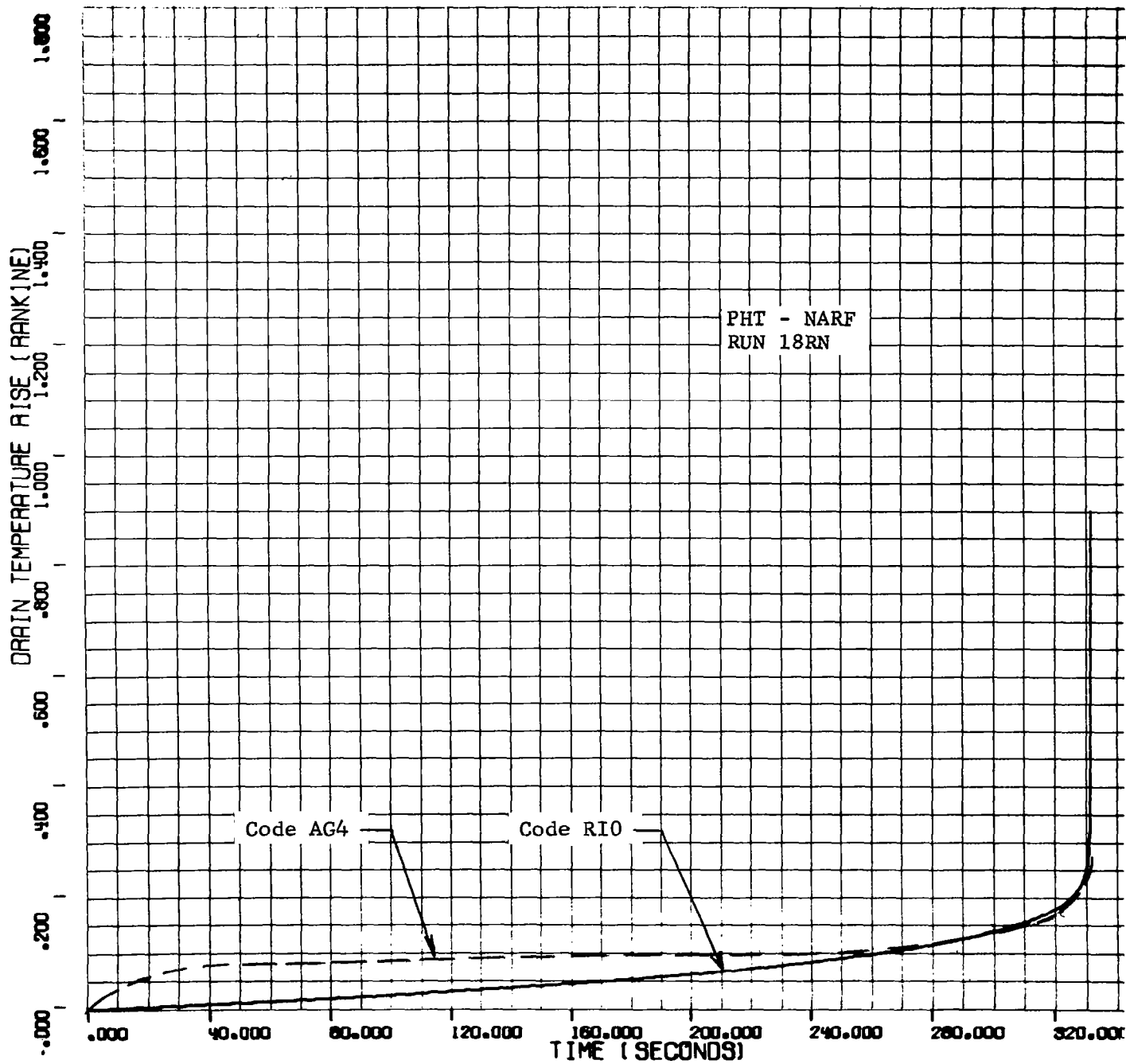
Figure 4-13   Comparison of Drain Temperature Profiles Calculated
               By Computer Codes RIO and AG4
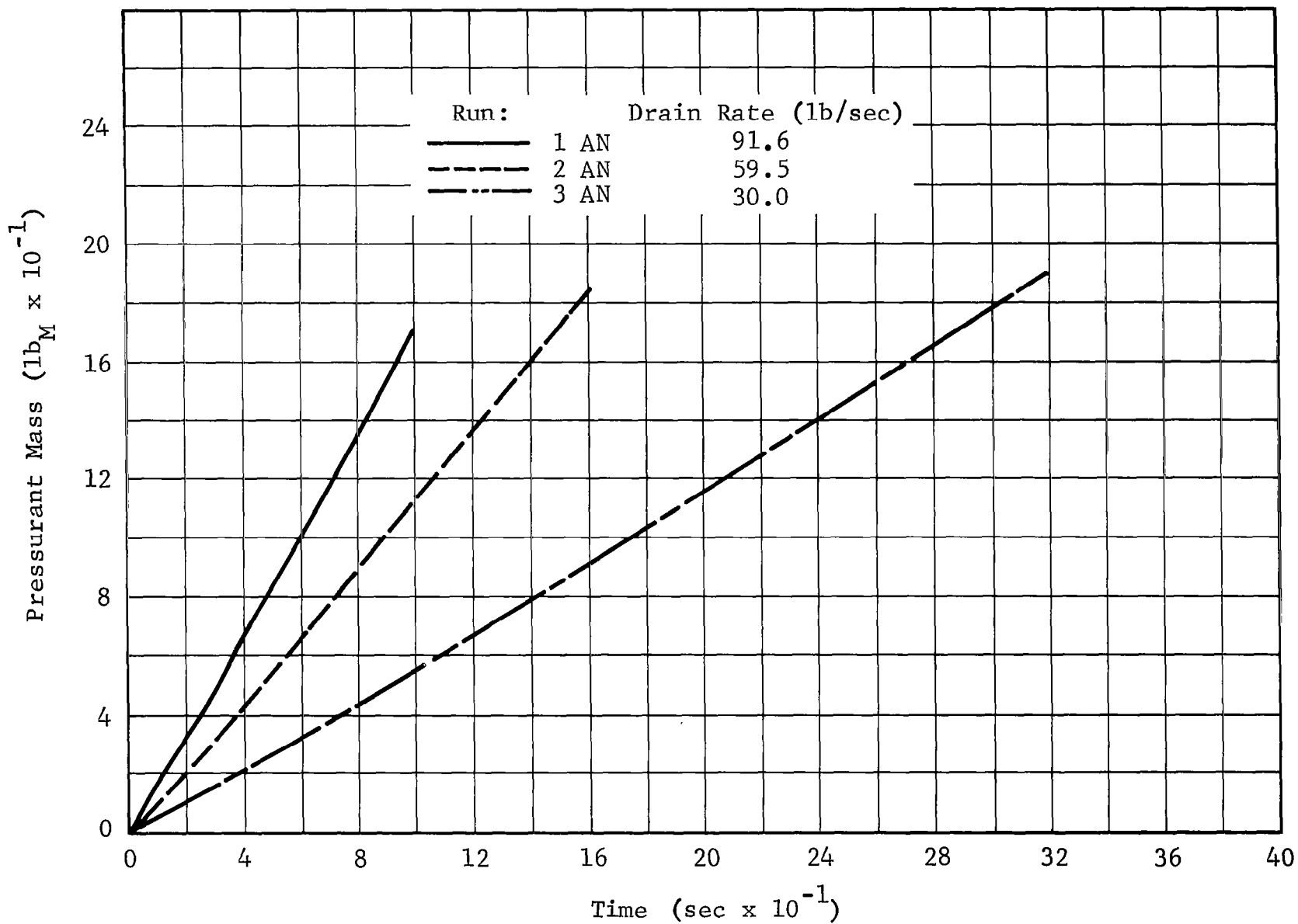
Figure 4-14   PHT Pressurant Requirements for Vent/Run Pressures
of 24/26.2 psia at 10-MW Reactor Power
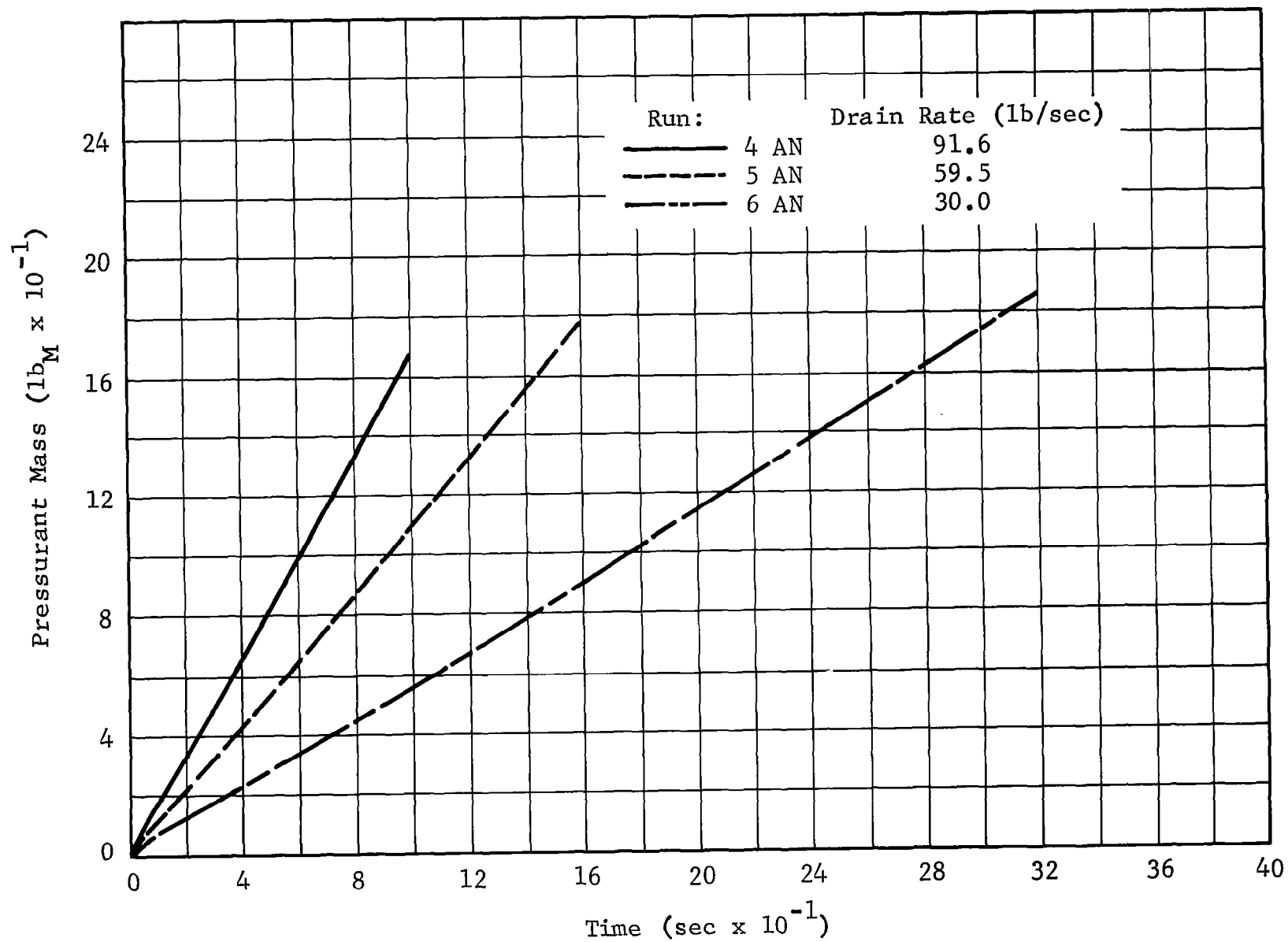
Figure 4-15   PHT Pressurant Requirements for Vent/Run Pressures
of 14.7/16.9 psia at 10-MW Reactor Power

4.2.5 Stratification and Destratification

Liquid hydrogen stored for long periods of time will depart from thermodynamic equilibrium due to thermal stratification. This will occur even under conditions of low acceleration and low sidewall heating. The impact of this phenomenon on tank design is that the pressure existing in a locked-up tank is dependent on the highest temperature of the fluid in the tank. A 1^oR temperature inequilibrium corresponds to a pressure rise of about 3 psi. Because tank weights depend on design pressures, methods to reduce or eliminate stratification hold promise of significant weight savings. Recent investigations (Ref. 15) of various destratification devices has shown the jet mixing concept to be promising. The PHT test provides an excellent opportunity to extend the experimental investigations of this destratification techniques to a large tank.

4.2.5.1 Stratification

Thermal stratification can be either passive or active. Natural heating effects can cause a temperature stratification to develop. Passive stratification can arise from the flow of heated liquid along the tank wall in a free-convection mode, resulting in the formation of a heated fluid layer at the ullage-liquid interface; also, high ullage heating can increase tank pressure and the surface temperature of the liquid. Active stratification results when a tank is pressurized.

Before stage firing, the tank is pressurized to collapse bubbles and to put bulk liquid in a subcooled state to satisfy pump NPSP requirements. Upon pressurization, the liquid at the interface immediately rises to the saturation temperature corresponding to the applied pressure.

Calculations of the PHT stratification based on techniques presented in Reference 14 indicate that passive stratification levels of 0.2° to $5^\circ R$ may be expected over the range of side-wall heating rates possible.

In general the passive stratification in the PHT will be characterized by fairly small temperature rises and large stratified layer depths. Therefore, experimentally, accurate temperature measurements will be necessary for valid stratification data.

Active stratification resulting from active tank pressurization during drain was predicted using code RIO. The results indicate that a very sharp temperature gradient can develop during drain. The stratified layer growth rates are low enough that the temperature profile in the layer(s) can be determined as it passes a fixed temperature sensor. The sensor should be capable of response to temperature changes of the order of $50^\circ R/sec$ for the highest drain rate (91.6 lb/sec) and $5^\circ R/sec$ for a drain rate of 15 lb/sec.

4.2.5.2 Destratification

The destratification requirements for the PHT using an axial jet were predicted using the techniques described in Reference 15. The results of the study indicate that the maximum pump flow required is about 2 lb/sec and the maximum fluid power is less than 5 watts. These results are similar to those predicted previously (Ref. 1).

It should be noted that since the use of the destratification pump during drain is expected to increase pressurization requirements, PHT data should be collected on this effect.

4.2.6 Pressurization and Ullage

Although there is a wealth of information available on pressurization phenomena, the Propellant Heating Test offers an opportunity to provide, with relatively little expenditure of effort, some additional data regarding pressurant requirements and pressure behavior during active pressurization. In addition, data can be obtained on the ullage parameters that effect ullage stratification and, therefore, self-pressurization.

The effects of active pressurization and pressurization level on the tank thermodynamics and fluid dynamics have been previously discussed in Subsection 3.3.6 for the RNS and Subsection 4.2.4 for the PHT, and thus are not included here.

4.3 Experimental Equipment

The experimental configuration shown in Figure 4-7 and discussed in this section was designed to be compatible with the existing ASTR facility; it provides the necessary flexibility for variation in nuclear and thermodynamic parameters. Some details of the facility construction such as the blast shield, thimble, and aluminum reactor window are presented.

4.3.1 Reactor Facility

The reactor facility, as described here, includes the ASTR and safety equipment for protection of the facility. The safety equipment includes the hydrogen-gas detection system, closed-circuit television monitoring systems, blast shields, and biological shields. The ASTR facility is shown in Figure 4-16.

4.3.1.1 The Aerospace Systems Test Reactor

The ASTR is a self-contained, pressurized nuclear reactor located in a below-grade-level tank with the necessary apparatus to position it in various attitudes. It is a heterogeneous, enriched, light-water moderated and cooled thermal reactor which operates over a design power range of 0 to 10 MW in support of radiation effects testing and shielding experiments. The design is roughly that of a right-circular cylinder 76 in. in length and 34 in. in diameter.

WATER SHIELD
TANK

LH$_2$ SUPPLY
TANK

FACILITY
SHIELD

The ASTR tank is 17.5 ft in diameter and 17 ft deep, 16.5 ft of which is below grade level. The top of the tank is flanged to accept a variety of upper-tank configurations. One such configuration is a short tank section that extends the top of the ASTR tank to a height of approximately 3 ft above grade.

On one side of the reactor is a void, or "window," which provides a direct-beam path from the core to increase the flux available from the reactor. Normally, the window on the ASTR consists of a water-tight air void constructed of sheet aluminum. This void is to be replaced with a solid-aluminum window to provide additional protection for the reactor.

A shield constructed of 2-in.-thick steel slab will be inserted between the ASTR and the test tank, for some tests, in order to increase the n/γ ratio of the radiation incident on the test tank. The shield can also be used as additional biological protection for personnel if it becomes necessary to work near the bottom of the test tank during reactor shutdown periods. When the shield is not in use, it will be positioned near the wall of the ASTR Tank where it will not interfere with lowering or raising the reactor.

4.3.1.2 Biological Shield

The biological shield consists of two parts called the facility shield and the water-tank shield (Fig. 4-7). It will serve two purposes: (1) to contain any conceivable blast that

4-35

could occur, and (2) reduce the radiation level around the facility.

Facility Shield. The facility shield, or silo, is constructed around the periphery of the ASTR tank as a 3-ft-thick cylindrical structure that is 19 ft high with an inner diameter of 26 ft. There are three penetrations in the silo: one door, 12 ft wide and 10.5 ft high, and two 18-in.-i.d. pipes. The lowest point of these penetrations is 3 ft above grade so that the silo will have a leak-free volume greater than the volume of the PHT tank.

When the door is closed it will be secured in place by four vertical hinge pins, one at each inside and outside edge. The size of these pins and the method of their attachment are such that the door will withstand the stress calculated for the maximum hypothetical hydrogen explosion. To open the door, three of the pins are removed, and the door, supported by a caster, pivots outward.

An air duct connected to a 5,000-cfm blower will be routed through one of the 18-in. penetrations. This blower will be used to flush the volume around the lower portion of the hydrogen tank. The other penetration will be used for the LH_2 fill and drain line. All other lines and electrical leads to the test tank will be routed over the top of the silo wall.

Safety devices incorporated in the silo include a CO_2 fire extinguishing system and a water spray system. Plumbing for twelve CO_2 exhaust nozzles and twelve water spray nozzles is embedded in the concrete near the top of the wall. Water and CO_2 nozzles are placed alternately at equal spacings around the wall. The CO_2 nozzles will be connected to dual banks of CO_2 bottles outside the silo. The water nozzles will be connected through a solenoid-operated pneumatic valve to a fire hydrant. Both systems will be operated from the control room.

Water Shield Tank. The silo is covered by a water shield 40 ft in diameter and 3.5 ft deep. The diameter of this shield is larger than that of the silo to prevent direct streaming of radiation from the silo.

The water shield tank has a capacity of 32,850 gallons. Since this tank must be set aside when moving large test items into or out of the silo, the tank has a drain valve and a single-point-pickup lifting eye.

The tank is supported 9 ft above the silo by legs resting in positioning holes in the top of the silo. The bottom of the tank is high enough (28 ft above grade) to accommodate the modular test tank. The 9-ft space between the silo and water shield tank will be open; thus, the silo will have a vent area of approximately 275 square feet.

4.3.1.3 Reactor Protection Shield

A paramount consideration in all reactor test configurations is that the reactor must be protected against damage that could possibly result from an accident with the experiment. For the PHT, reactor protection will be provided by a structure called the spider webb (Fig. 4-17). This structure will physically support the test tank with its associated plumbing. The design criteria were a static load of 18,000 lb and a safety factor of 2.5 times the static load.

The main frame of the spider webb consists of steel I-beams arranged in a 12-ft square with a diagonal brace in each corner. The frame is supported above the 3-ft ASTR-tank extension by a 12-ton jackscrew at each corner. Eight equally spaced I-beams are inclined downward and inward from the main frame and diagonal braces to a 75-in.-diam bottom plate having a 32-in.-diam hole in the center. With the reactor raised to the irradiation position, this hole is directly over the reactor window. The eight inclined I-beams are laced with six equally spaced steel cables to form, in essence, a conical spider webb above the reactor. Materials used in construction of the spider webb are:

```
Main frame I-beams:  12-in. x 12-in. WF 79, 1018 steel
Inclined I-beams:  8-in. x 5½-in. WF20, 1018 steel
Bottom plate:  1½-in.-thick 1018 steel plate
Lacing Cables:  5/8-in.-diam 18-8 stainless steel
```
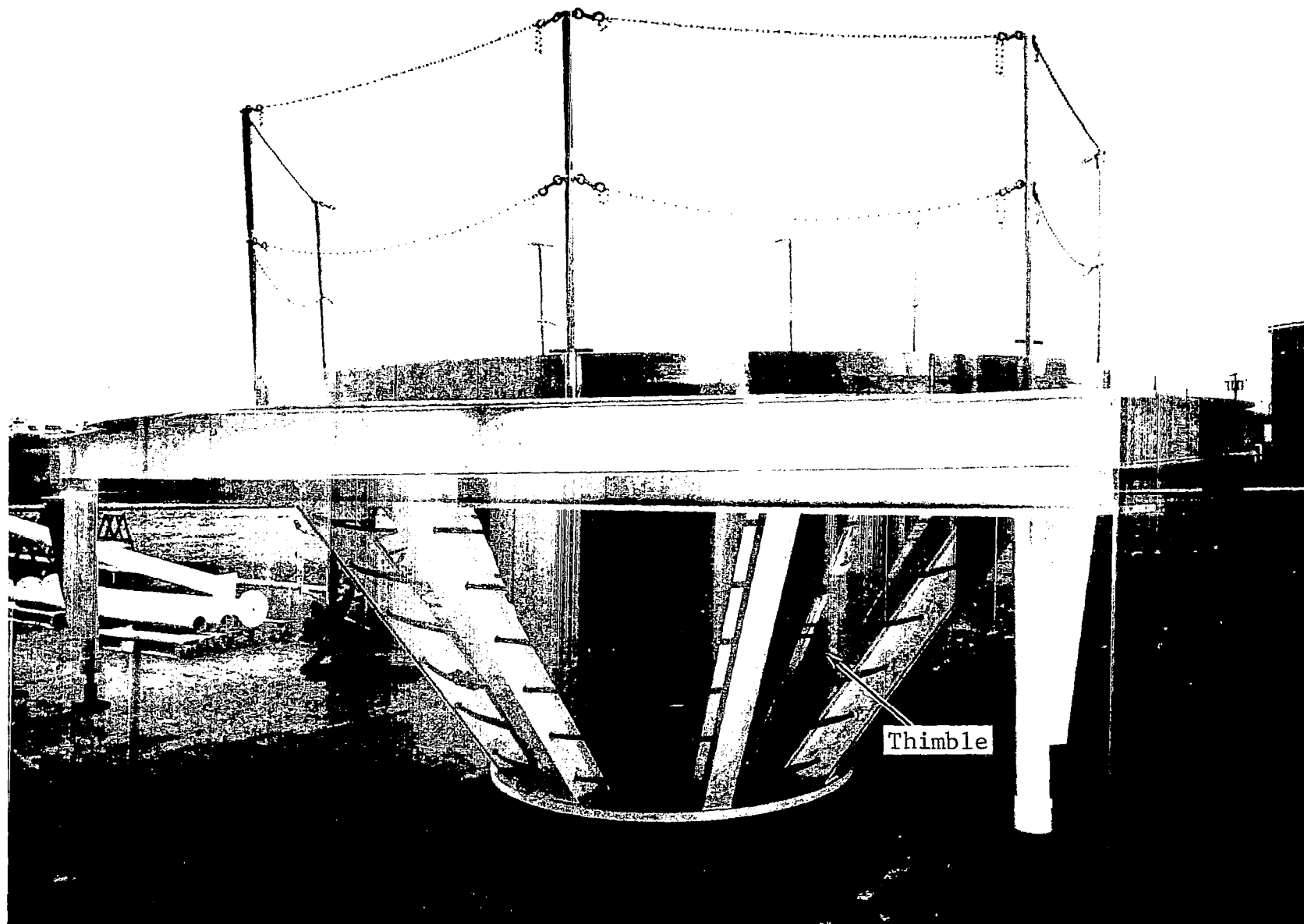
Figure 4-17 Spider Web and Thimble

4.3.1.4 Thimble

The thimble is a conical-shaped water retainer which nests within the envelope of the spider webb vertical structure (Fig. 4-17). The lower (small) end terminates at the opening in the circular base of the webb. This location coincides with the aluminum void on the ASTR and provides the shortest flux leakage path into the irradiation volume created by the thimble.

The thimble is a water-tight welded aluminum structure supported by flanges at its upper (large) end which are secured to the spider webb upper structure. Adequate clearance between the thimble and the test tank is provided for all required liquid-hydrogen lines and instrumentation cables.

The facility will be purged with air directed into the thimble around the test tank to ensure maximum air flow in the vicinity of the tank penetration. This purge is to assist in diffusion and dilution of any hydrogen should leaks occur in this area.

4.3.1.5 Hydrogen-Gas Detection System

In the event a leak should develop during the irradiation phase of an experiment, it will be detected by a General Monitor's Gas Detection System. This system contains fifteen individual channels each of which is calibrated to provide a visual and audible alarm should the concentration of hydrogen reach 10% of the lower explosive limit (LEL).

The sensing heads will be placed at those locations where a leak would most likely occur and at locations where escaping hydrogen gas could possibly accumulate. Typical locations would be at liquid-line and valve fittings, pumps, shroud-purge flow exits, and system exhaust plumbing. Provisions for sampling the test tank exhaust gas will be provided to verify the absence of hydrogen after the completion of the emptying and purge cycle. Detectors will be located at the upper portion of the silo, where the silo purge air will be exhausted. Redundant detectors will be utilized at critical points.

4.3.1.6 <u>Facility-Television Monitoring System</u>

Area and test equipment surveillance will be accomplished by closed-circuit television. Six remotely operable cameras complete with pan and tilt capabilities will be utilized. Three cameras will be mounted within the silo and three external to the silo.

Specific items to be viewed by the external cameras will be the hydrogen supply tank, the gas distribution and supply network, and the liquid hydrogen pump and flow control valves. The areas adjacent to these items, including the silo exterior and the gaseous hydrogen exhaust system, will also be scanned by the cameras. Their placement will be such as to allow overlapping coverage, where feasible, to provide maximum redundancy.

The cameras located within the silo will be placed for maximum overlapping coverage of the tank, fittings, and test structure.

The camera control system allows instantaneous selection of any three cameras for visual monitoring. The monitors are located in the Radiation Effects Control Console within the control room. Backup monitors located in the Reactors Consoles can simultaneously monitor any camera being monitored at the other console.

Any camera can be selected for recording on video tape. During irradiations and/or liquid-hydrogen operations, one of the cameras inside the silo will be continuously recorded.

4.3.2 Instrumentation

The instrumentation for the PHT must fulfill the objective of providing data for use in evaluating the computer codes used in predicting the drain-temperature profiles (Sec. IV). This requirement establishes the number and location of measurements and their accuracy for radiation levels, tank pressure, fluid temperature, flow rate, and level. The following sections present short discussions on these measurements.

4.3.2.1 Nuclear Measurements

Nuclear measurements are required inside and outside of the hydrogen tank for purposes of determining the radiation intensity at the bottom of the tank, in the liquid hydrogen, and

around the tank, and for monitoring reactor power level. Measurement of the radiation incident on the hydrogen tank and the distribution of radiation levels within the liquid hydrogen are necessary to the analysis of the experimental results since they will provide the nuclear-heating profiles required as input to the thermodynamic calculational procedures. The nuclear measurements will also be used in the evaluation of the procedures for calculating the radiation attenuation and energy-deposition rates in hydrogen. The results of the detailed study presented in FZK-350 (Ref. 1) were analyzed and found to be still valid for this test. That report should be consulted for a complete discussion of the measurement procedures.

4.3.2.2 <u>Thermodynamic and Fluid Dynamic Measurements</u>

The different measurements necessary for the experimental analysis of propellant heating include pressure, temperature, flow, and liquid level. The techniques of measurement selected and analyzed in the previous study (Ref. 1) have been reviewed as to their desired accuracy and range. It was found that in general all data are still valid although slight changes will have to be made when a final PHT tank configuration is chosen.

4.3.2.3 <u>Visual Coverage</u>

The television and photographic coverage requirements including tank lighting determined in the previous design effort were reviewed. It was found that the present PHT facility

would impose no additional or more sever requirements than those given in Reference 1. A typical man-hole-cover mounted camera arrangement is shown in Figure 4-18.

4.3.2.4 <u>Data-Acquisition System</u>

Temperature measurements associated with the fill, drain, and stratification portions of the test require that the data-acquisition system have a high repetition rate so that each measurement can be repeated at least twice per second. The number of measurements and their accuracy dictates that the system be digital; this will also allow direct reduction of the data by use of the IBM 360 computer.

Based on these considerations and others, the following requirements for a data-acquisition system have been established:

```
Type of system:  Digital
Minimum No. of Channels:  120
Minimum Speed:  200 channels/sec
Display per channel (or per sweep):  Time, channel ID,
    four decimal digits, polarity sign
Inputs:  Low-level dc analog signals from unbalanced
    bridges and thermocouples
Sensitivity:  0.5 microvolt
Output:  Digital on magnetic tape (compatible with 360
    computer)
```

At the present time, the NARF facility at General Dynamics does not have a system which meets all these requirements. One system which meets all these requirements is made by Trans Sonics and has been delivered to MSFC. It is a 120-channel digital system with a speed of 20 complete sweeps through the 120 channels
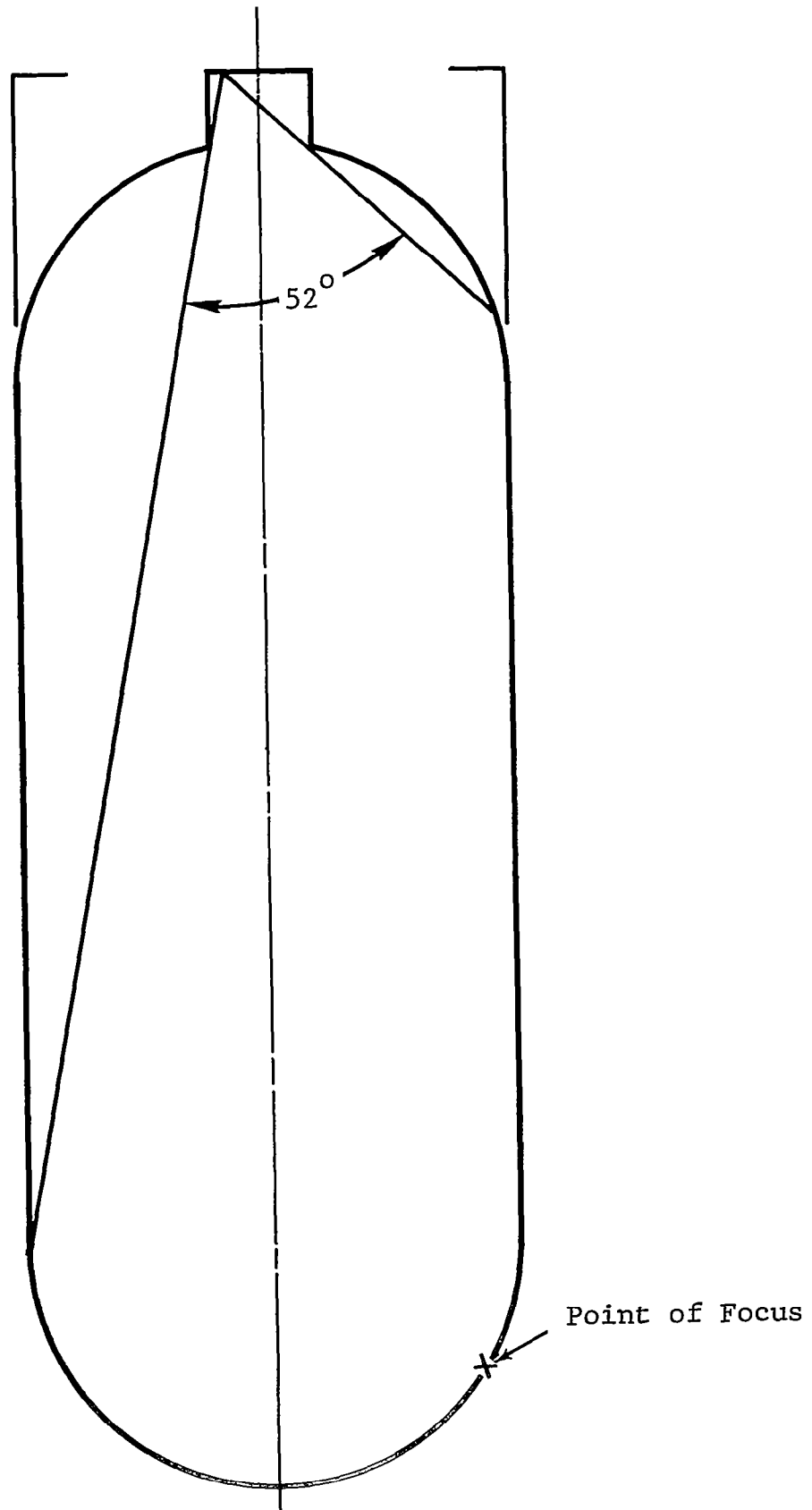
Figure 4-18   Camera Angle for Typical PHT Tank

in one second. Its present sensitivity is 5 microvolts, but modifications could increase the sensitivity to 0.5 microvolts; this would make it acceptable for use with thermocouples. It is a noise-free system which could easily be put into use for this test.

Visual monitors and auxiliary test equipment for other measurements will be furnished by General Dynamics.

4.4 Test Plan Synthesis

The test objectives and the various thermodynamic, fluid dynamic, and nuclear criteria that must be considered in the synthesis of a test plan are discussed below. Since four different RNS configurations are still being considered, no definitive test plan was formulated at this time.

4.4.1 Test Objectives

The primary objectives of the test are (1) to provide data that can be used to increase the confidence in the analytical techniques used to predict nuclear-energy deposition and the fluid thermodynamic effects resulting from the combined environments of ambient and nuclear heating, and (2) to provide data for design application through simulation and/or parametric testing.

The experiment being considered will not only fulfill the above objectives, but also will take maximum advantage of the test

facility capabilities and test sequencing to provide a maximum amount of data in a minimum number of runs. These data include, for instance, effects of pressurant gas and pressurant-gas temperature on stratification and pressurant-gas requirements, destratification parameters during both drain and non-drain periods, and the effect of nuclear heating on stratification under non-drain conditions as well as boundary-layer effects under similar conditions. In addition, data on the effect of internal structure on propellant heating and stratification will be provided for.

4.4.2 Thermodynamic and Fluid Dynamic Criteria

Based on the work accomplished, thermodynamic design criteria have been established for this experiment which, when applied along with the geometric similitude constraints, will yield a test plan designed to provide the maximum amount of applicable thermodynamic and fluid dynamic data. The primary criteria affecting the design of the test plan are: (1) the baseline or initial conditions for the test runs, for example, the bottom-to-side wall heat-flux ratio, (2) the range of variables required for design and simulation of a RNS, and (3) the range of variables required for evaluating the computer codes such as flow rate, nuclear heating, ambient heating, internal structure, etc.

The range of the important RNS and PHT simulation parameters were shown in Figures 4-1 through 4-4. An experiment

4-47

design based on these parameters will be capable of providing the design data required for any of the RNS configurations and missions now being considered.

4.4.3 Nuclear Criteria

The nuclear criteria for the experiment are to (1) obtain data for the verification of computer procedures for calculating radiation attenuation and energy deposition in liquid hydrogen, and (2) simulate the nuclear environment of the NERVA to allow application of the experimental data to the design of RNS. Measurement of the radiation leaving the reactor and of the radiation incident on the test tank bottom will be made to determine the radiation source term for input to the computer procedures. The neutron flux and gamma-ray dose distributions inside the test tank will be measured for determination of the attenuation due to the liquid hydrogen. These data will also be used to calculate energy-deposition rates and profiles within the hydrogen. The bulk energy input into the tank and hydrogen will be determined with boiloff and self-pressurization measurements. These data will be a check on the nuclear-energy deposition rates determined from the nuclear radiation maps.

V. FLOW VISUALIZATION EXPERIMENT

A qualitative study of the fluid motion resulting from bottom and sidewall heat shorts was conducted for a conical bottom tank configuration using a schlieren flow visualization technique. The test equipment and results are discussed in the following subsections.

5.1 Test Equipment

The test equipment consisted of a single pass schlieren optical system and a clear plastic test tank. The test fluid, n-butyl alcohol, was chosen on the basis of its optical and thermophysical properties as well as its chemical compatibility with the plastic test tank.

5.1.1 Optical Arrangement

A schematic of the optical system used in the study is shown in Figure 5-1. The field of view of the system was a circular area 4 inches in diameter. This area was set by the lens diameter of the laser collimator (beam expander).

The image was recorded on film using a studio camera with the lens removed, thus allowing the image to fall directly on the film. The exposure time was controlled by the automatically timed and actuated camera shutter system.

The film used was Polaroid Type 52 (ASA 400). Exposure times with this film ranged from 1/10 to 1/50 second.

Beam
Steerer

Jodon Engineering Associates
15 Milliwatt Helium-Neon Laser

Mirror

Test Tank

Tropel Spatially
Filtered Laser
Collimator Model 280

Camera

Knife
Edge
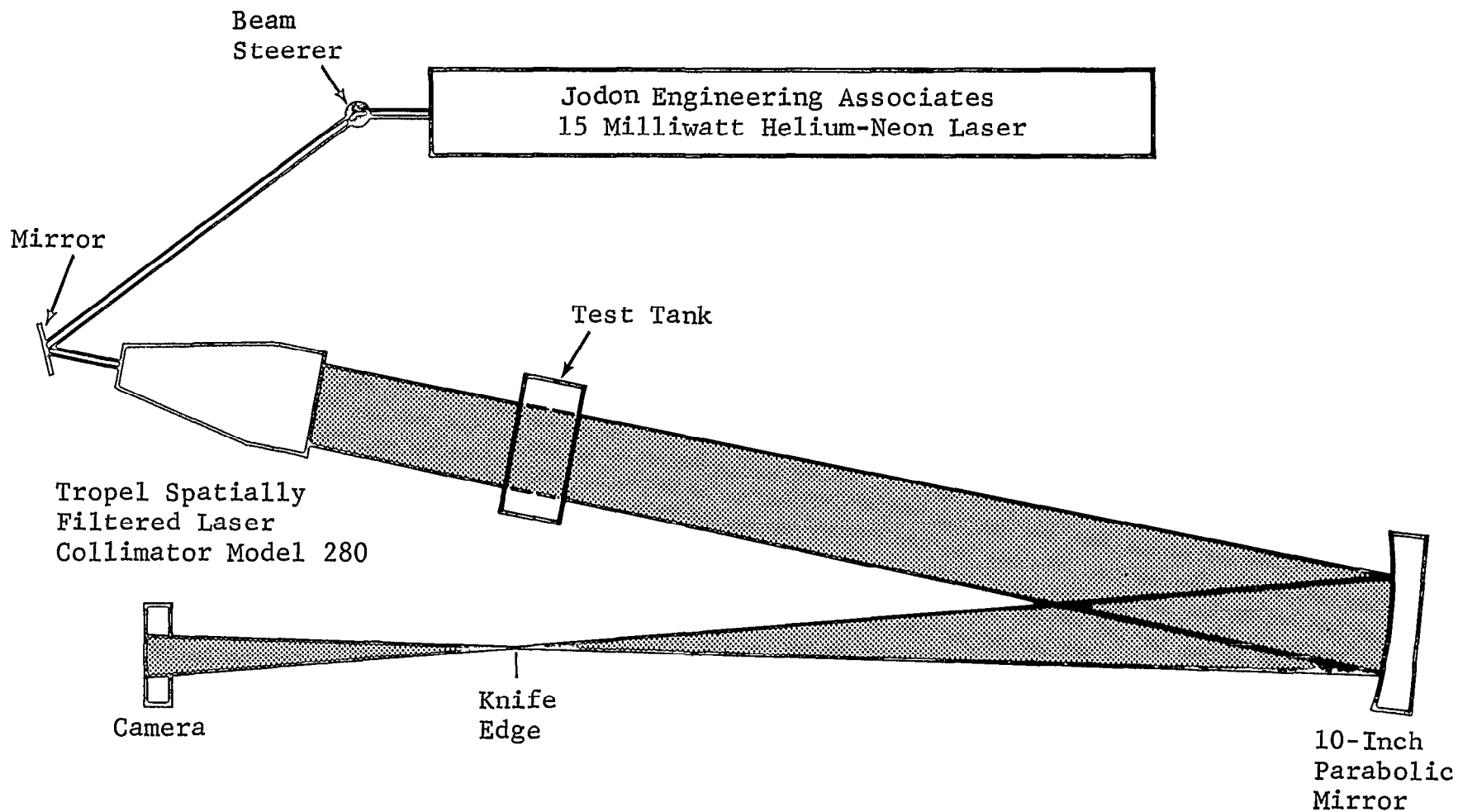
10-Inch
Parabolic
Mirror

Figure 5-1 Optical Arrangement for Single-Pass Schlieren Photograph

5.1.2 Test Tank

A side view of the two-dimensional test tank used is shown
in Figure 5-2. Tank side walls are 1-inch apart and are of
1/16 in.-thick material.

The tank was constructed from cast acrylic. This material
was used because it has good optical properties and is relatively
easy to fabricate. The heat shorts consisted of two 3/16-in.
brass bolts on the left side and one 1/4-in. copper tube on the
right side of the conical sidewalls. The drain heat short was
simulated by a 1/4-in. copper tube located in the middle of the
tank bottom. Heat to the ends of the heat shorts were provided
by electrical resistance wires.

5.2 Test Results

Approximately 12 hours of tests were conducted during which
the fluid motion resulting from various combinations of heat
transfer through the heat shorts was observed. Unfortunately,
on the day selected for photographing these phenomena the laser
tube stopped functioning and only three photographs were ob-
tained. Additional photographs were not made because replace-
ment of the laser tube was not possible within the time and cost
constraints of the program.

Figures 5-3 and 5-4 show the fluid motion in the test tank
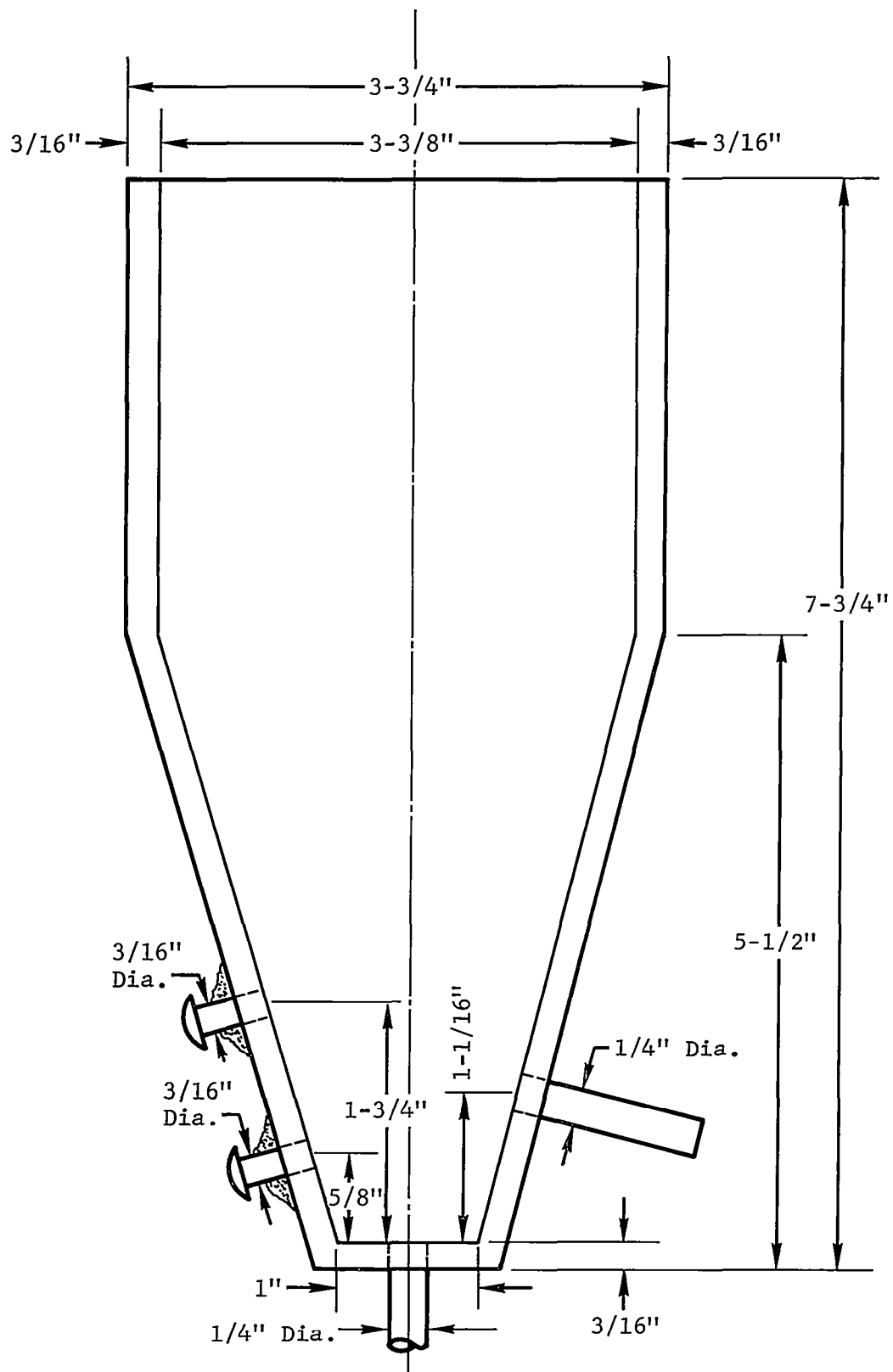under different heat leak conditions. In both cases the drain

Figure 5-2 Test Tank for Schlieren Photograph

(a) Time After Start of Heating: 30 Sec
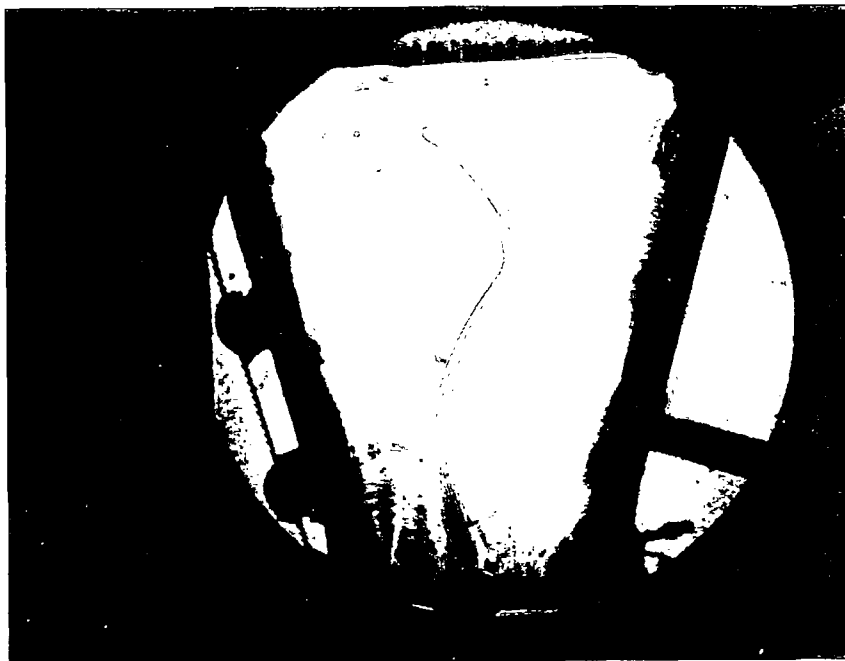
(b) Time After Start of Heating: 90 Sec

Figure 5-3   Schlieren Photographs Showing Flow Patterns
             Resulting from Major Drain Line Heating and
             Minor Nonuniform Heat Short Heating

Time After Start of Heating: 90 Sec

Figure 5-4   Schlieren Photograph Showing Flow Pattern
             Resulting from Minor Drain Line Heating and
             Major Nonuniform Heat Short Heating

line and sidewall heat shorts were the only source of heating, i.e., no sidewall or bulk (source) heating was present.

Figure 5-3 shows the formation of the fluid motion caused by a combination of drain pipe bottom heating and sidewall heat short heating and cooling. Fluid patterns photographed at two time intervals, namely, 30 and 90 seconds from the start of heating, are shown. For this case, the dominant feature of the fluid motion is caused by the drain line bottom heating -- a type of heating that could occur in a full-scale tank if the thermodynamic vent system failed to operate properly and did not absorb the heat flowing from the warm exterior components through the drain line to the liquid hydrogen. The fluid motion for this type of heating is characterized by a column of warm fluid flowing up the centerline of the tank. This column dissipates as it rises giving up its energy to the cooler sur-rounding bulk fluid. When it reaches the top, it starts forming a stratified layer. At later times as it reaches the stratified layer, it is deflected and dissipated adding to the stratified layer. The motion of the column as well as the deflection at the top was of an oscillatory nature. One can also see the den-sity change in the bulk fluid created by the warm column of fluid moving up through it. The drain line heat flux was calculated to be about 15 Btu/h-in.^{2}.

Also shown in this figure are the fluid motion effects of nonuniform heating or cooling of the liquid by the heat shorts located in the sidewalls of the conical portion of the tank. The right side heat short is cool compared to the liquid and, therefore, is causing a very slight boundary layer to form and proceed downward along the wall toward the bottom of the tank. This can be seen most clearly in the photograph taken at 30 seconds after start of heating. After 90 seconds, the bulk motion has destroyed this weak boundary layer flow and it appears that some type of mixed flow is occurring near the right wall. The heat flux flowing from the tank at this location was estimated to be less than 2 $Btu/h\text{-}in.^2$. The heat shorts in the left side of the conical portion of the tank were heated slightly during this run. The heat flux was estimated to be 5 $Btu/h\text{-}in.^2$ for the uppermost heat short and 2 $Btu/h\text{-}in.^2$ for the lower heat short. As was the case for the flow on the right side, the boundary-layer flow can be seen developing in a regular manner at 30 seconds, while at 90 seconds the flow is irregular and bulk mixing seems to be destroying the boundary layer flow.

Figure 5-4 shows the fluid motion resulting from very high heating on the right side heat short (30 $Btu/h\text{-}in.^2$), slight cooling on the left side heat shorts (about 2 $Btu/h\text{-}in.^2$), and drain line heating of 15 $Btu/h\text{-}in.^2$.

The high heat flux on the right side creates a very large turbulent boundary layer flow starting at the heat short and proceeding almost vertically up to the stratified layer. The momentum of this boundary layer flow is very high compared to the momentum of the warm column of fluid rising from the drain line heat short. This fact can be ascertained by comparing the depth to which the stratified layer is penetrated by the two flows. When comparing the depth of the stratified layers in Figures 5-3 and 5-4, it is found that the depth in Figure 5-4 is much greater. This is as it should be since much more energy is being added to the fluid through the heat shorts.

The slight cooling effect of the left side heat shorts produces a downward flowing boundary layer starting at the upper heat short location and flowing toward the bottom. This flow is similar to that shown in Figure 5-3 (left side heat short cooling). In the case at hand, however, the flow is much better defined after 90 seconds of heating than in the previous case (Fig. 5-3). This is probably caused by the general flow pattern within the tank being counterclockwise, that is, up the right side and down the left side. A good indication of this is the downward bulge of the stratified layer near the left sidewall.

In summary, it appears that, under the conditions studied, heat shorts can create some bulk mixing, particularly if the short is on the tank centerline and at the bottom of the tank.

In general however, it seems that the dominant trait is to produce a stratified layer, especially when the heat short is located in the sidewall.

VI. CONCLUSIONS AND RECOMMENDATIONS

6.1 Conclusions

From the analysis of the fluid dynamic and thermo-dynamic phenomena of liquid hydrogen propellant in typical RNS configurations in conjunction with a re-evaluation of the test plan developed previously, it is concluded that:

1. The ranges of the scaling groups obtainable in the PHT either encompass or extend over most of the range of the expected full-scale values of all RNS configurations studied (Figs. 4-1 to 4-4).

2. The wide range of conditions that can be obtained in the PHT will be significant in developing correlations from the test data.

3. One of the more important groups that effect the fluid dynamic and thermodynamic phenomena (stratification) within the propellant tank is the bottom-to-sidewall heat-flux ratio.

4. The bottom-to-sidewall heat-flux ratio can be varied in the PHT by using different reactor power levels.

5. The range of bottom-to-sidewall heat-flux ratios for typical RNS configurations lies within the range obtainable in the PHT (Fig. 4-1).

6. Both active and passive stratification under drain and nondrain conditions can be studied in the PHT.

7. The effect that nuclear heating of the internal structure has on the stratification is not well defined and must be studied further.

8. Since stratification under various conditions will already exist in the PHT, destratification experiments can be run with little additional effort.

9. The drain-temperature profiles predicted using computer codes RIO and AG4 are different, and experimental data are required to further refine and reconcile the analytical computer codes (Fig. 4-13).

10. Criteria for boundary-layer initiation and breakoff points are lacking and must be further developed before the fluid dynamics and thermo-dynamics of the RNS tanks can be accurately predicted, especially in tanks having conical bottoms with small cone half angles.

6.2 Recommendations

Based on the above conclusions it is recommended that:

1. A PHT tank configuration be chosen and final design accomplished with purchase of long lead time items.

2. The criteria for boundary-layer initiation and breakoff be studied and determined both ex-perimentally and analytically. These studies should as a minimum include wall angles and wall heat fluxes consistent with current RNS design parameters.

3. A time-phased test plan be developed allowing for extended-parameter testing of non-nuclear tank-related variables (e.g., pressurization, heat shorts, vent pressures) followed by nuclear irradiation testing.

4. Further studies be undertaken to define the effects that nuclear heating of internal struc-ture such as antivortex baffles, suction-dip devices, thermodynamic vent system components, and propellant retention screens has on the fluid dynamic and thermodynamic phenomena of the propellant.

APPENDIX A

DIMENSIONAL ANALYSIS AND SIMILARITY

A-1 INTRODUCTION

The fluid dynamic and thermodynamic behavior of the
liquid-hydrogen propellant of a nuclear rocket vehicle
before, during, and after engine firing is very complex as
a result of the changing environment. Elements of this
environment include propellant heating due to ambient and
nuclear sources, changes induced by tank venting and/or
propellant mixing, and changes due to acceleration. A
thorough understanding of the effects of these elements on
the propellant is necessary before system operating char-
acteristics can be accurately defined.

Analytical techniques are available for predicting or
estimating these effects (Reference 2-1 and 2-2). The results
of these techniques, however, have never been validated
experimentally for large-size tanks. Since it is both
difficult and expensive to do full-scale testing of either
the single tank or the complete hybrid RNS configurations,
ground test simulation employing the scale-model tests
provides an excellent means for obtaining the required data.

In the first part of this Appendix, the physical
situation is described and the various physical phenomena

A-1

and the effect each has on the fluid dynamic and thermodynamic behavior of the propellant are discussed. Also included is a discussion of ground rules for the modeling analysis. In the second part, the modeling techniques used to derive the scaling groups necessary for simulation are presented and the physical significance of each group is discussed.

A-2   DESCRIPTION OF PHYSICAL SITUATION

The first step in performing a modeling analysis is to define the physical situation as accurately as possible. For the case at hand, this means a description of the nuclear rocket vehicle and the particular system to be considered. The pertinent physical phenomena can then be determined and the ground rules for the scale model established.

A-2.1   NUCLEAR ROCKET VEHICLE - Typical RNS configurations are shown in the main body of this report (Figures 2-1 through 2-4). Likewise the thermodynamic, fluid dynamic and geometric variables of the RNS configurations are given in Table 3-1.

A-2.2   SYSTEM CONSIDERED - The system to be considered consists of a cylindrical tank with either hemispherical, elliptical, or conical ends. Liquid hydrogen is the propellant. The event under consideration is that of stage firing during space flight.

A-2.3 PROPELLANT PHENOMENA - In the system being considered the liquid-hydrogen propellant is subjected to various drain rates and modes of heating and pressurization.

During the coast phase of the mission, energy enters the propellant by conduction through the tank wall. This creates a natural-convection boundary layer in the liquid hydrogen along the tank wall. The boundary layer transports warm fluid to the top of the tank where it forms a stratified surface layer and, hence, an axial temperature gradient. The magnitude of this gradient is an indication of the deviation from thermal equilibrium in the propellant.

During engine firing the most significant phenomena occur in the lower portion of the tank. Close to the bottom, near the tank outlet, the forced-convection currents created by the draining fluid can be sufficiently strong to destroy the natural-convection boundary layer. If this were the only phenomenon occurring, it would stop the boundary-layer transport of warm fluid from the bottom of the tank. However, the tank wall heat flux will increase because of direct deposition of nuclear energy within the wall, and this will counter the effect of the forced-convection currents. In addition, significant quantities of nuclear energy will also be deposited in the bulk fluid.

This will create a buoyant force in the bulk or core of the fluid, and this force will act counter to the inertia forces of the draining fluid. It is possible for these phenomena to create a temperature inversion wherein the fluid would be warm at the bottom, cool in the bulk, and warm at the top.

It is important to understand the above phenomena because their effect on RNS system design is significant. For example, if a large layer of warm propellant exists at the time of firing and the vapor pressure corresponding to its temperature exceeds the net positive suction head requirements of the pump, pumping action will stop when this fluid reaches the pump and the remaining propellant will be unused. Also, if stratification occurs during coast, the tank must be designed for higher pressures or be vented more frequently.

A-2.4 MODELING GROUND RULES - Exact duplication of all relevant system variables in a scaled test will ensure duplication of full-scale physical phenomena and the applicability of the results. This is, however, impossible in the case under consideration because of the complex nature of the problem and the number of variables involved. Thus it is necessary to base the modeling laws on duplication of scaling groups associated with those physical phenomena felt to be dominant.

Extremes of test conditions should also be run to generate data that will be useful in case the selection of the scaling groups is not optimum. This wide range of test conditions will ensure that the data will be applicable even if the configuration of the RNS is changed.

A-3 MODELING TECHNIQUES

One method of obtaining pertinent dimensionless parameters is that of normalization of the equations governing the physical phenomena. This method is quite straightforward but requires a valid mathematical model. To normalize the equations requires two steps: (1) make all variables nondimensional in terms of the appropriate scale of the problem and (2) divide through the equation by the coefficient of one term to make the equation dimensionless, term by term.

A second method is dimensional analysis. This method is concerned with the manner in which the relationship between primary dimensions implies a relationship between the physical parameters ascribed to those dimensions. The Pi Theorem is a formal statement of the connection between a function expressed in terms of physical parameters and a related function expressed in terms of nondimensional groups (References 3 through 6). Given a relationship among m parameters,

$$f_1 (q_1, q_2, q_3, \ldots, q_m) = 0 \qquad (1)$$

an equivalent relationship can be expressed in terms of n

nondimensional parameters

$$f_2 (\Pi_1, \Pi_2, \Pi_3, \ldots, \Pi_{\dot{n}}) = 0 \qquad (2)$$

where n is given by

$$n = m - k \qquad (3)$$

and k is the minimum number of primary dimensions, e.g.,

mass, length, time, and temperature, used to construct the

original set of physical parameters.

A-3.1 NORMALIZATION OF GOVERNING EQUATIONS - Normalization

of the governing equations to develop a set of scaling

parameters requires sufficient understanding of the physi-

cal phenomena to write a valid mathematical model.

A-3.1.1 <u>Definition of Mathematical Model</u> - A mathematical

model of the problem at hand consists of the Navier-Stokes

equation, the boundary-layer energy equation (both written

in cylindrical coordinates), and an overall energy balance.

The following assumptions are made:

1. Changes in the θ direction are negligible

2. Only the liquid is considered

3. Density is a function of temperature only

4. Viscosity is constant.

The following equations then result:

Vertical Momentum

$$\rho\left(\frac{\partial u}{\partial t} + u\frac{\partial u}{\partial x} + v\frac{\partial u}{\partial r}\right) = -\rho g - \frac{\partial P}{\partial x} + \mu\left(\frac{\partial^2 u}{\partial x^2} + \frac{1}{r}\frac{\partial u}{\partial r} + \frac{\partial^2 u}{\partial r^2}\right) \quad (4)$$

Radial Momentum

$$\rho\left(\frac{\partial v}{\partial t} + u\frac{\partial v}{\partial x} + v\frac{\partial v}{\partial r}\right) = -\frac{\partial P}{\partial r} + \mu\left(\frac{\partial^2 v}{\partial x^2} + \frac{1}{r}\frac{\partial v}{\partial r} - \frac{v}{r^2} + \frac{\partial^2 v}{\partial r^2}\right) \quad (5)$$

Energy

$$\frac{\partial T}{\partial t} + u\frac{\partial T}{\partial x} + v\frac{\partial T}{\partial r} = \alpha\left(\frac{\partial^2 T}{\partial x^2} + \frac{1}{r}\frac{\partial T}{\partial r} + \frac{\partial^2 T}{\partial r^2}\right) \quad (6)$$

Continuity

$$\frac{\partial u}{\partial x} + \frac{\partial v}{\partial r} = 0 \quad (7)$$

Overall Energy Balance

$$\frac{\partial}{\partial t}\left[Mc_p(T-T_i)\right] = q_w A_w + q_b A_b - \dot{w}\, c_p(T-T_i) \quad (8)$$

Variation in Density

$$\rho = \rho_o\left[1 - \beta(T-T_o)\right] \quad (9)$$

A-3.1.2 <u>Normalization Procedure</u> - The normalization procedure

will be demonstrated by use of the energy equation, with

the work on the remaining equations performed in Section

A-4.

The normalization parameters used are given in Table

A-1 (p. A-20). Substituting these values into the energy

equation yields

A-7

$$\frac{\partial \overline{T}}{\partial \theta} \frac{(T_s - T_i)\, \nu}{H_o{}^2} + \frac{\dot{w}(T_s - T_i)}{\rho\, D^2\, H_o} \,\overline{u}\, \frac{\partial \overline{T}}{\partial \overline{x}} + \frac{\dot{w}(T_s - T_i)}{\rho\, D^3} \,\overline{v}\, \frac{\partial \overline{T}}{\partial \overline{r}} \;=$$

$$\frac{\alpha(T_s - T_i)}{D^2} \left(\frac{D^2}{H_o{}^2} \frac{\partial^2 \overline{T}}{\partial \overline{x}^2} + \frac{1}{\overline{r}} \frac{\partial \overline{T}}{\partial \overline{r}} + \frac{\partial^2 \overline{T}}{\partial \overline{r}^2} \right) \qquad (10)$$

Dividing through by $\dfrac{\dot{w}(T_s - T_i)}{\rho\, D^3}$, the coefficient of $\overline{v}\,\dfrac{\partial \overline{T}}{\partial \overline{r}}$,
results in

$$\left[\frac{\rho D^3 \nu}{\dot{w}\, H_o{}^2}\right] \frac{\partial \overline{T}}{\partial \theta} + \frac{D}{H_o} \,\overline{u}\, \frac{\partial \overline{T}}{\partial \overline{x}} + \overline{v}\, \frac{\partial \overline{T}}{\partial \overline{r}} = \frac{\rho D \alpha}{\dot{w}} \left(\frac{D^2}{H_o{}^2} \frac{\partial^2 \overline{T}}{\partial^2 \overline{x}} + \frac{1}{\overline{r}} \frac{\partial \overline{T}}{\partial \overline{r}} + \frac{\partial \overline{T}}{\partial \overline{r}^2} \right) \quad (11)$$

This equation yields three groups:

(1) $\dfrac{D}{H_o}$ \qquad (2) $\dfrac{\rho D^3 \nu}{\dot{w}\, H_o{}^2} = \left(\dfrac{\rho D \nu}{\dot{w}}\right)\!\left(\dfrac{D^2}{H_o{}^2}\right)$ \qquad (3) $\dfrac{\rho D \alpha}{\dot{w}} = \left(\dfrac{\rho D \nu}{\dot{w}}\right)\!\left(\dfrac{\alpha}{\nu}\right)$

From the normalization of the momentum and overall energy
equation and listing of the normalization parameters for
the basic dimension length, time, and temperature, the di-
mensionless scaling groups in Table A-2 (p. A-21) are derived.

A-3.2 PI THEOREM - The Pi Theorem can be applied to the same
problem without the need of a mathematical model. This
method is more mechanical in nature but requires significant
insight into the problem to determine all the pertinent
variables.

A-3.2.1 Definition of Variables - The starting point for the
Pi Theorem dimensional analysis is the determination of the
physical variables to be used. Fifteen variables were

determined to be pertinent to the problem at hand. These variables were determined assuming no ullage-liquid interactions and then considering the individual phenomena involved. The variables are defined in Table A-3 (p. A-22); their relationship to the tank is shown in Figure A-1 (p. A-24), where convenient.

A-3.2.2 <u>Pi Group Development</u> - Four basic dimensions - mass (M), length (L), time (θ), and temperature (T) - are necessary to express these fifteen variables. According to the Pi Theorem, these fifteen variables may be combined to form 15-4 = 11 dimensionless groups.

The number of Πs being known, the next step is to formulate explicitly a set of independent Πs. One method is to find an arbitrary group of parameters that does not form a dimensionless product, for example, q_w, H_o, T_s-T_i, ν and ρ. The selection of this group in reality is not completely arbitrary since consideration is given to obtaining terms convenient for nondimensionalization and terms which should appear in expected groups, e.g., the Reynolds number. For convenience, a fifth basic dimension, the Btu (H), is defined, allowing five equations in five unknowns to be used for the solution of the exponents of the variables in the various nondimensional groups. An example of the formation of one Π grouping is given below; the derivation of a

A-9

complete set of Πs is given in Section A-4:

$$\Pi_1 = \frac{X}{q_w^{a_1} H_o^{b_1} (T_s - T_i)^{c_1} \nu^{d_1} \rho^{e_1}} \qquad (12)$$

The parameters of the denominator have the dimensions of

$$\left[H^1 \theta^{-1} L^{-2} \right]^{a_1} \left[L \right]^{b_1} \left[T \right]^{c_1} \left[L^2 \theta^{-1} \right]^{d_1} \left[M^1 L^{-3} \right]^{e_1}$$

The numerator has the dimension of L^1. Five equations in

the five unknowns can now be written.

For H, $\quad a_1 = 0$ $\hfill (13)$

For T, $\quad c_1 = 0$ $\hfill (14)$

For M, $\quad e_1 = 0$ $\hfill (15)$

For L, $\quad -2a_1 + b_1 + 2d_1 - 3e_1 = 1$ $\hfill (16)$

For θ, $\quad -a_1 - d_1 = 0$ $\hfill (17)$

Solving for the unknowns,

$$a_1 = 0 \qquad\qquad d_1 = 0$$

$$b_1 = 1 \qquad\qquad e_1 = 0$$

$$c_1 = 0$$

$$\Pi_1 = \frac{X}{q_w^o H_o^1 (T_s - T_i)^o \nu^o \rho^o} = \frac{X}{H_o} \qquad (12)$$

Continuing the above procedure, the set of Πs given in

Table A-4 (p. A-23) are developed.

A-3.2.3 _Scaling Group Development_ – The relative importance of

the dimensionless groups and the ways in which they can be

combined to give more easily recognizable groups occur from an extension of dimensional analysis commonly called similitude analysis. For example, when the natural-convection boundary layer is considered, a knowledge of the physical phenomena indicates interest in simulating the ratio of the buoyancy force to the viscous force. This leads to the observation that Π_7 should be combined with Π_{11} to form what is commonly called the Grashof number $g\,\beta\,(T_s - T_i)\,x^3/\nu^2$.

In like manner, the combination of Π_8 and Π_9 yields $\rho\nu c_p/k$, which is the ratio of the momentum diffusivity to the thermal diffusitivity and is known as the Prandtl number. The ratio of the inertial force to the gravitational force is obtained by combining $(\Pi_6)^2$ and Π_7. This ratio is known as the Froude number. From the overall energy balance standpoint a dimensionless bulk temperature rise is of interest. This can be obtained by combining Π_6 and Π_8. From an experimental standpoint it is easier to work with wall heat flux than with temperature difference; therefore, the modified Grashof number $g\,\beta\,q_w\,H_0^4/k\nu^2$ is used in place of the Grashof number. The results of this analysis yield the same dimensionless groups as obtained from the normalization of the governing equations (see Table A-2) with the addition of the group $\beta\,(T_s - T_i)$.

There are now eleven scaling parameters. N_1, N_2, N_3

A-11

are nondimensional distance, time, and temperature, respectively. If only drain temperature is considered, $N_1 = 0$. N_4 involves geometric similarity. N_5 is a relationship between heat inputs reaching the stratified layer and heat inputs deposited in the bulk. N_6 is a Reynold's number for the entire draining tank. N_7 is the Grashof number, important to free-convection flow. N_8 relates to nondimensional bulk temperature rise. N_9 is important to tank outflow conditions. N_{10} is the Prandtl number of the liquid. N_{11}, $\beta(T_s - T_i)$, is a measure of the liquid expansion effects and an indication of the errors resulting from the use of a constant ρ; the importance of this group is believed to be minimal for low $T_s - T_i$ values, and the important effect of β is included in the modified Grashof number.

An experimental test program can now be developed by the use of these scaling parameters. Values of the physical parameters for the full-scale RNS are substituted into the nondimensional groups to determine the explicit values to be used in designing the scaled test.

Existing facilities as well as the choice of test fluid will also influence the experiment design. For example, the choice of liquid hydrogen (based on nuclear radiation attenuation considerations) restricts the range of those groups containing physical property parameters.

A-12

A-4 NORMALIZATION AND DIMENSIONAL ANALYSIS DETAILS

The governing equations which comprise the mathematical model are given by Equations 4 to 9. Normalization of these equations provides 10 scaling parameters, which are listed in Table A-2. The detailed derivation of these groups is presented below. The normalization parameters used are given in Table A-1.

Taking the vertical momentum equation (Eq. 4) and substituting Equation 9 and the appropriate values for u, v, x, r, and P from Table A-1, the following equation results:

$$\rho\left[\frac{\partial\overline{u}}{\partial\overline{t}}\left(\frac{\dot{w}\,\nu}{D^2 H_o^2}\right) + \left(\frac{\dot{w}}{\rho D^2}\right)^2 \frac{1}{H_o}\,\overline{u}\,\frac{\partial\overline{u}}{\partial\overline{x}} + \left(\frac{\dot{w}}{\rho D^2}\right)^2 \frac{1}{D}\,\overline{v}\,\frac{\partial\overline{u}}{\partial\overline{r}}\right] =$$

$$-\rho\,g\,\beta\,\overline{(T_i - T)}\,(T_s - T_i) - \rho\,g - \frac{\partial\overline{P}}{\partial\overline{x}}\frac{\rho D}{t^2}$$

$$+ \frac{\mu\dot{w}}{\rho D^4}\left[\left(\frac{D}{H_o}\right)^2 \frac{\partial^2\overline{u}}{\partial\overline{x}^2} + \frac{1}{\overline{r}}\frac{\partial\overline{u}}{\partial\overline{r}} + \frac{\partial^2\overline{u}}{\partial\overline{r}^2}\right]$$

Dividing through by $\dfrac{\dot{w}^2}{\rho D^4\,H_o}$ yields the following groups, which are the coefficients of the various differential terms:

1. $\dfrac{\nu D^2\rho}{\dot{w}\,H_o} = \left(\dfrac{\rho\nu D}{\dot{w}}\right)\left(\dfrac{D}{H_o}\right)$

2. $\dfrac{H_o}{D}$

3. $\quad g\dfrac{\beta(T_s-T_i)\rho^2 D^4 H_o}{\dot{w}^2}=g\dfrac{\beta(T_s-T_i)H_o D^2}{\nu^2}\left(\dfrac{H_o}{D}\right)^2\left(\dfrac{\rho\nu D}{\dot{w}}\right)^2$

$$=g\dfrac{\beta(T_s-T_i)}{\nu^2}\,H_o^{\,3}\left(\dfrac{\rho\nu D}{\dot{w}\cdot}\right)^2$$

4. $\quad \dfrac{\rho^2 g\ D^4 H_o}{\dot{w}^2}$

5. $\quad \dfrac{\rho^2 D^6}{t^2\,\dot{w}^2}=\left(\dfrac{\rho^2 D^6}{t^2\,\dot{w}^2}\right)\left(\dfrac{\nu^2 H_o^4}{\nu^2 H_o^4}\right)=\left(\dfrac{\rho^2\nu^2 D^2}{\dot{w}^2}\right)\left(\dfrac{H_o^4}{t^2\nu^2}\right)\left(\dfrac{D^4}{H_o^4}\right)$

The radial momentum equation and the continuity equation yield no new groups.

Now taking the overall energy balance, Equation 8, differientiating, and substituting the following

$$\theta=\dfrac{\dot{w}t}{\rho D^2 H_o}\quad\text{(Equivalent to }\Pi_2\,\Pi_6/\Pi_4^2\text{ , Table V)}$$

$$\overline{T}=\dfrac{T-T_i}{T_s-T_i}$$

$$M=\left(\dfrac{\rho\pi D^2 H_o}{4}-\theta\rho D^2 H_o\right)$$

$$A_w=\pi D x$$

$$A_b=\dfrac{\pi D^2}{4}$$

we obtain

$$\dot{w}\,c_p\left(\dfrac{\pi}{4}-\theta\right)\dfrac{d\overline{T}}{d\theta}(T_s-T_i)=q_w\,\pi D x+q_b\,\dfrac{\pi D^2}{4}$$

Dividing through by $\overset{\circ}{w}\,c_p\,(T_s-T_i)$, the following new dimensionless groups arise:

A-14

6. $\dfrac{q_b \, D^2}{\dot{w} \, c_p (T_s - T_i)}$

7. $\dfrac{q_b}{q_w}$

These groups along with the addition of the nondimensional distance x/H_o and   dimensional temperature $(T-T_i)/(T_s-T_i)$ form a set of 10 scaling groups.

The Pi Theorem states that 11 independent dimensionless groups are to be expected with the 15 variables previously stated. The detail derivation of Π_2 to Π_{11} is given below.

The group of parameters used to nondimensionalize Π, in Equation 12, may be repeated as the nondimensionalizing group, $q_w^a \, H_o^b \, (T_s - T_i)^c \, \nu^d \, \rho^e$, for formation of $\Pi_2 - \Pi_{10}$. Since a fifth term was added to this group for convenience by defining the Btu as a basic dimension, to form Π_{11}, one term of the repeating group is discarded from the denominator and that term is nondimensionalized by the remaining four terms.

In forming the remaining Πs the set of Equations 13 through 17 remain valid for Π_2 to Π_{10}, except the values on the right-hand-side change for each Π. The values to which these equations are set depends on the exponent of the respective basic dimension in the numerator.

A-15

For Π_2, t $\left[\theta^1\right]$

$$a = 0 \qquad\qquad\qquad\qquad a = 0$$

$$c = 0 \qquad\qquad\qquad\qquad b = 2$$

$$e = 0 \qquad\qquad\qquad\qquad c = 0$$

$$-2a+b+2d-3e = 0 \qquad\qquad d = -1$$

$$-a-d = 1 \qquad\qquad\qquad e = 0$$

Therefore, $\Pi_2 = \dfrac{t\nu}{H_o^2}$

For, Π_3, T-T$_i$ $\left[T^1\right]$

$$a = 0 \qquad\qquad\qquad\qquad a = 0$$

$$c = 1 \qquad\qquad\qquad\qquad b = 0$$

$$e = 0 \qquad\qquad\qquad\qquad c = 1$$

$$-2a+b+2d-3e = 0 \qquad\qquad d = 0$$

$$-a-d = 0 \qquad\qquad\qquad e = 0$$

Therefore, $\Pi_3 = \dfrac{T-T_i}{T_s-T_i}$

For Π_4, D $\left[L^1\right]$

$$a = 0 \qquad\qquad\qquad\qquad a = 0$$

$$c = 0 \qquad\qquad\qquad\qquad b = 1$$

$$e = 0 \qquad\qquad\qquad\qquad c = 0$$

$$-2a+b+2d-3e = 1 \qquad\qquad d = 0$$

$$-a-d = 0 \qquad\qquad\qquad e = 0$$

Therefore, $\Pi_4 = \dfrac{D}{H_o}$

For Π_5, q_b $\left[H^1 \; L^{-2} \; \theta^{-1}\right]$

$a = 1$	$a = 1$
$c = 0$	$b = 0$
$e = 0$	$c = 0$
$-2a+b+2d-3e = -2$	$d = 0$
$-a-d = -1$	$e = 0$

Therefore, $\Pi_5 = \dfrac{q_b}{q_w}$

For Π_6, $\dot{w}$ $\left[M' \; \theta^{-1}\right]$

$a = 0$	$a = 0$
$c = 0$	$b = 1$
$e = 1$	$c = 0$
$-2a+b+2d-3e = 0$	$d = 1$
$-a-d = -1$	$e = 1$

Therefore, $\Pi_6 = \dfrac{\dot{w}}{H_o \rho \, \nu}$

For Π_7, g $\left[L \; \theta^{-2}\right]$

$a = 0$	$a = 0$
$c = 0$	$b = -3$
$e = 0$	$c = 0$
$-2a+b+2d-3e = 1$	$d = 2$
$-a-d = -2$	$e = 0$

Therefore, $\Pi_7 = g \, \dfrac{H_o^3}{\nu^2}$

A-17

For Π_8, c_p $\left[H^1 \ M^{-1} \ T^{-1}\right]$

$\qquad$ a = 1 $\qquad\qquad\qquad$ a = 1

$\qquad$ c = -1 $\qquad\qquad\qquad$ b = 1

$\qquad$ e = -1 $\qquad\qquad\qquad$ c = -1

$\qquad$ -2a+b+2d-3e = 0 $\qquad$ d = -1

$\qquad$ -a-d = 0 $\qquad\qquad\qquad$ e = -1

Therefore, $\Pi_8 = \dfrac{c_p \ (T_s - T_i) \rho \ \nu}{q_w \ H_o}$

For Π_9, k $\left[H \ L^{-1} \ T^{-1} \ \theta^{-1}\right]$

$\qquad$ a = 1 $\qquad\qquad\qquad$ a = 1

$\qquad$ c = -1 $\qquad\qquad\qquad$ b = 1

$\qquad$ e = 0 $\qquad\qquad\qquad$ c = -1

$\qquad$ -2a+b+2d-3e = -1 $\qquad$ d = 0

$\qquad$ -a-d = -1 $\qquad\qquad\qquad$ e = 0

Therefore, $\Pi_9 = \dfrac{k \ (T_s - T_i)}{q_w \ H_o}$

For Π_{10}, q_w is taken from the group of repeaters and the remaining four are used to non-dimensionalize q_w.

$$\Pi_{10} = \frac{q_w}{H_o^a \ (T_s - T_i)^b \ \nu^c \ \rho^d}$$

$$\frac{\left[M^1 \ \theta^{-3}\right]}{\left[L'\right]^a \ \left[T'\right]^b \ \left[L^2 \theta^{-1}\right]^c \ \left[M'L^{-3}\right]^d}$$

For M $d = 1$ $a = -3$

For θ $-c = -3$ $b = 0$

For L $a+2c-3a = 0$ $c = 3$

For T $b = 0$ $d = 1$

Therefore, $\Pi_{10} = \dfrac{q_w \, H_o{}^3}{\nu^3}$

For Π_{11}, $\left[T^{-1} \right]$

   $a = 0$ $a = 0$

   $c = -1$ $b = 0$

   $e = 0$ $c = -1$

  $-2a+b+2d-3e = 0$ $d = 0$

   $-a-d = 0$ $e = 0$

Therefore, $\Pi_{11} = \beta(T_s - T_i)$

TABLE A-1   Normalization Parameters

$$\overline{u} = \frac{u\, \rho\, D^2}{\dot{w}}$$

$$\theta = \frac{t\, \nu}{H_o^2}$$

$$\overline{v} = \frac{v\, \rho\, D^2}{\dot{w}}$$

$$\overline{x} = \frac{x}{H_o}$$

$$\overline{T} = \frac{T - T_i}{T_s - T_i}$$

$$\overline{r} = \frac{r}{D}$$

$$\overline{P} = \frac{P\, t^2}{\rho\, D^2}$$

$$N_1 = \frac{x}{H_o}$$

$$N_6 = \frac{\dot{w}}{\rho \nu D}$$

$$N_2 = \frac{\nu t}{H_o^2}$$

$$N_7 = \frac{g \beta q_w H_o^4}{k \nu^2}$$

$$N_3 = \frac{T - T_i}{T_s - T_i}$$

$$N_8 = \frac{q_b D^2}{\dot{w} c_p (T_s - T_i)}$$

$$N_4 = \frac{D}{H_o}$$

$$N_9 = \frac{\dot{w}^2}{g \rho^2 D^4 H_o}$$

$$N_5 = \frac{q_b}{q_w}$$

$$N_{10} = \frac{\nu c_p \rho}{k}$$

TABLE A-3 Pertinent Variables

Geometric

H_o, initial liquid level

D , tank diameter

Kinematic

ν , kinematic viscosity

ρ , density

Dynamic

$\dot{w}$, drain rate

x , position measured axially from tank bottom

g , gravitational acceleration

β , coefficient of thermal expansion

Thermal

q_w, average tank wall heat flux

q_b, average tank bottom heat flux

$T-T_i$, local temperature difference

T_s-T_i, surface temperature difference

t , time

k , conductivity

C_p, heat capacity

TABLE A-4   Derived Pi Gropings

$$\Pi_1 = \frac{x}{H_o}$$

$$\Pi_6 = \frac{\dot{w}}{\rho \nu H_o}$$

$$\Pi_2 = \frac{t \nu}{H_o^2}$$

$$\Pi_7 = \frac{g H_o^3}{\nu^2}$$

$$\Pi_3 = \frac{T - T_i}{T_s - T_i}$$

$$\Pi_8 = \frac{c_p (T_s - T_i) \nu \rho}{q_w H_o}$$

$$\Pi_4 = \frac{D}{H_o}$$

$$\Pi_9 = \frac{k (T_s - T_i)}{q_w H_o}$$

$$\Pi_5 = \frac{q_b}{q_w}$$

$$\Pi_{10} = \frac{q_w H_o^3}{\nu^3 \rho}$$

$$\Pi_{11} = \beta (T_s - T_i)$$
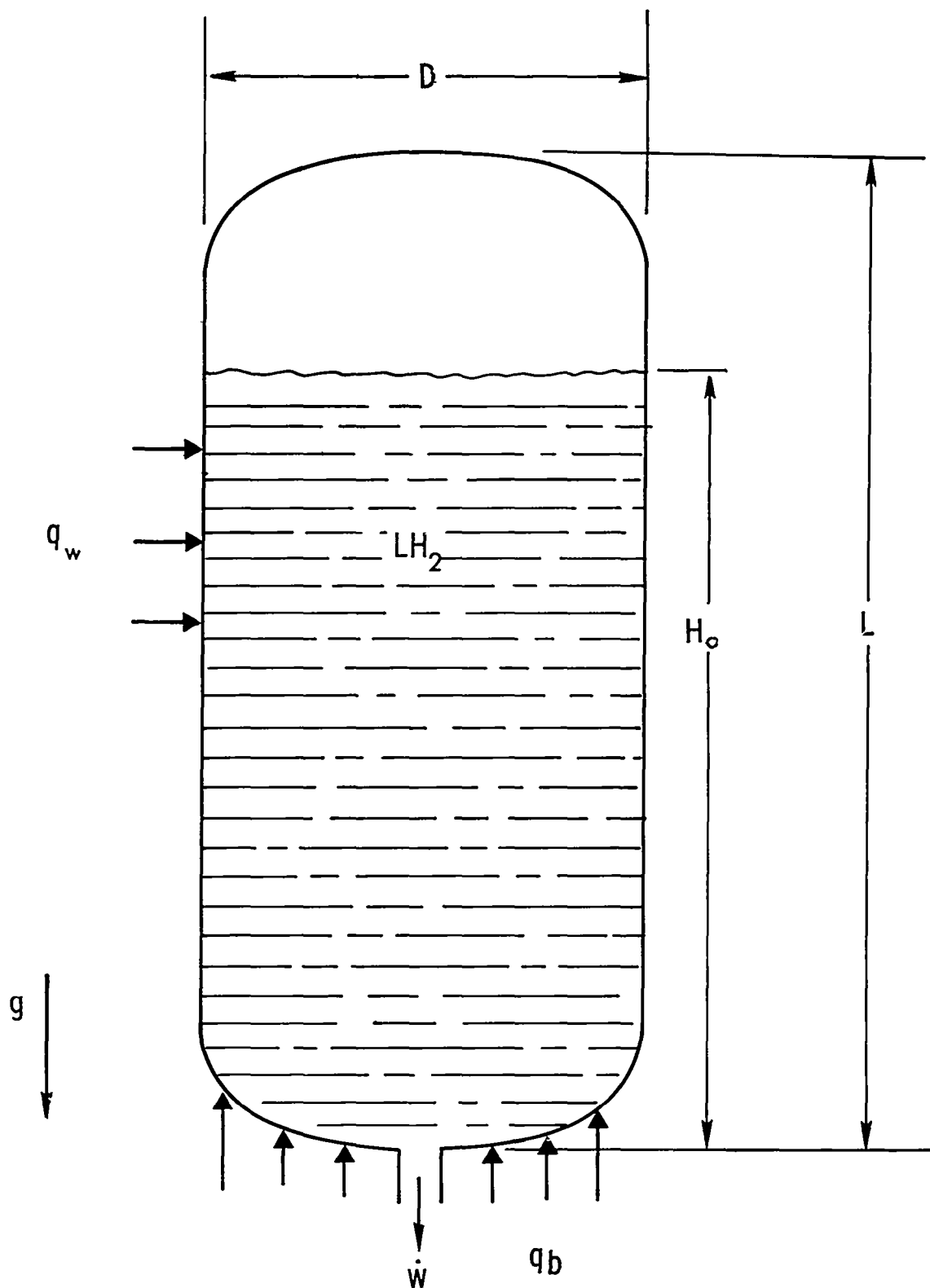
Figure A-1   Physical Variables

APPENDIX B

DESCRIPTION OF ANALYTICAL PROCEDURES

B-1 COMPUTER CODE AG4

Computer Code AG4 is the Fort Worth operation's desig-
nation for the Asymmetric Propellant Heating Computer Pro-
gram developed by LMSC as part of Phase I of the Modular
Nuclear Vehicle Study (Ref. 2). The code is based on a
stratification and pressurization model which treats a
draining axisymmetric vessel under variable acceleration and
allows for asymmetric heating effects. The liquid is treated
in a stepwise-in-time manner and is stratified in horizontal
layers by the assumed quasi-steady boundary-layer flow
along the heated vessel walls. The boundary-layer flow is
considered to be turbulent and includes both wall and nuclear
(source) heating. Bulk nuclear heating is also included.
The pressurization is treated in a continuous manner and
couples the ullage with the liquid and the wall through mass
and energy transfer, and includes continuous or intermittent
pressurization or venting. The ullage region is considered
to be a lumped system (one node) as is the tank wall. Tem-
perature and low-pressure dependent values are considered
for liquid, vapor, wall, and tank-insulation properties.

B-2   COMPUTER CODE RIO

The Fort Worth operation code RIO is a modified version
of the code developed by NASA/LeRC to analyze the 125-gal
tank test data generated by the FWD in 1963. The analytic
model upon which this procedure is based is given in Reference
1. The physical problem solved is that of a draining,
axisymmetric tank subjected to a constant pressure from an
active pressurization system. No ullage-liquid interactions
are considered. Flow into the stratified region of the
liquid is based on turbulent free-convection along the
heated walls. Wall and bulk nuclear heating is a tabular
input group as a function of axial distance from the tank
bottom. Constant property values are assumed. This problem
is solved by assuming a plausible temperature profile which
is made to satisfy the momentum and energy equations based
on the entire fluid in the tank. The program is written
in FORTRAN IV language compatible with the IBM System 360.

B-3   COMPLETE-MIX MODEL

The complete-mix model applies to a draining axisymmetric
tank and assumes that all ambient and nuclear energy inputs
to the tank are instantly distributed uniformly throughout
the remaining liquid. No ullage interactions are considered.
The heating inputs are, however, functions of the liquid

level and are therefore time variant. Constant property values are assumed.

The constant Q complete-mix model differs from the complete-mix model only in that the heating rates applicable at the initial liquid level are assumed to apply throughout the drain period.

APPENDIX C

RNS DUAL-CELL CONCEPT ANALYSIS

C-1 INTRODUCTION AND SUMMARY

The concept of the Reusable Nuclear Shuttle propellant storage system that consists of a single external tank with an internal tank was reviewed to determine possible problems based on thermodynamic considerations. This configuration of the RNS is defined by North American Rockwell Space Division (Ref.4).

Nuclear data for this analysis was based on the Aerojet-General source terms for the 1500-MW hot-bleed NERVA engine given in Reference 16.

No specific problems were found that would cause the feasibility of this concept to be questioned. However, the addition of the internal tank does cause several additional weight penalties and thermodynamic problems not present in a single-tank design. Three problem areas have been investigated and the results are discussed: (1) local boiling, (2) prepressurization requirements, and (3) drain temperature.

C-2 LOCAL BOILING

The possibility of boiling within the tank during prepressurization, firing, and cool-down modes was investigated. The prime problems are associated with the internal tank and

intercell feed lines where they interface with hot ullage and the penetration heat leak at the internal tank mount. It was estimated that the highest heat flux to the fluid, during proper operation of the thermodynamic vent system, will be 11 Btu/h-ft^2-$^{\circ}$R, which is well below the incipient boiling critical heat flux. ·Failure of the thermodynamic vent system could, however, result in heat fluxes large enough to cause boiling under coast. and cool-down conditions at the point where the internal tank mounts to the external tank (one of the vent system functions is to produce subcooled liquid in the lower regions of the tank). The consequences of boiling at this point would be particularly severe since the vapor would be trapped under the zero-g propellant retention screens. Vapor trapped in this location could enter the intercell feed lines resulting in a higher pressure required to force feed the internal tank.

C-3 PREPRESSURIZATION REQUIREMENTS

Figure C-1 presents the relationship of the liquid levels to the tank geometry after the completion of the TLI burn. The cold column of liquid hydrogen contained in the internal tank not only reduces the average ullage temperature but also provides a cold surface on which the gaseous hydrogen (ullage) may condense. The net effect is about a threefold increase in the mass of auxiliary pressurization gas required compared

Internal Tank Liquid Level

External Tank Liquid Level
After TLI Burn
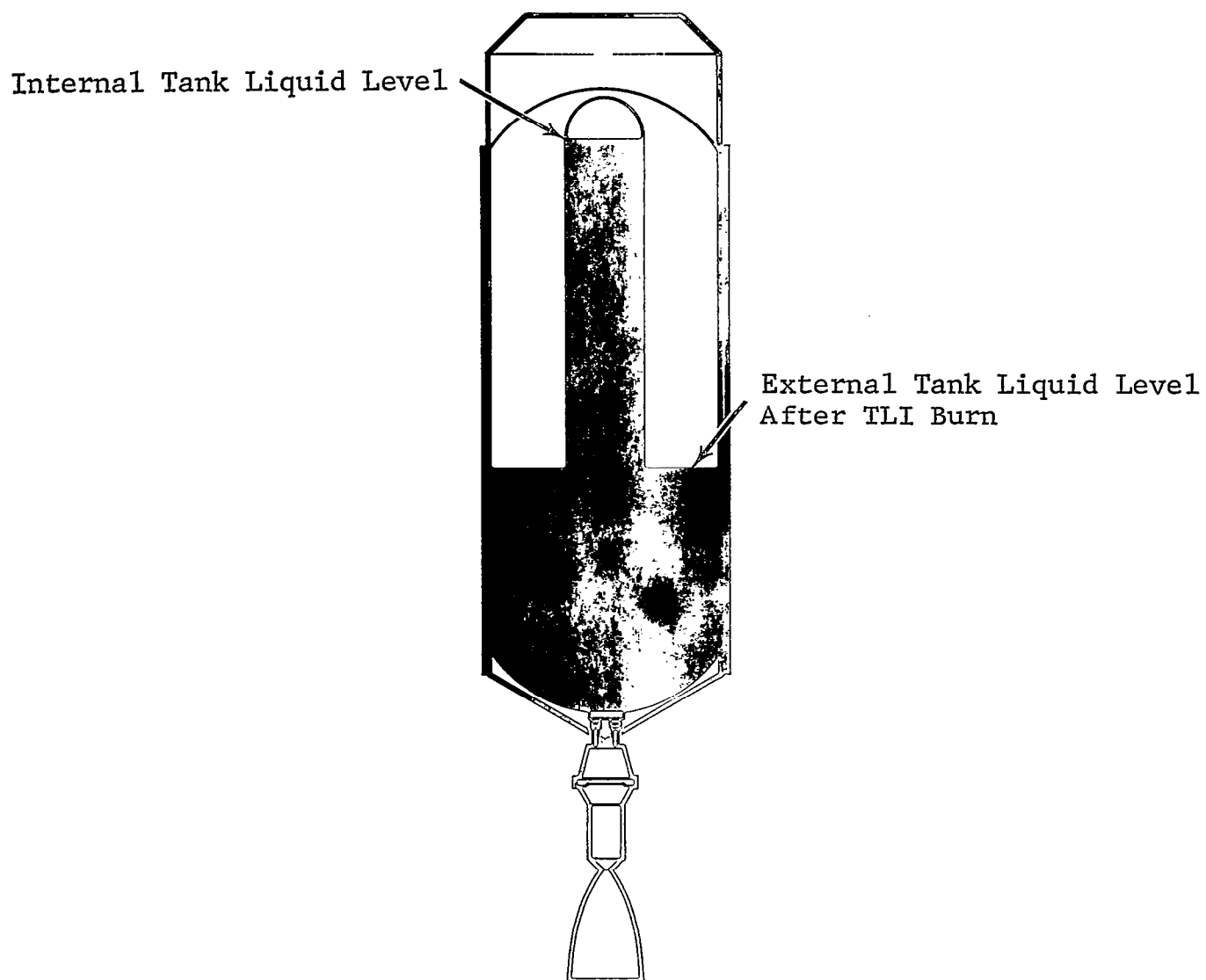
Figure C-1 Dual-Cell Design RNS

with a single-tank concept. Because of condensation, the pressurization gas required during firing is greater for the dual-cell concept than for a single-tank design. For example, a peak pressurization flow rate without an internal tank is estimated to be 0.75 lb/sec while with the internal tank this peak pressurization flow rate is increased to 1.7 lb/sec.

It can be concluded from the above that the presence of the internal tank substantially increases the mass of stored prepressurization gas required. This condition appears to have been included in NAR's assessment of the auxiliary pressurization system weight penalty.

C-4 DRAIN-TEMPERATURE PROFILES

Drain-temperature profiles were generated for each of the four main engine burns of the lunar shuttle mission. The drain-temperature analysis is based on a mixed model and uses the nuclear heating rates presented in Figure C-2. The mixed model assumes that the energy being absorbed by the LH_2 is completely and instantly mixed throughout the LH_2 remaining at any time step. The ambient heat flux to the external tank is proportional to the tank surface area wetted by the LH_2 at any time step. The nuclear heating is also time varient since it depends upon the $LH2$ remaining in the tanks at any given time. The tanks were analyzed assuming that they were drained in series.
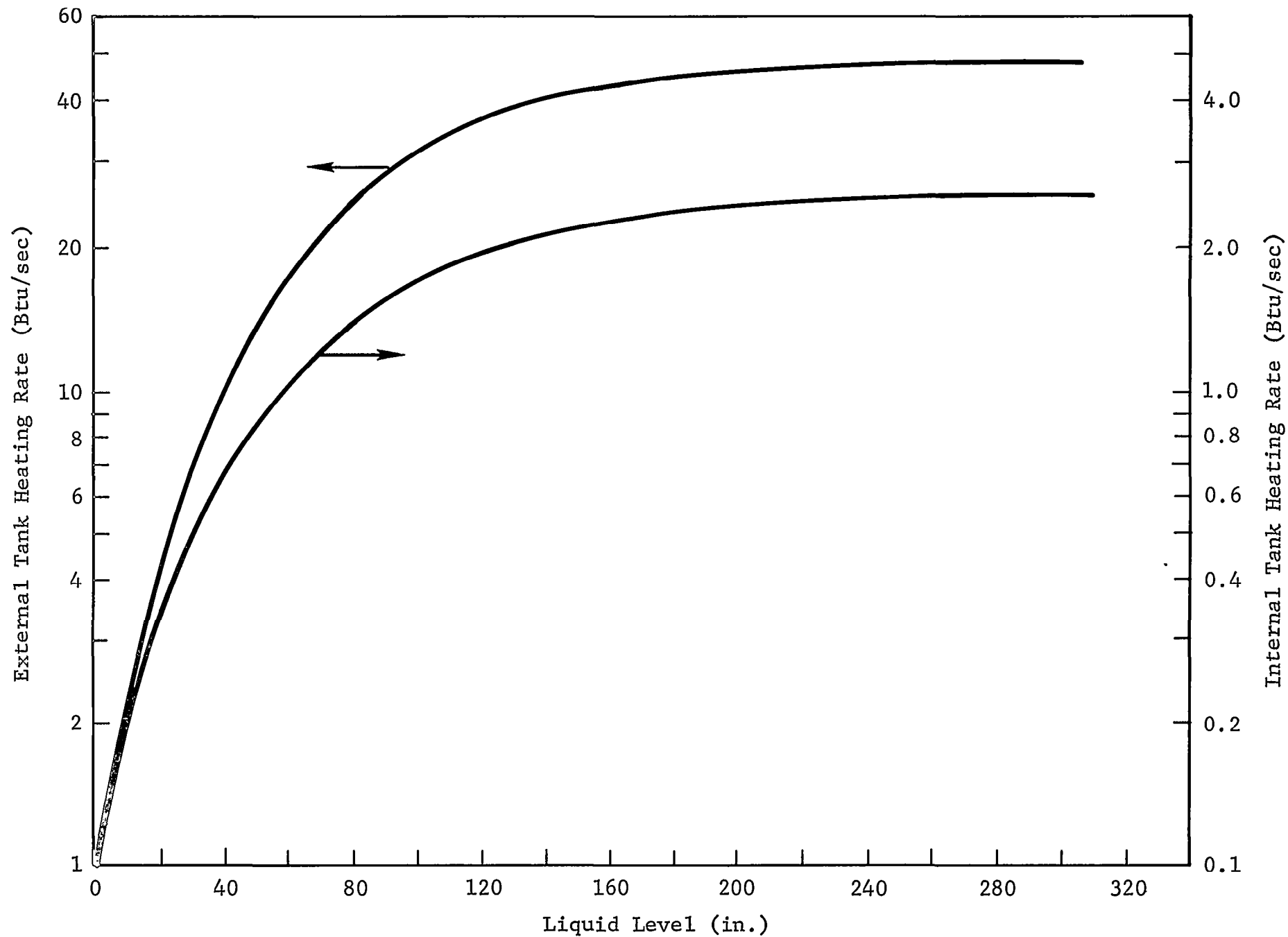
Figure C-2 Nuclear-Energy Deposition Rate

Figures C-3 through C-6 present the drain-temperature profiles for the TLI, LOI, TEI, and EOI burns. The LH_2 was assumed to be initially at 24-psi saturated conditions for each burn.

The use of an internal tank creates an additional heat load on the draining fluid caused by the increase in wetted area. The primary heat load is due to ullage condensing on the exposed area of the internal tank. This heat load can produce up to 66 percent of the total increase in drain temperature (main tank empty, internal tank draining). A secondary heat load is created by the $LH2$ passing through the high radiation field twice. In addition, the fact that the internal tank is used as a shield means that a significant amount of energy is deposited in the internal tank and with the new full-flow engine this could be significant. The effect of this design change on drain temperature was not analyzed at this time because adequate design data were not available.

The net effect of the drain-temperature rise is an increase in saturation temperature and pressure of the LH_2 in the tank. For the four main engine burns, the saturation pressure will not exceed the tank pressure operating limit of 32.1 psia. The maximum drain temperature of 41.55°R occurs after the external tank is empty during the EOI burn. This temperature corresponds to a pressure of 30.5 psia. With an estimated 0.6-psi feed-
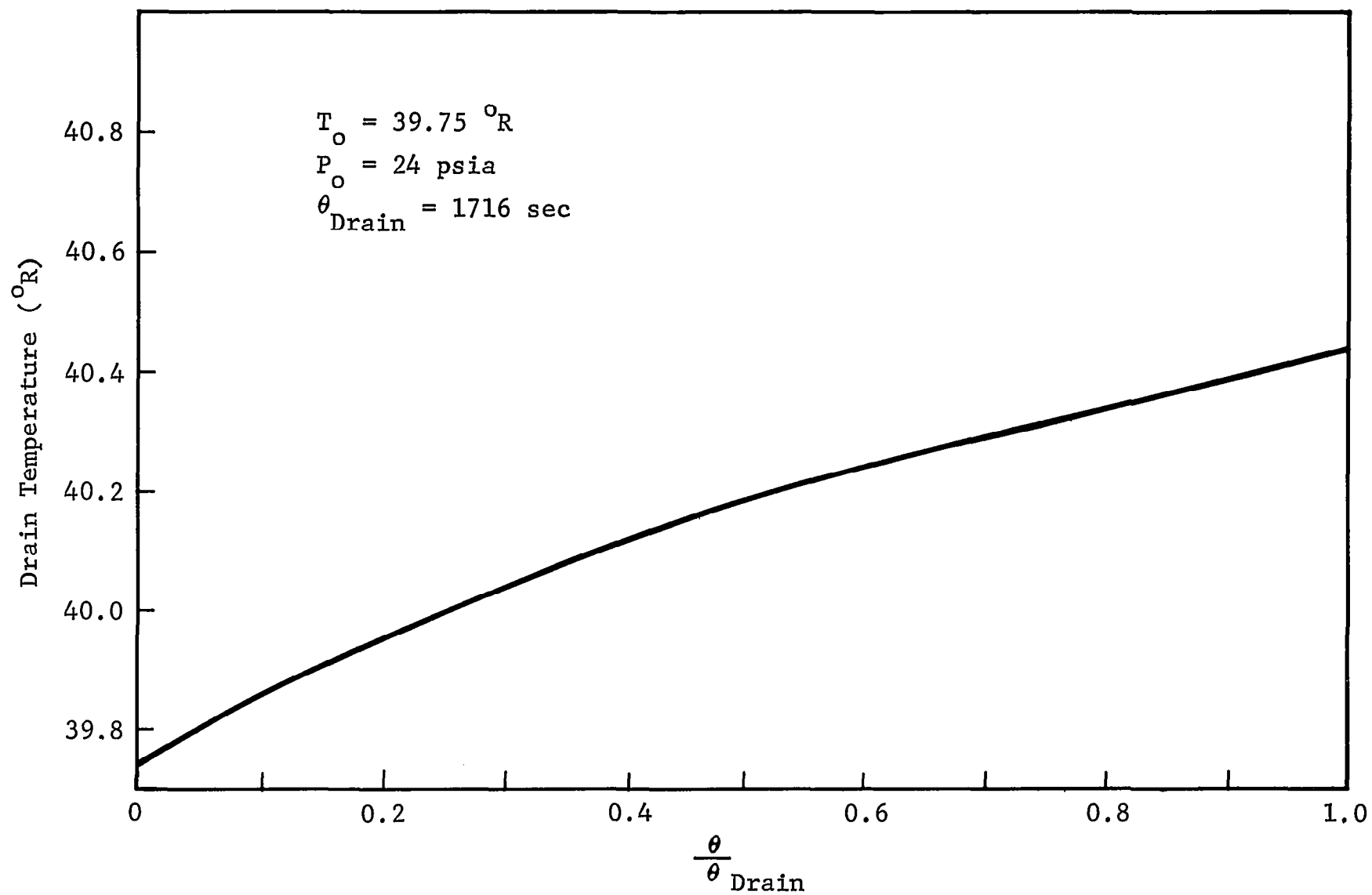
Figure C-3   Drain-Temperature Profile for TLI Burn
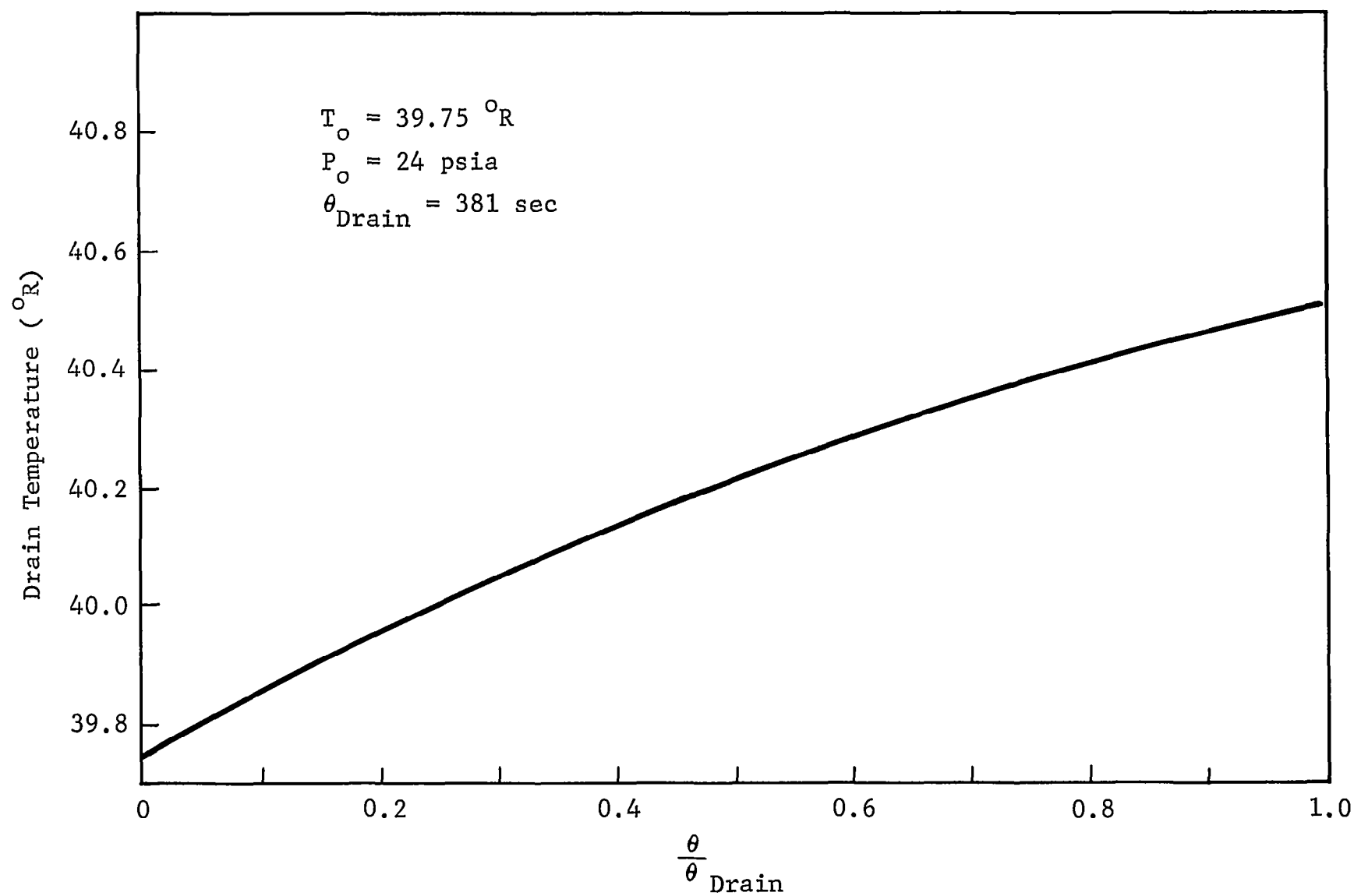
Figure C-4   Drain-Temperature Profile for LOI Burn
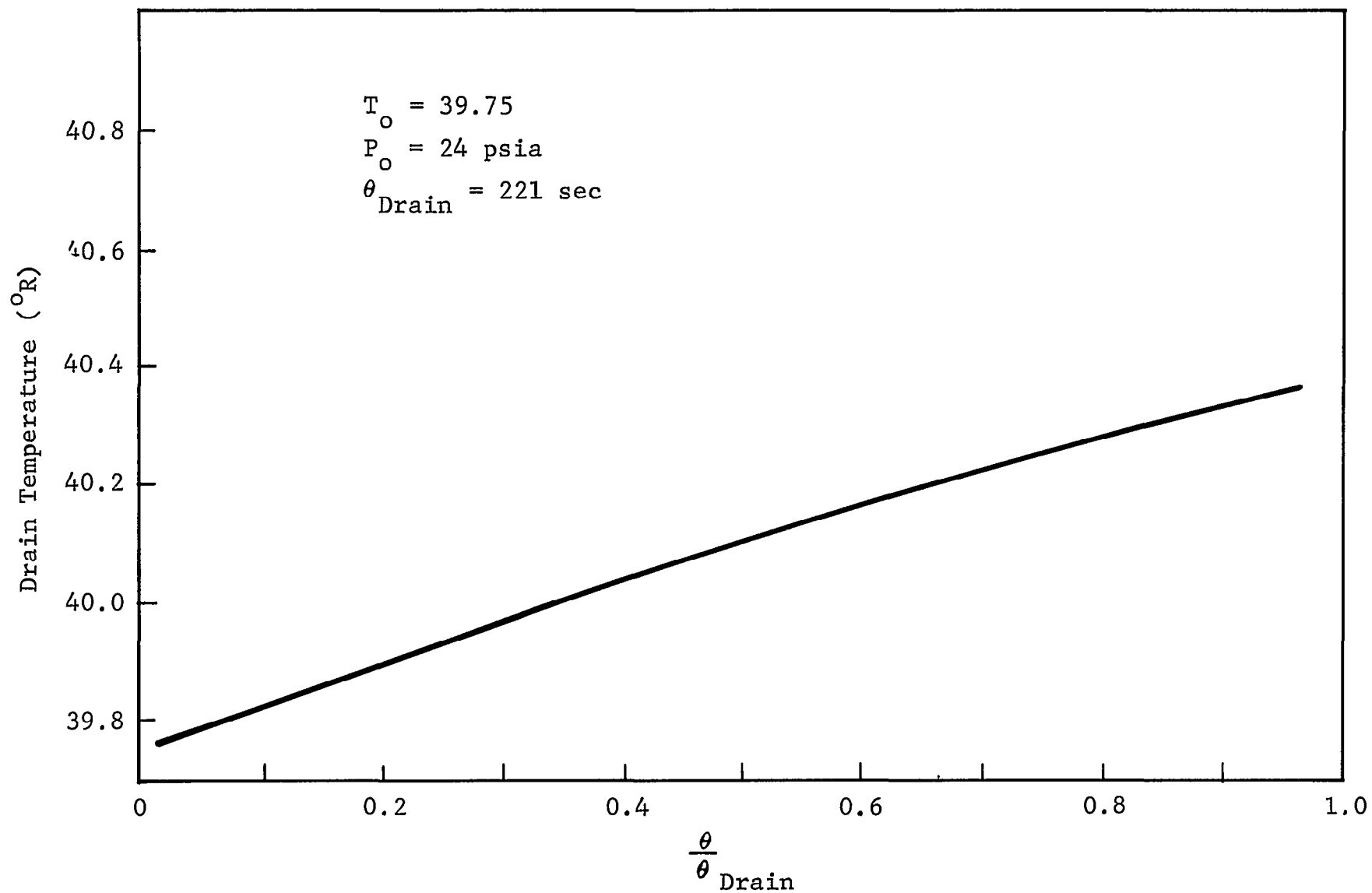
Figure C-5   Drain-Temperature Profile for TEI Burn
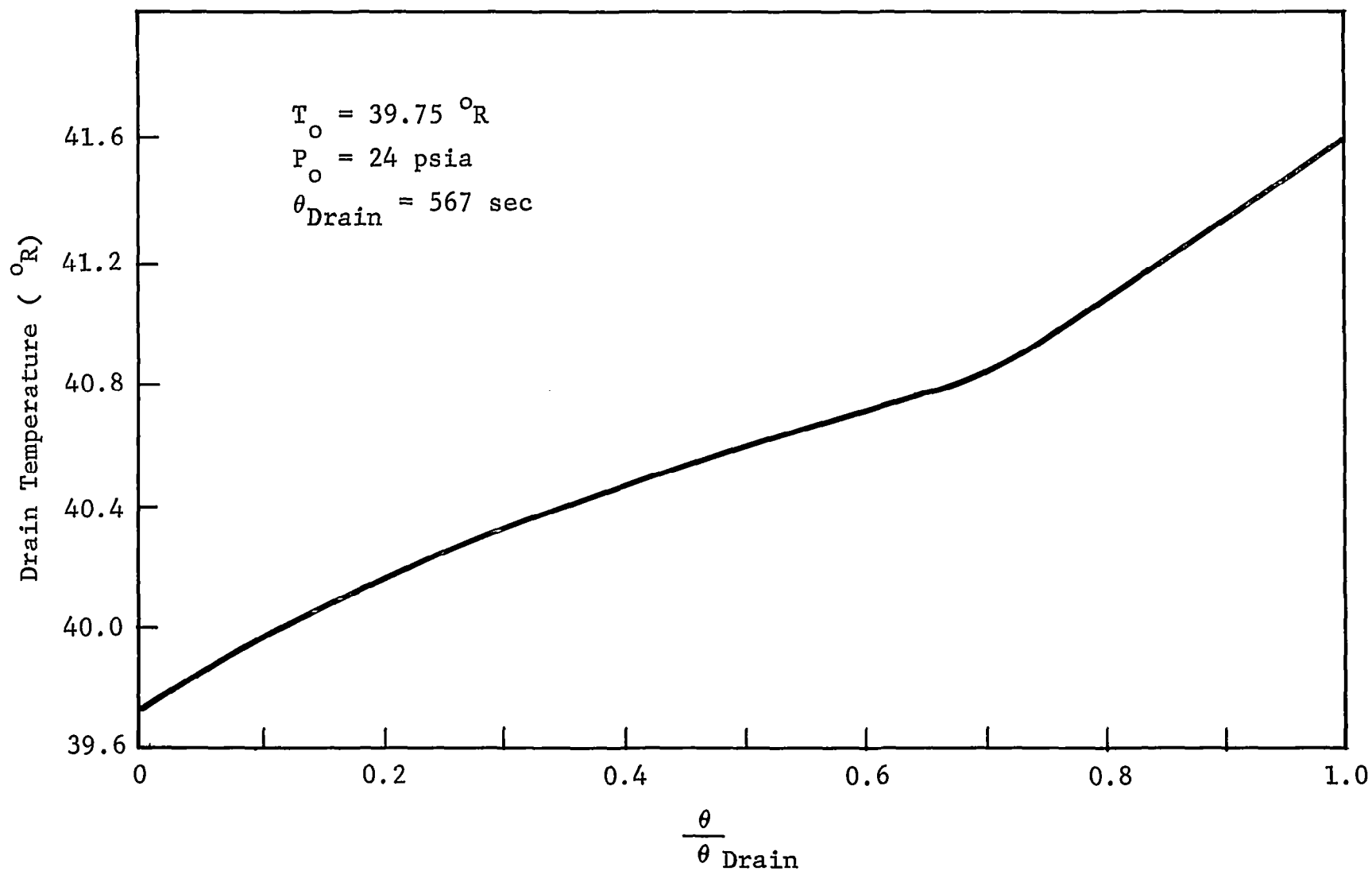
Figure C-6 Drain-Temperature Profile for EOI Burn

system loss and a 0.5-psi margin, the required saturation pressure will be 31.6 psia.

After each burn the tank will be vented to 24 psia. Boil-off losses due to this venting were estimated at 1410 pounds.

APPENDIX D

DRAIN-TEMPERATURE PLOTS

Figures D-1 through D-25 are PHT drain-temperature plots predicted using computer code RIO. The PHT operating conditions for the data shown in the plots correspond to those in Table 4-2 for the applicable run number.
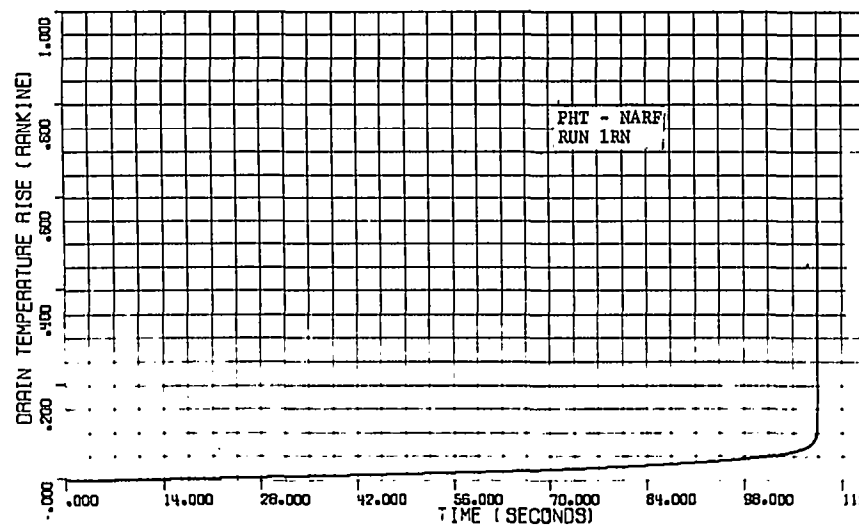
Figure D-1
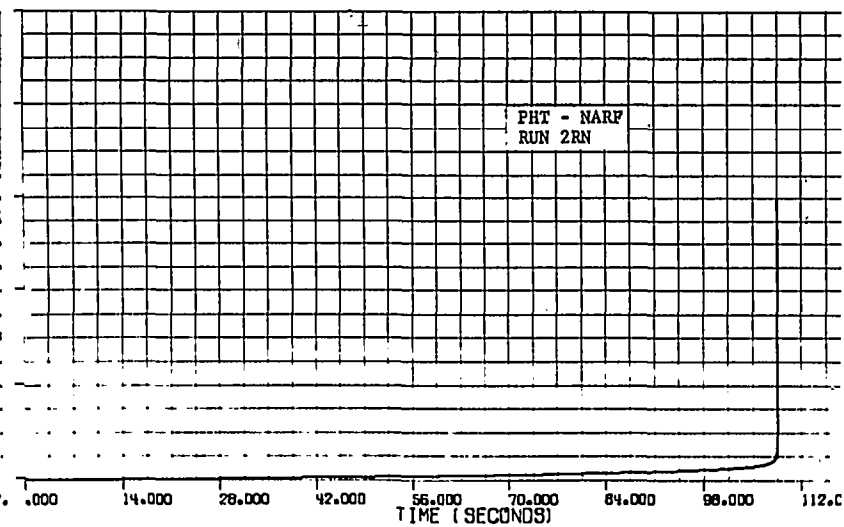
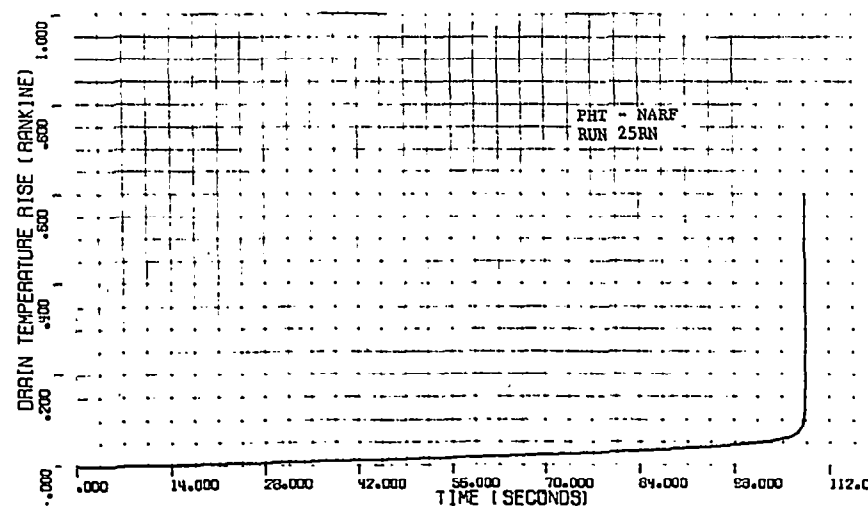Figure D-2
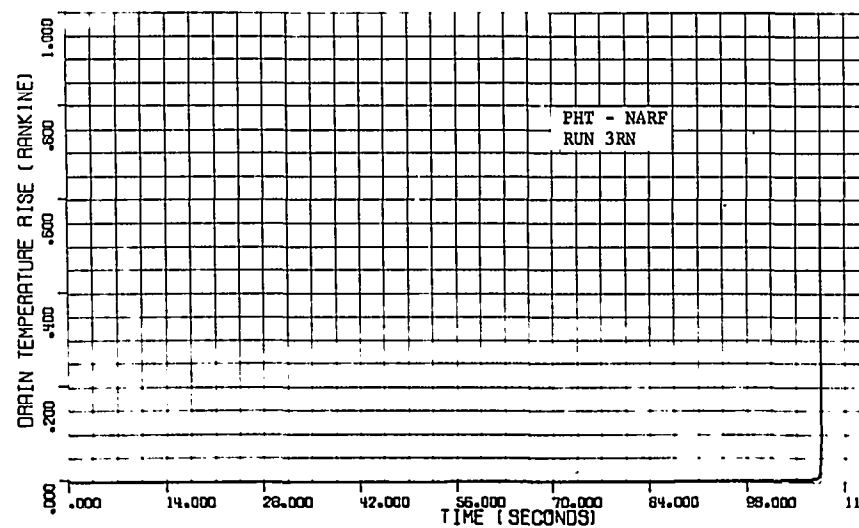
Figure D-3
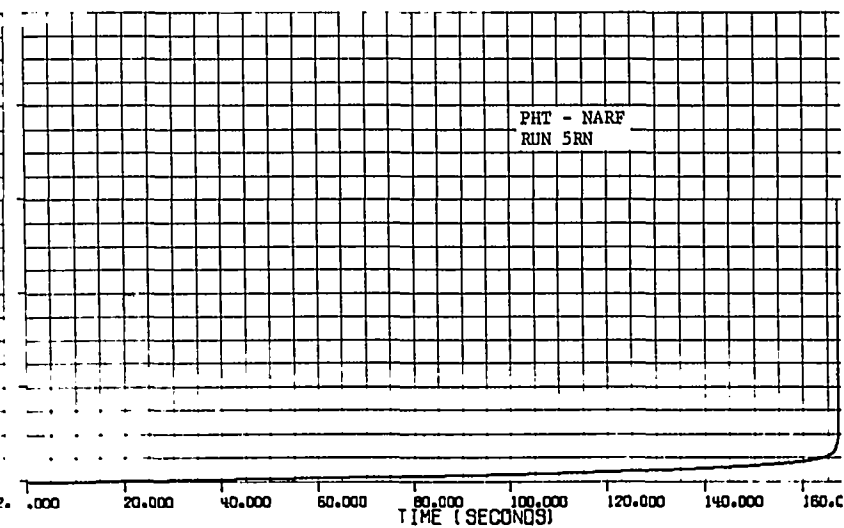
Figure D-4
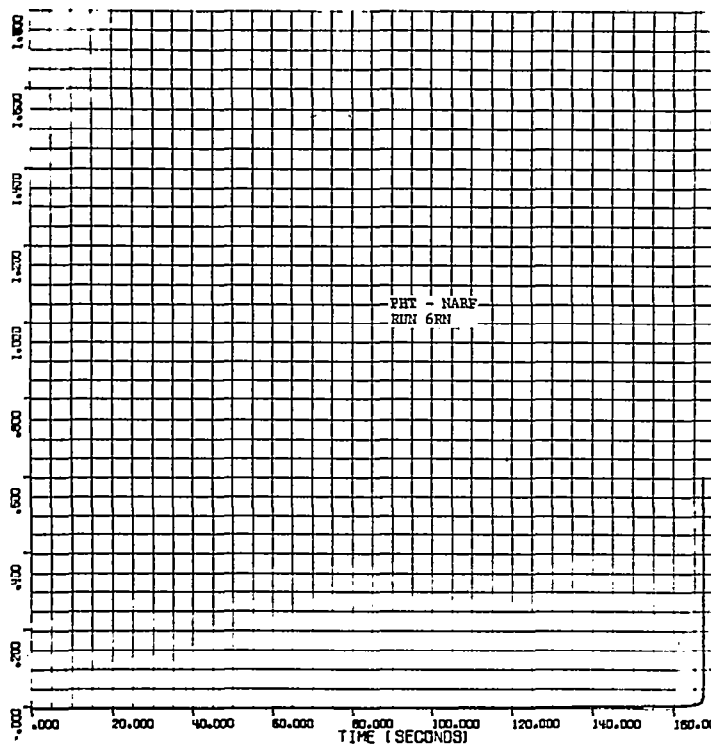
Figure D-5
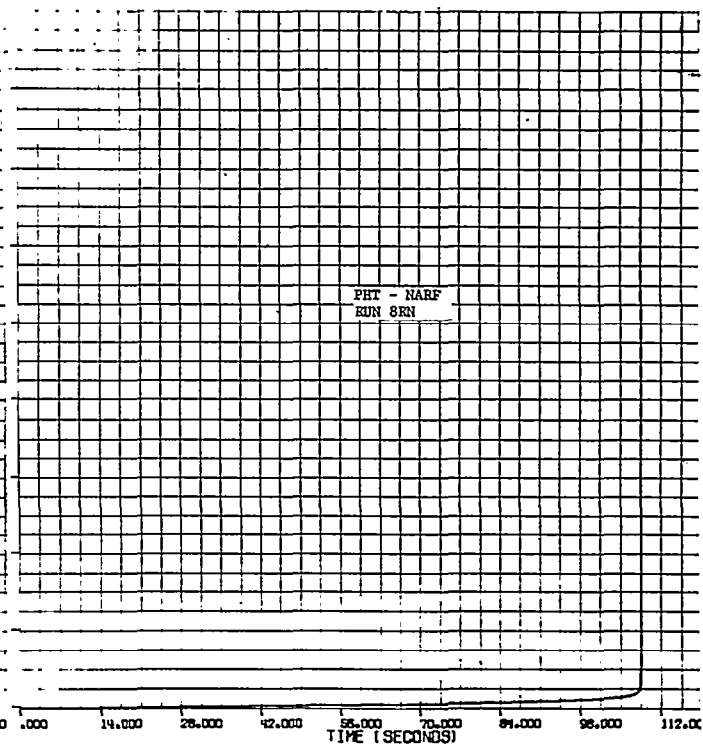
Figure D-6
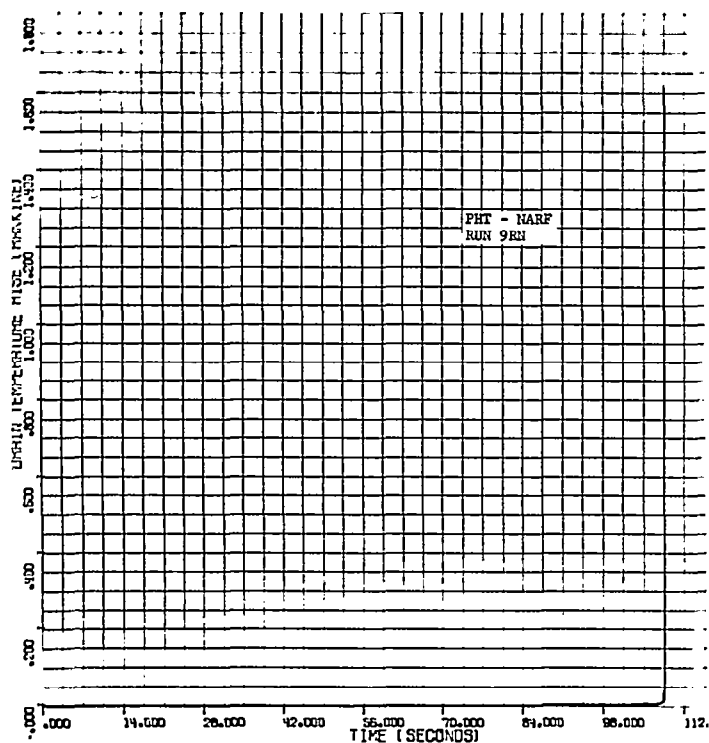
Figure D-7

Figure D-8

D-3
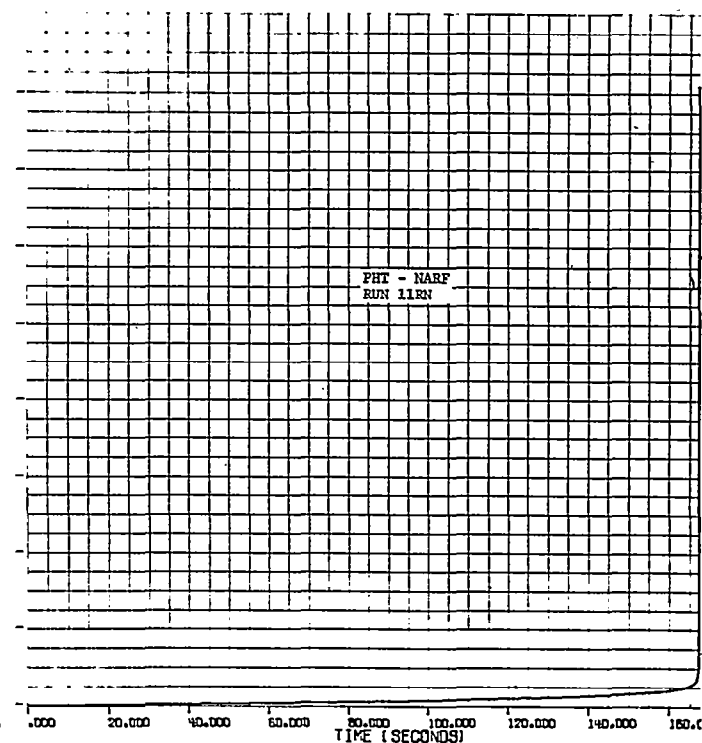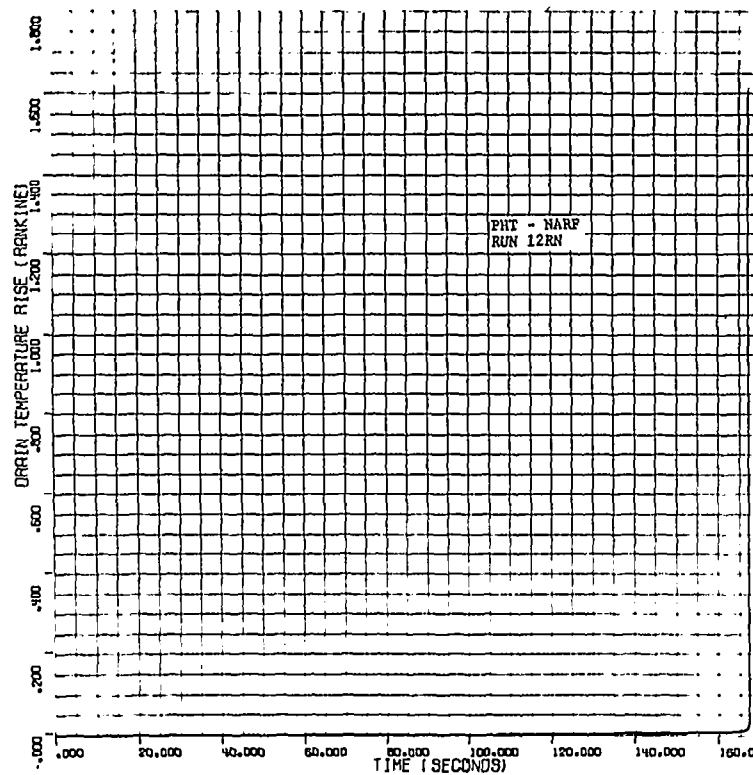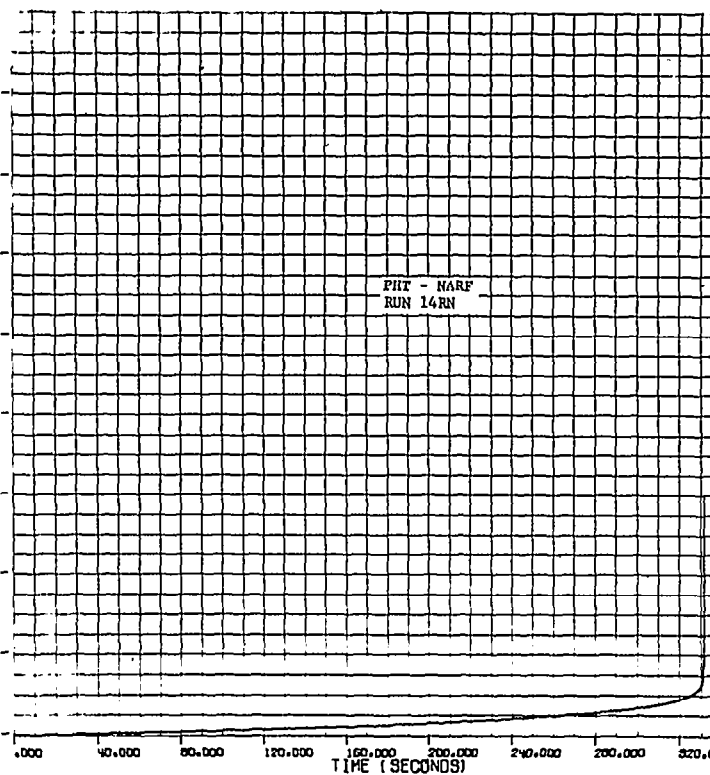
Figure D-9

Figure D-10
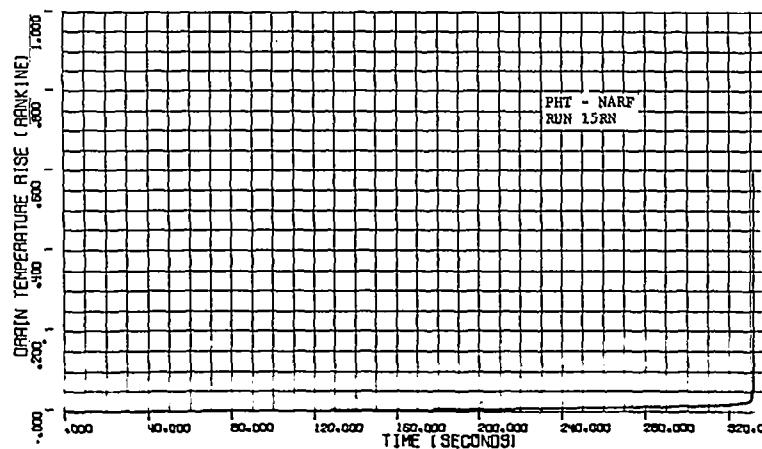
Figure D-11

Figure D-12

D-4
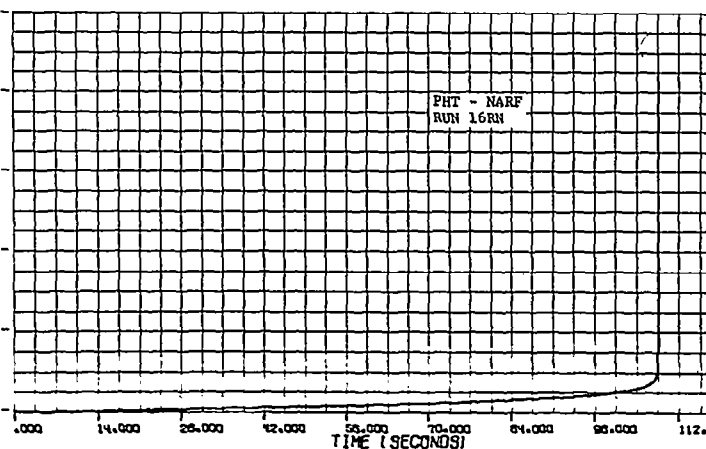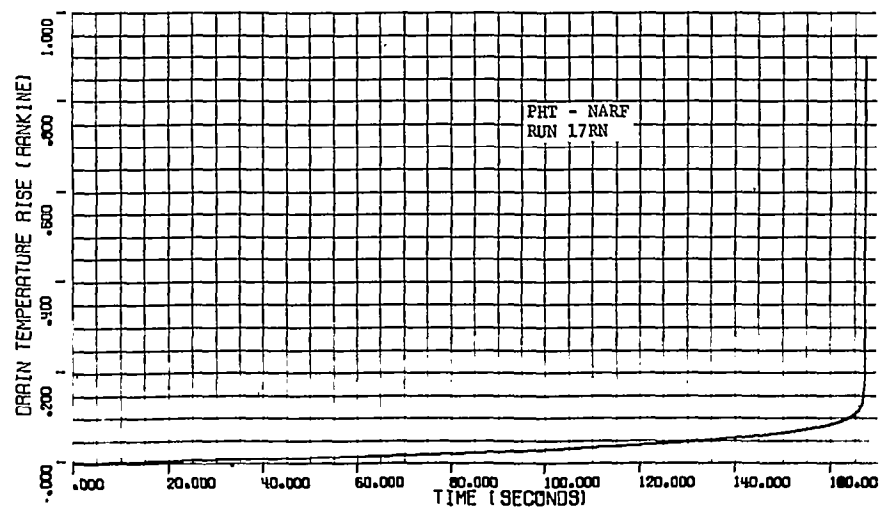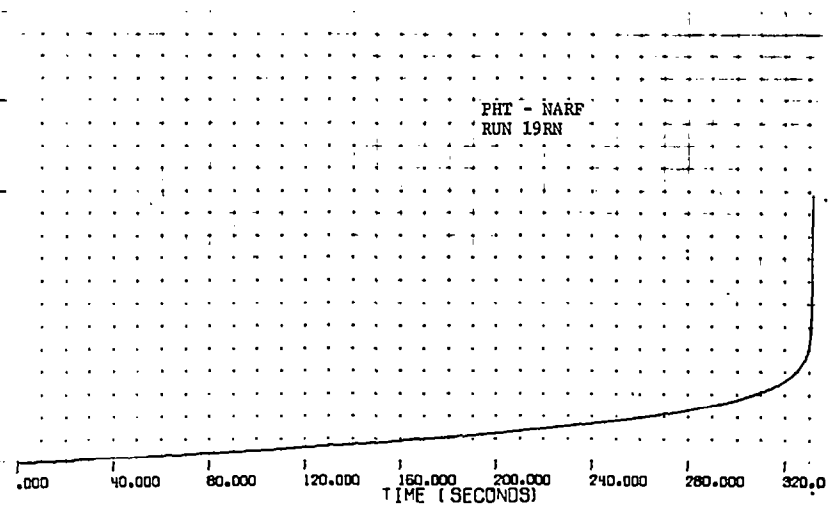
Figure D-13

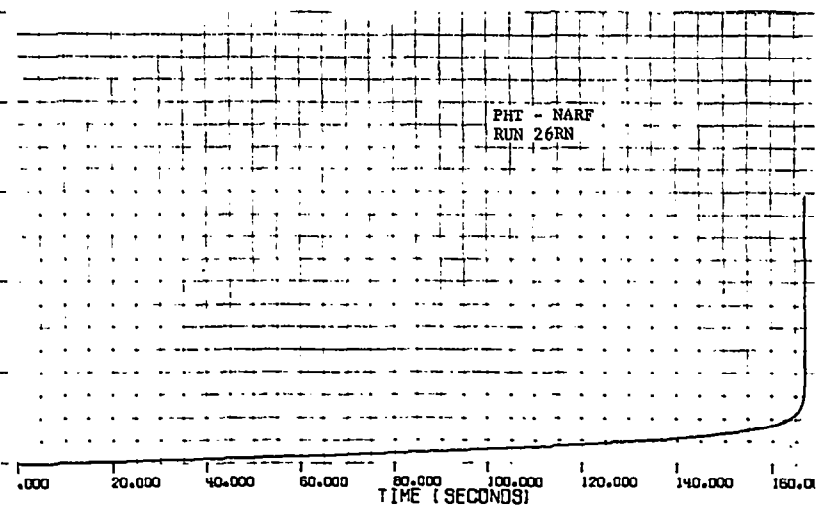Figure D-14
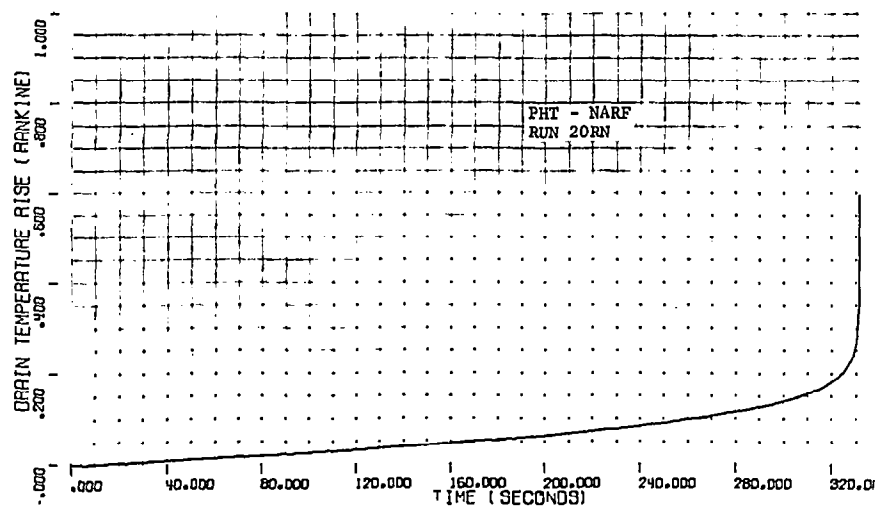
Figure D-15
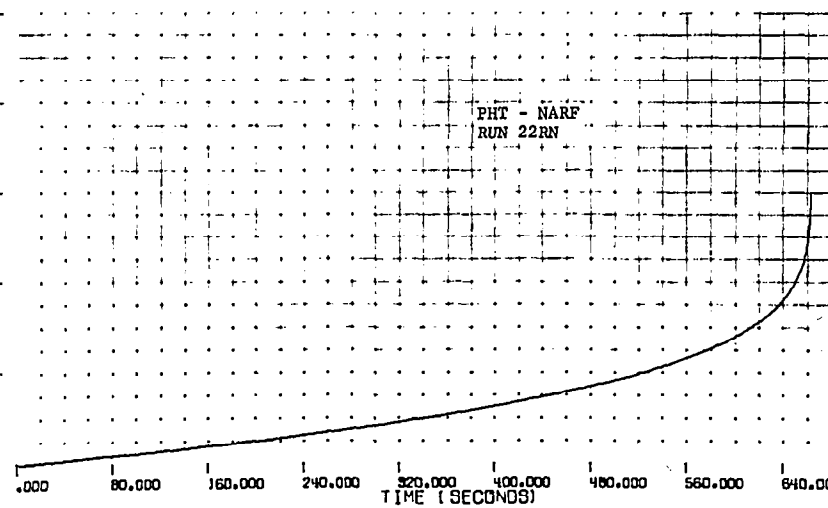
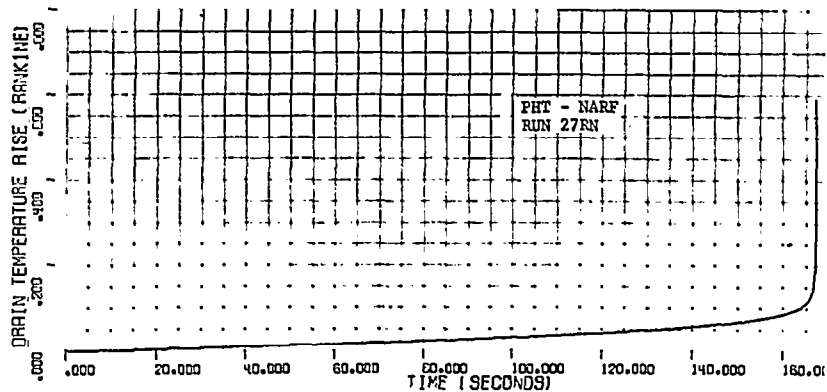Figure D-16
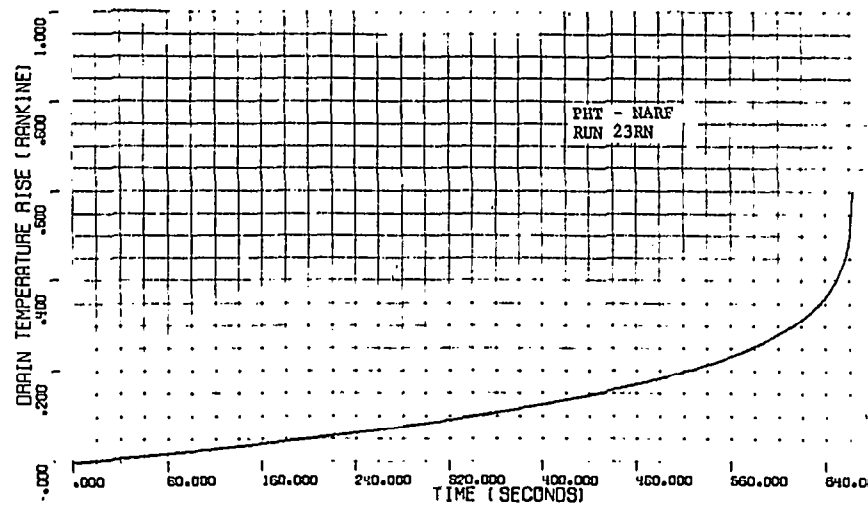
Figure D-17
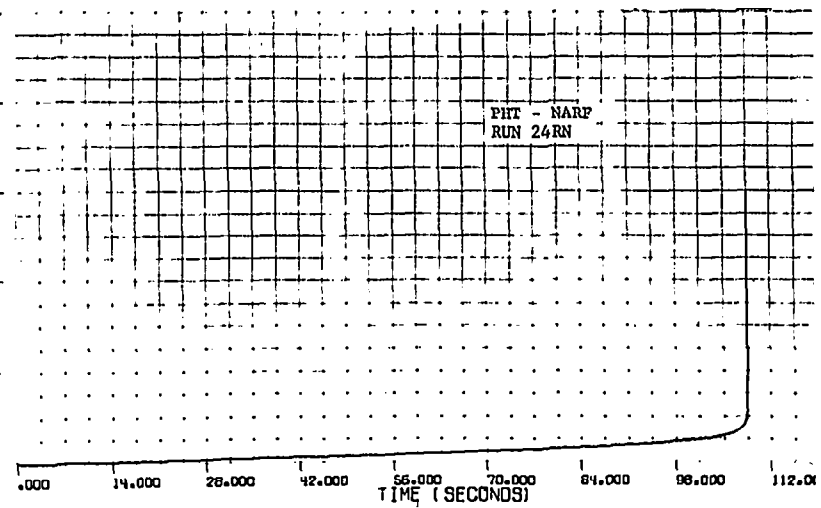
Figure D-18

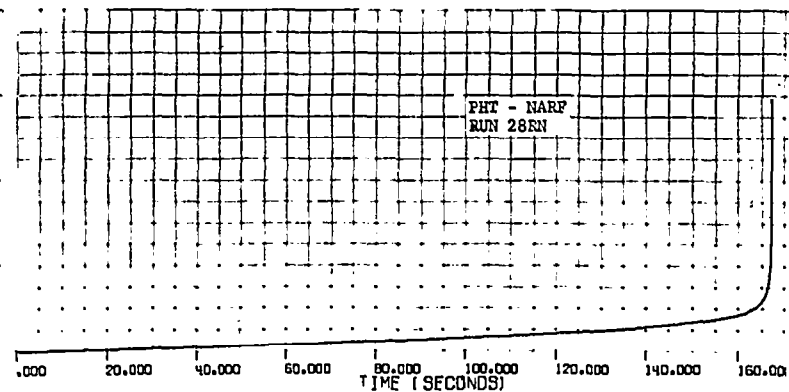Figure D-19

Figure D-20
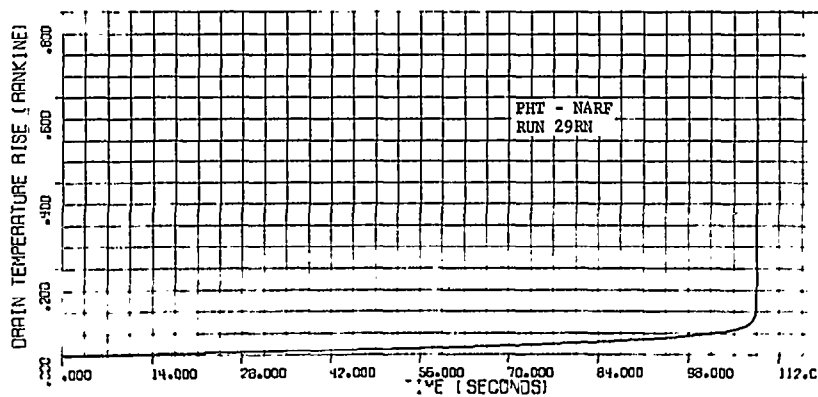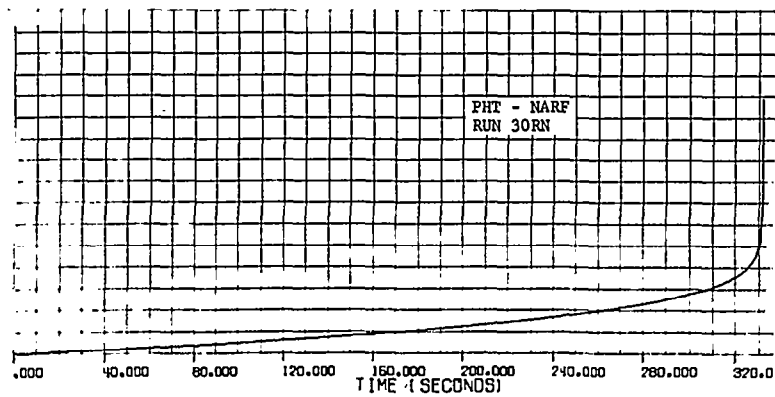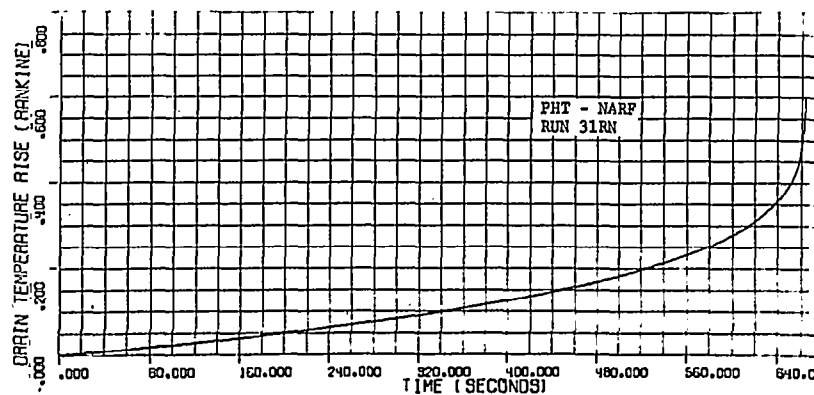
Figure D-21

Figure D-22

Figure D-23

Figure D-24

Figure D-25

REFERENCES

1. Kerlin, E. E., Hehs, W. A., Westerheide, D. E., McCauley, B. O., _Evaluation of Cryogenic Insulation Materials and Composites for Use in Nuclear Radiation Environments - Final Analytical Progress Report on Propellant Heating Test (1 October 1967 through 31 December 1967)_, General Dynamics/Fort Worth Division Report FZK-350, February 1968.

2. _Nuclear Flight System Definition Study Final Report_, McDonnell Douglass Astronautics Co. Report, MDC-G0585, May 1970.

3. _Nuclear Flight System Definition Study Final Report_, Lockheed Missiles & Space Co. Report, LMSC-A968223, May 1970.

4. _Nuclear Flight System Definition Study Phase II Final Report_, North American Rockwell Space Division Report SD70-117, April 1970.

5. _NERVA Reference Data (Full-Flow Engine)_, Aerojet Nuclear Systems Company Report S130-CP-090290-F1-PREL, April 1970.

6. _Evaluation of Insulation Materials and Components for Use in a Nuclear Radiation Environment - First Quarterly Progress Report (21 May through 31 August)_, General Dynamics Report FZK-373, 15 September 1970.

7. _Evaluation of Insulation Materials and Components for Use in a Nuclear Radiation Environment - Second Quarterly Progress Report (1 September through 30 November)_, General Dynamics Report FZK-375, 15 December 1970.

8. _Evaluation of Insulation Materials and Components for Use in a Nuclear Radiation Environment - Third Quarterly Progress Report (1 December through 28 February 1971)_, General Dynamics Report FZK-377, 15 March 1971.

9. _Computer Code For Calculating Temperature Profiles in a Propellant Tank_, R. L. Danilowicz NASA TM X-1556, April 1968.

10. _Modular Nuclear Vehicle Study, Volume IV, Axisymmetric Propellant Heating Computer Program_, Lockheed Missile and Space Co., LMSC-A794909-A, 15 September 1968.

REFERENCES (Cont'd)

11. A Study of Cryogenic Propellant Stratification Reduction
     Techniques, Annual Report, General Dynamics, Fort Worth
     Division Report FZA-419, 15 September 1967.

12. A Study of Cryogenic Propellant Mixing Techniques, Volume 1,
     Mixer Design and Experimental Investigations, Final Report,
     FZA-439-1, 1 November 1968.

13. Study of Cryogenic Fluid Mixing Techniques, Volume 1, Large-
     Scale Experimental Mixing Investigations and Liquid-Oxygen
     Mixer Design, Final Report, General Dynamics, Fort Worth
     Division Report FZA-450-1, 15 September 1970.

14. Thermal Stratification of Cryogens Stored in a Low-Gravity
     Environment, Poth, L. J., and Van Hook, J. R., Proceedings
     of the Institute of Environmental Sciences, April 1971.

15. Control of the Thermodynamic State of Space-Stored Cryogenic
     Fluids by Jet Mixing, Poth, L. J., and Van Hook, J. R.,
     AIAA/SAE 7th Propulsion Joint Specialist Conference, Paper
     No. 71-646, June 1971.

16. Review of NERVA Radiation and Shielding Studies, Aerojet
     General Corporation Report RN-PA-0021, 30 September 1969.